Novel Bayesian Inferences from The Cosmic Microwave Background

विद्या वाचस्पति की
उपाधि की अपेक्षाओं की आंशिक पूर्ति में प्रस्तुत शोध प्रबंध

A thesis submitted in partial fulfillment of the requirements of the degree
of Doctor of Philosophy

द्वारा / By
सायन साहा / Sayan Saha

पंजीकरण सं. / Registration No.:
20172032

शोध प्रबंध पर्यवेक्षक / Thesis Supervisor:
प्रो. तरूण सौरदीप / Prof. Tarun Souradeep

सहपर्यवेक्षक/ Co-Supervisor:
प्रो. सौरभ दुबे / Prof. Sourabh Dube

भारतीय विज्ञान शिक्षा एवं अनुसंधान संस्थान पुणे

INDIAN INSTITUTE OF SCIENCE EDUCATION AND RESEARCH PUNE

2024

Dedicated to Maa and Baba

Declaration

Name of Student: Sayan Saha
Reg. No.: 20172032
Thesis Supervisor(s): Prof. Tarun Souradeep & Prof. Sourabh Dube (Co-Supervisor)
Department: Physics
Date of joining program: August 1, 2017
Date of Pre-Synopsis Seminar : December 26, 2023
Title of Thesis : Novel Bayesian Inferences from the Cosmic Microwave Background

I declare that this written submission represents my ideas in my own words and where others' ideas have been included, I have adequately cited and referenced the original sources. I also declare that I have adhered to all principles of academic honesty and integrity and have not misrepresented or fabricated or falsified any idea/data/fact/source in my submission. I understand that violation of the above will be cause for disciplinary action by the Institute and can also evoke penal action from the sources which have thus not been properly cited or from whom proper permission has not been taken when needed.

The work reported in this thesis is the original work done by me under the guidance of Prof. Tarun Souradeep.

Sayan Saha
Sayan Saha
Reg. no. 20172032

Date: May 27, 2024

CERTIFICATE

Certified that the work incorporated in the thesis entitled "Novel Bayesian Inferences from the Cosmic Microwave Background" Submitted by Sayan Saha was carried out by the candidate, under my supervision. The work presented here or any part of it has not been included in any other thesis submitted previously for the award of any degree or diploma from any other University or institution.

Tarun Souradeep

Date: May 27, 2024

Prof. Tarun Souradeep
Supervisor

Sourabh Dube

Date: May 31, 2024

Prof. Sourabh Dube
Co-Supervisor

ACKNOWLEDGEMENTS

The journey of a PhD student is an amazing experience. Its success depends on many factors and significant support. The first and foremost role is that of the supervisor. In my PhD, I was fortunate enough to work under Prof. Tarun Souradeep. His knowledge and experience always shone through in his guidance. He has an amazing intuition for any problem I encounter. Moreover, he maintained such an environment in the group where everyone could ask the most naive question and be encouraged to do so. His guidance and patience have shaped me into the researcher I am today.

Next, I owe a great deal to Dr. Shabbir Isak Shaikh. Shabbir is one of the most patient and remarkable people I know. He made a massive contribution by mentoring me and patiently answering all my questions, not just research-related but also those pertaining to any issues I faced. He truly is my friend, philosopher, and guide. Prof. Suvodip Mukherjee has also been an amazing influence. During the first part of my PhD, he helped me immensely to understand several complex concepts and guided me significantly in completing my initial work. I also appreciate the contributions and influence of Prof. Benjamin D. Wandelt during the first part of my work.

During the second part of the thesis, I had the opportunity to work with Prof. Julien Carron and Dr. Louis Legrand. Julien is one of the nicest and most humble people I know and has helped me tremendously in understanding the subject. Louis has been my go-to person every time I faced a problem in my project during my stay in Geneva. In addition to working with my collaborators, I have also learned from discussions with other group members in India and Switzerland. I would like to thank Dr. Rajorshi Chanda, Dr. Debrata Adak, Dr. Debajyoti Sarkar, Mr. Dipanshu Garg (Dipu), and Dr. Sarvesh Kumar Yadav. While staying in Geneva, I learnt a lot from Mr. Sebastian Belkner and Dr. Omar Darwish. Group meetings and journal clubs have been the most efficient places for me to learn new things. I am very grateful for that.

I am also grateful to some other people in my academic life. For example, my research advisory committee (RAC) members, Prof. Aseem Paranjape and Prof. Sourabh Dube. Sourabh is also technically my co-supervisor at IISER Pune and helped me a great deal with the any academic and administrative difficulties that I faced. Besides that, Sourabh is an amazing person, who has helped and guided me a lot during my PhD journey.

Besides the help we get in our academic life, we also need a network of friends to make this journey more enjoyable. Starting with the IISER-Pune campus, I was fortunate enough to have an amazing friend circle, such as Mr. Souvik Panda Mahapatra (Panda), Mr. Pratim Das, Ms. Madhurima Batabyal, Mr. Sumit Sen, Dr. Saikat Pahan, Mr. Sandipan Mahanta, Dr. Souptik Chakraborty (Souptik da). Souptik da is one of the people whom I respect a great deal and also a very good friend. He has also helped me a great deal in many aspects of this journey. During my stay in Geneva, I was fortunate enough to share an office with Mr. Nicolas De ro. In just a period of one year, he became one of my best friends. Along with being an amazingly aspiring physicist, he has been my most trusted trekking companion. The weekend treks with him have been so amazing and memorable. At the end of my PhD journey, I shifted to Raman Research Institute (RRI), Bengaluru. Here, I also became part of a great community. Not only does RRI provide the best possible environment for research, but the people here have made the concluding part of my PhD journey amazingly beautiful. I am really thankful to have friends such as Ms. Gunjan Tomar, Mr. Yash Agarwal, Prof. Saurabh Singh, Mr. Kinjal Roy, Mr. Aman Upadhyay, Mr. Shovan Barik, and Dr. Ion Santra. Even though I came here as a new person, they welcomed me with warmth and made me part of their family. The 'chai pe charcha' every evening is one of the fondest moments that I have had at RRI. One of many things I will miss is playing table tennis every evening.

I am really grateful for the support from my parents. They are my powerhouse. Even in difficult situations, they have encouraged me to follow my dreams and work hard. My father is the reason I was addicted to pursuing science in the first place. My mother is someone who taught me to follow my dreams. She has always encouraged me to ask questions. Only because of her, I acquired the habit of asking questions, which is the first step in becoming a scientist, in my opinion.

I want to acknowledge the HPCs: PARAM Brahma at IISER Pune and Yggdrasil at the University of Geneva. All the heavy computational work has been done here. I acknowledge the support from the technical people involved in both of these HPCs. Regarding the financial support, I want to acknowledge the IISER-Pune Institute PhD fellowship. Along with that, I also want to acknowledge other scholarships and grants such as the Swiss Government Excellence Scholarship (ESKAS No. 2022.0316) for my year-long research at the University of Geneva, grant (2000 CHF) from Société académique de Genève (SACAD) to attend the Future Science with CMB x LSS workshop at YITP, Kyoto University, and the Infosys Foundation Travel Award (50,000 INR) to attend the Future Cosmology workshop at IESC Cargese, France.

Table of Contents

Dedication **iii**

Declaration **v**

Certificate **vii**

Acknowledgement **ix**

Table of Contents **xiii**

List of Figures **xvi**

List of Tables **xxii**

Abstract **xxiv**

I Introduction **1**

1 Introduction **3**

1.1 CMB in the Era of Precision Cosmology 3

1.2 CMB Dipole 4

1.3 Small-Scale CMB fluctuations 7

1.3.1 Temperature Fluctuations 8

1.3.2 Polarization Fluctuations 9

1.4 Cosmological Principle and Statistical Isotropy (SI) 11

1.4.1 CMB Power-spectrum 11

1.4.2 Violation of SI and BipoSH Representation 13

1.5 Weak Lensing of CMB 14

1.6 Bayesian Inferences in Cosmology 18
1.7 Summary 19

II Doppler Boost of Cosmic Microwave Background 21

2 Overview of the Doppler Boost Model 23
2.1 Introduction 23
2.2 Imprint of Doppler boost on CMB 26
2.3 Covariance matrix of Doppler boosted CMB temperature map 28
2.4 Summary 33

3 Methodology 35
3.1 Introduction 35
3.2 Data Model and the Parameter Posterior 36
3.3 Sampling method: Hamiltonian Monte Carlo 37
3.4 Summary 40

4 Analysis on *Planck*-2018 CMB temperature map 41
4.1 Introduction 41
4.2 Implementation Details 42
4.3 HMC samples of CMB maps 46
4.4 Inference of the Covaraince Matrix 46
  4.4.1 The Diagonal Part 46
  4.4.2 The off-diagonal part 48
4.5 Robustness of Results on Different Foreground Cleaned Maps 53
4.6 Summary 53

5 Model Comparison with Bayes factor 57
5.1 Introduction 57
5.2 Bayes Factor for Known CMB Dipole Value 58
5.3 Bayes Factor for Known Quasar Dipole Value 59
5.4 Summary 60

III Clusters: Small-Scale CMB Lenses **61**

6 CMB lensing by galaxy clusters **63**
6.1 Introduction 63
6.2 NFW Profile 64
6.3 Lensing by NFW profile 65
6.4 Summary 68

7 Cluster mass estimators **71**
7.1 Intrduction 71
7.2 Lensing Reconstruction 73
  7.2.1 Data Model and the Covaiance Matrix 73
  7.2.2 Quadratic Estimator (QE) 74
  7.2.3 Maximum a Posteriori (MAP) Estimator 75
7.3 Cluster Signal Reconstruction 77
7.4 Summary 80

8 Results **83**
8.1 Introduction 83
8.2 Profile Reconstruction 84
8.3 Cluster mass constraints 88
8.4 Summary 91

9 Conclusion **93**
9.1 Doppler Boost of CMB 93
9.2 Clusters: Small-Scale CMB Lenses 95

Appendices **99**

A Appendix for Chapter 8 **101**
A.1 Exact QE bias calculation 101

Bibliography **103**

List of Figures

1.1 The spectrum of CMB as measured by FIRAS. Image source [1] 4

1.2 *Top:* The image of the CMB sky from COBE DMR 53 GHz band on a scale 0-4 K, showing a perfect uniformity. *Middle:* The fluctuation image in mK scale from DMR, after subtracting the CMB monopole. *Bottom:* The fluctuations in μK scale after subtracting the dipole as well. Image credit: NASA / COBE Science Team [1] 5

1.3 *Top panel*: The nine-year observed foreground cleaned WMAP (2001-2010), Image Source: [2]. *Bottom Panel:* Same temperature map as observed by *Planck*, foreground cleaned using `SMICA` [3] 7

1.4 Polarization anisotropy map measured by *Planck*, depicting headless vectors to represent the polarization field. This is overlaid on a temperature map for context. Both maps are at a resolution of 5 degrees for consistency and clearer interpretation. Image source: [3] 10

1.5 The summary of power spectrum measurements with different CMB-probes. *Upper pannel:* `CMB-TT`, `CMB-EE` and `CMB-BB` are the auto angular power-spectrum as defined in Eq. 1.10. The B-mode power spectrum is mostly due to the lensing of E-modes by the large-scale structure mass distribution of the late time universe. *Middle panel:* The cross power-spectrum between T and E modes. *Lower panel :* The power spectrum of the lensing potential, as defined in more detail in Section 1.5. Image source: [3] . . . 12

1.6 *Top panel*: The reconstructed lensing deflection map from *Planck*-2018 temperature and polarization data in 67% sky-fraction. Image source: [4]. *Middle Panel:* The reconstructed κ map from ACT DR6 data over 9400 deg^2 sky area. Image source [5]. *Bottom Panel:* The reconstructed κ map from SPT-3G 2018 temperature map in 1500 deg^2 sky area in the southern hemisphere. Image source [6] 17

1.7 Comparison of the measured lensing potential power spectrum $C_L^{\phi\phi}$ across various probes to date. Notably, the ACT DR6 results [7] exhibit the highest signal-to-noise ratio among these measurements, closely matched by the precision of the *Planck* `NPIPE` maps [8]. Image source: [7]. 18

2.1 We show the difference between a simulated statistically isotropic map and a Doppler boosted map at 217 GHz generated with the same value of the initial random seed using `CoNIGS` [9] with an injected signal in the fiducial dipole direction $\ell = 264°$, $b = 48°$, with the known amplitude $v/c \equiv \beta = 1.23 \times 10^{-3}$ for the illustration purpose. 25

2.2 The harmonic space `SMICA` weights used to construct the temperature maps $X_{\rm high}(\hat{n})$ (left panel) and $X_{\rm full}(\hat{n})$ (right panel), as mentioned in Eq. 2.13. Image source: [10] 30

2.3 In this figure we show the `SMICA` boost factor $b^{\texttt{SMICA}}(l)$ for 3 different masks, $f_{\rm sky} = 40.1\%$ (black curve), 59.1% (cyan curve) and 72.2% (magenta curve), which are depicted in Figure 4.1. $b^{\texttt{SMICA}}(l)$ corresponding to each mask is obtained by taking the peaks of histograms of $b_{lm}^{\texttt{SMICA}}$ (we have $(2l+1)$ modes at each l). As a reference, the red and the blue lines show the boost factor b_ν for the *CMB channels*, 143 GHz and 217 GHz, respectively. 31

4.1 The grey regions in Figure 4.1a, 4.1b and 4.1c are the three different masks ($f_{\rm sky} = 40.1\%$, 59.1% and 72.2% respectively), that have been used in our analysis. 43

4.2 *Top panel:* The noise variance map, obtained from 200 FFP10 noise simulations, used in our analysis. *Bottom panel:* One of the FFP10 noise realizations. 44

4.3 *Top panel:* One of the sample maps ($N_{\rm side} = 2048$) obtained from the a_{lm} samples with the primary set-up ($f_{\rm sky} = 40.1\%$, $l_{\rm max} = 1950$). *Bottom panel:* The difference between the SMICA map and the sample map at unmasked regions 45

4.4 *Top panel:* The distributions of C_l's for six different l values. Histograms are obtained using the samples of C_l. The solid black curve is the analytic distribution curve of that specific C_l. The black dashed line shows the peak values. The solid red line represents the value of C_l obtained from `SMICA` map. The magenta line shows the best fit ΛCDM theory C_l given by *Planck*. *Bottom panel:* The Maximum-a-posteriori estimate of C_l distribution inferred in this analysis (black curve) along with the realisation C_l (red curve) obtained from the `SMICA` map. The blue curve represents the best fit ΛCDM theory C_l given by *Planck*. We have an evidence in the power spectrum of a SMICA residual of an isotropic unresolved extra-galactic point source background. 47

4.5 The figure presents the 1D distributions and 2D joint distributions of β_{10}, β^r_{11} and β^i_{11} samples. These samples are obtained from the analysis of the `SMICA` 2018 temperature map, with $f_{sky} = 40.1\%$ mask, using multipoles up to $l_{max} = 1950$. The contours in the joint distribution show the levels for 68% and 90% of the sample points, respectively. The blue dashed line shows the peak values of the distribution and the red solid line represents the canonical value of our local motion from CMB dipole. 50

4.6 the distribution of β. The samples of β, θ_β and ϕ_β has been obtained from the β_{10}, β^r_{11} and β^i_{11} samples using Eq. 2.9. 51

4.7 The joint distribution of θ_β and ϕ_β with $f_{\rm sky} = 40.1\%$ mask, using multipoles up to $l_{\rm max} = 1950$. The samples of β, θ_β and ϕ_β has been obtained from the β_{10}, β^r_{11} and β^i_{11} samples using Eq. 2.9. In Figure 4.6, the dashed blue line is the mean of this histogram, whereas the dashed cyan line depicts the β value corresponding to the maximum posterior points of β_{10}, β^r_{11} and β^i_{11} parameters. The purple curve represents the analytical form of this distribution (as derived in [11]). The dashed red line presents the known dipole amplitude corresponding to the Solar System velocity 1.23×10^{-3}. In Figure 4.7, the θ_β and ϕ_β samples are binned in a `HEALPix` grid of $N_{\rm side} = 32$, normalized by its peak value and smoothed by a Gaussian kernel. The cyan circle represents the maximum posterior point of the distribution with our primary set-up. The white cross represents the known dipole direction. In this figure, we also depict the inferred direction for the other analysis setups: $f_{\rm sky} = 59.1\%$, $l_{\rm max} = 1950$ (cyan diamond); $f_{\rm sky} = 72.2\%$, $l_{\rm max} = 1950$ (cyan square); $f_{\rm sky} = 40.1\%$, $l_{\rm max} = 1500$ (magenta circle); $f_{\rm sky} = 59.1\%$, $l_{\rm max} = 1500$ (magenta diamond) and $f_{\rm sky} = 72.2\%$, $l_{\rm max} = 1500$ (magenta square). The grey and purple lines show the borders of $f_{\rm sky} = 40.1\%$ and $f_{\rm sky} = 72.2\%$ masks respectively. . 52

4.8 *Top panel:* The distributions of the velocity amplitude for `NILC` (black), `SEVEM` (blue) and `SMICA` (orange), with the mask $f_{\rm sky} = 40.1\%$ using multipoles from $l_{\rm min} = 800$ up to $l_{\rm max} = 1950$. The inferred values from these three maps have been indicated by the dashed line, with the same colour choices. The red dashed line represents the value inferred from CMB dipole. *Bottom panel:* The inferred directions for `NILC` (magenta dot), `SEVEM` (green dot) and `SMICA` (yellow dot), with the mask $f_{\rm sky} = 40.1\%$ using multipoles from $l_{\rm min} = 800$ up to $l_{\rm max} = 1950$. The map shown in this figure corresponds to the observed CMB dipole, with the direction indicated by the white cross. 55

6.1 The well-known dipole-like structure that we expect in (lensed-unlensed) [1] sky when there is a cluster with $M_{200} = 2 \times 10^{14} M_\odot{}^2$, $z = 0.7$ present in our line of sight. 67

7.1 Comparison of reconstruction noises for QE, HDV QE, and MAP estimators in the combined TQU channel under CMB-S4 noise and beam conditions. 78

7.2 Contribution per lensing multipole to the cluster mass SNR (the integrand of Eq. 7.12) shown in case of a $2\times10^{14}M_\odot$ cluster at $z=0.7$, for the CMB-S4-like configuration described in the text. Green, orange and magenta show temperature-only, polarization-only and combined reconstruction respectively. Dashed shows the quadratic estimator case and solid the CMB lensing maximum a posteriori method of this work. Dotted shows the QE with a high-ℓ cut on the gradient leg [12]. While the MAP approach is exactly the same than for optimal CMB lensing power spectrum reconstruction, this probes much smaller scales (the spectrum SNR is almost entirely confined to $L<1500$ for this configuration). 80

8.1 *Top panel*: Reconstructed deflection angle profiles $\alpha(\theta)$ from stacking a set of 1000 temperature-only reconstructions ($M=4\times10^{14}M_\odot, z=0.7$). CMB multipoles $100\leq\ell\leq5000$ are used to reconstruct the lensing multipoles $100\leq L\leq5000$. Shown are the standard QE (blue), QE with a high-ℓ cut at 2000 on the gradient leg [12] (green, HDV QE), and the maximum a posteriori (MAP) lensing reconstruction of this work (red, without any cuts), and the input truncated to the same L range. The bias in the MAP reconstruction is much reduced compared to the QE but still visible at this cluster mass. In polarization reconstruction no such bias is visible. The deflection profile's oscillatory features results from the fact that the lensing reconstruction is performed in harmonic space and truncated to $L_{\max}=5000$. *Lower panel:* The same profiles in harmonic space, weighted at each multipole by their contribution to the cluster mass estimate (see Eq. (7.11)). An estimate of the map-level reconstruction noise was subtracted in each realization, in order to accelerate convergence, so that the scatter is not representative of an actual data analysis. Analytic predictions are given for the QE and HDV QE cases as the dotted and dashed black lines. The MAP case is slightly tilted in this configuration compared to the input profile (solid black). 85

8.2 Analytical predictions for the QE-inferred mass bias as a function of halo mass for temperature-only QE lensing mass map reconstruction, with (green, 'HDV QE') and without (blue) cut on the gradient leg [12], including CMB multipoles $100 \leq \ell \leq 5000$ and lensing multipoles $100 \leq L \leq 5000$ (here all clusters are set at $z = 0.7$). The points show the corresponding results for our simulated reconstructions with $M_{200} = 4, 7$ and $10 \times 10^{14} M_{\odot}$, together with the result of our MAP method (red). The error bar is our empirical estimate for a sample of a thousand cluster. The bias is a strong function of halo mass and can be very significant for massive haloes. 86

8.3 Same as the lower panel of Fig. 8.1, for the polarization-only (QU) quadratic and MAP estimators. The QU channel does not suffer from the bias due to strong to moderate lensing close to the cluster center. 87

8.4 Constraints on cluster mass for a sample of 1000 identical clusters ($M_{200} = 2 \times 10^{14} M_{\odot}$, at redshift 0.7) as a function of white noise levels. The beam FWHM is 1 arcmin. It is important to note that the the relative noise quantity $\sigma_{M_{200}}/M_{200}$ corresponds the error the mass measurement for 1000 stacked clusters. Green, orange and magenta show temperature-only, polarization-only and combined reconstruction respectively. Dotted lines (HDV QE) show the QE forecast (Eq. 7.12) with a cut at 2000 in the gradient leg [12] to remove the QE bias (see Fig. 8.1), dashed lines the QE case without any cuts, and solid the maximum a posterior lensing map reconstruction method of this work (MAP). The improvement in constraining power comes from the partial removal from the CMB maps of the lensing signal not directly related to the cluster, and is more prominent in polarization, as expected. Markers with error bars are estimated from our set of simulations, with the x coordinate slightly shifted for clarity. The error bars are obtained from the bootstrapping method (for 1000 clusters), showing good consistency. In the QE case, we applied a simple multiplicative correction to remove the bias in the estimate. 90

List of Tables

4.1 Summary of results for different choices of mask, with $l_{\rm min} = 800$ and $l_{\rm max} = 1950$ 49

4.2 Summary of results for different component separation CMB maps, with mask $f_{\rm sky} = 40.1\%$, using multipoles from $l_{\rm min} = 800$ upto $l_{\rm max} = 1950$ . . 54

8.1 Summary of results on 1000 simulations with input $\kappa_0 = 0.1285$, corresponding to a cluster mass of $M_{200} = 2 \times 10^{14} M_{\odot}$ at $z = 0.7$. The table displays the mean $\hat{\kappa}_0$ evaluated from 1000 simulations along with the corresponding errors σ_{κ_0}, obtained using from bootstrapping. For the T and TQU estimators, HDV QE results are provided, while the QE result is presented for the QU estimator. Additionally, MAP estimated values are shown in the second row. $\sigma^{\rm th}_{\kappa_0}$ depicts the theoretical error prediction given by Eq. 7.12. See also Fig. 8.4. 89

ABSTRACT

In the evolving landscape of modern precision cosmology, the continuous progress of ongoing and upcoming surveys has provided us with an unprecedented level of statistical power for drawing robust inference. The study of the Cosmic Microwave Background (CMB) fluctuations has been pivotal in this progress. The CMB acts as a tracer of the primordial fluctuation field at the time of the last scattering, around a redshift of $z = 1100$, corresponding to 380,000 years after the Big Bang. As these photons have journeyed through the universe, they have experienced weak gravitational lensing by the mass distribution in the large-scale structure of the later universe, thus carrying imprinted information about this later period. Additionally, the frame from which we observe the CMB, specifically the Solar-System barycentre, is in motion relative to the cosmological rest frame, which further influences the observed CMB fluctuations. This thesis explores these two secondary effects on the CMB fluctuations to infer significant phenomena, employing a Bayesian framework to analyze and interpret the data.

The first part of the thesis introduces the fundamental concepts of CMB. In the subsequent part, we study the impact of the observation frame's motion on CMB fluctuations. On the largest scales, this motion can boost the CMB monopole to generate a dipole. However, distinguishing this kinematic dipole from an intrinsic dipole in the observed CMB dipole is challenging. According to the simplest and currently most favoured inflationary model, the intrinsic dipolar fluctuation in the CMB, should be of the same order as fluctuations (10^{-5} to 10^{-6} K) at smaller angular scales. To test this, we study the relativistic effects of this motion, namely modulation and aberration, on small-scale CMB fluctuations. These effects break the statistical isotropy of the CMB, leading to off-diagonal terms in the harmonic space covariance matrix. We employ a Bayesian approach, using Hamiltonian Monte-Carlo (HMC) sampling, to explore the joint posterior distribution of the covariance matrix and the signal. Our findings align the inferred velocity with the canonical value obtained from the CMB dipole, achieving a significance of approximately $\sim 5\sigma$, the most competitive significance to date.

The third part of the thesis focuses on using the gravitational lensing signal of the CMB to probe galaxy clusters. As the largest collapsed objects in the universe, clusters offer critical insights into cosmological parameters. The abundance of clusters as a function of mass and redshift directly probes the structure growth amplitude, mass

fraction, neutrino mass, and dark energy equation of state parameters. Hence, accurate cluster mass measurements at high redshifts are crucial for this analysis. Anticipating the CMB Stage 4 (CMB S4) experiment, we demonstrate the effectiveness of maximum-a-posteriori estimation of the gravitational lensing potential for cluster mass estimation. This approach significantly enhances the precision of cluster mass measurements in S4-like experiments by approximately 13-20% over the conventional quadratic estimator (QE). We also address the known bias in the temperature quadratic estimator caused by the strong non-Gaussianity of the signal. Our results show that our estimator effectively mitigates this bias without requiring scale cuts, thus preserving the signal-to-noise ratio. The thesis is based on the following publications,

1. **Sayan Saha**, Shabbir Shaikh, Suvodip Mukherjee, Tarun Souradeep, and Benjamin D. Wandelt, **Bayesian estimation of our local motion from the Planck-2018 CMB temperature map**, JCAP 10 (2021) 072, arXiv:2106.07666 [astro-ph.CO],

2. **Sayan Saha**, Louis Legrand, and Julien Carron, **Cluster profiles from beyond-the-QE CMB lensing mass maps**, JCAP 01 (2024) 024, arXiv:2307.11711 [astro-ph.CO].

Part I

Introduction

Chapter 1

Introduction

1.1 CMB in the Era of Precision Cosmology

Cosmology is the scientific study of the universe's overall structure and evolution over time. The Hot Big Bang model is the most widely accepted model for the universe's beginning. This model theorizes that the universe originated from an intensely hot plasma state and has been continuously expanding. Approximately 300,000 years after the beginning, the universe had cooled sufficiently to allow the formation of the first neutral atoms. During this epoch, photons, one of the fundamental components, became decoupled from the plasma and have been traveling towards us. These photons are known as the Cosmic Microwave Background (CMB) radiation. Due to the expansion of the universe, these photons have experienced significant redshift, now observable as an omnipresent blackbody background at a temperature of 2.7 K.

At later times, the neutral baryonic matter collapsed in the gravitational wells of the dark matter clumps and reionized the universe, giving rise to its first stars and galaxies. Since then, the universe has continued to evolve under the influence of gravity, resulting in the large-scale structure we observe today. The distribution of galaxies, alongside the CMB photons, serve as crucial probes, offering insights into the universe at different times. As cosmologists, our primary goal is to comprehend the universe's evolution across these different epochs. The most widely acclaimed model that aligns with empirical evidence is the ΛCDM model. This model delineates the universe as a composition predominantly of a cosmological constant, Λ, associated with dark energy, cold dark matter (CDM), and ordinary baryonic matter. Their respective proportions have been meticulously quantified

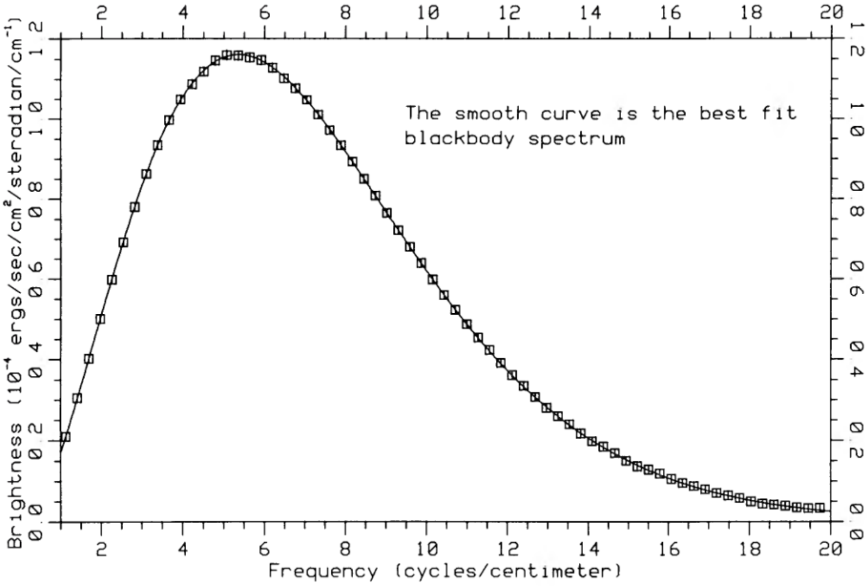

Figure 1.1: The spectrum of CMB as measured by FIRAS. Image source [1]

through various cosmological surveys.

The journey of observational cosmology began with a groundbreaking discovery by Edward Hubble in 1924. Hubble's observation of galaxies beyond the Milky Way revealed a profound truth: the universe is in a state of expansion. This revelation, pointing to the existence of a hot early universe, set the stage for another pivotal moment in the field: the serendipitous discovery of the CMB radiation [13] by Arno Allan Penzias and Robert Woodrow Wilson in 1965. This discovery, interpreted by Robert Dicke and his group [14] at Princeton, provided the first concrete evidence supporting the inference of a hot early universe. Following this discovery, the Cosmic Background Explorer (COBE) mission [15] undertook the first space-based measurement of this radiation across a spectrum of frequencies. Remarkably, COBE found that the CMB exhibits the most perfect blackbody spectrum ever observed in science, with a temperature of $T_0 = (2.7255 \pm 0.0006)K$ [16,17]. The Far InfraRed Absolute Spectrophotometer (FIRAS) aboard COBE was specifically designed to measure deviations from the CMB's blackbody spectrum. Its exquisite observations matched a blackbody spectrum perfectly, as shown in Figure 1.1.

1.2 CMB Dipole

In cosmological studies, when observing the CMB, our frame of reference is not the Cosmological Rest Frame but rather one in motion. This is because we observe from the

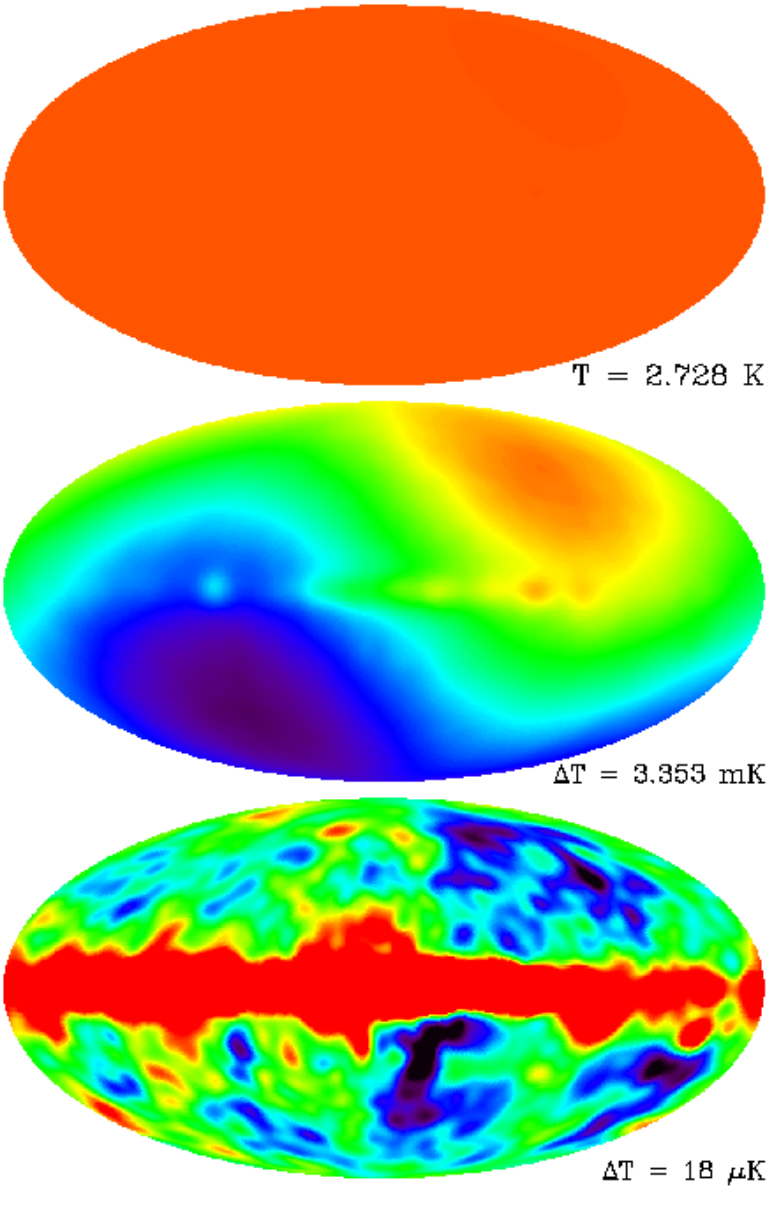

Figure 1.2: *Top:* The image of the CMB sky from COBE DMR 53 GHz band on a scale 0-4 K, showing a perfect uniformity. *Middle:* The fluctuation image in mK scale from DMR, after subtracting the CMB monopole. *Bottom:* The fluctuations in μK scale after subtracting the dipole as well. Image credit: NASA / COBE Science Team [1]

Earth, which itself is constantly moving. However, in CMB experiments, this motion – particularly the Earth's orbit around the sun – is meticulously accounted for and subtracted from the observations. We effectively consider our observation frame as the Solar System Barycenter, which, while more stable, is still in motion relative to the Cosmological Rest Frame.

The CMB appears isotropic (uniform) in the Cosmological Rest Frame. The mean temperature of the CMB is denoted as T_0. When our observation frame is moving at a velocity $\boldsymbol{v}$, this movement creates an observable dipole pattern across the sky. This pattern can be mathematically represented as:

$$\Delta T^{\mathrm{d}}(\hat{n}) = T_0(\boldsymbol{\beta} \cdot \hat{n}). \tag{1.1}$$

Here, $\boldsymbol{\beta} = \boldsymbol{v}/c$, where c is the speed of light, and $\hat{n}$ denotes the unit vector pointing towards the sky coordinates (θ, ϕ).

The Differential Microwave Radiometer (DMR) [18] aboard the COBE satellite marked a significant milestone in cosmology as the first instrument to measure the CMB fluctuations beyond the dipole anisotropy in the 1970's. Equipped with three frequency channels at 31.4, 53, and 90 GHz, the DMR was specifically designed to capture these subtle variations. The instrument successfully measured the Dipole field [19], as described in Eq. 1.1. This measurement is illustrated in the middle panel of Figure 1.2. However, when observing the dipole in the CMB, it is challenging to discern whether it results from the motion of our observational frame or is an intrinsic feature of the CMB itself. Unraveling this degeneracy is a crucial focus of the second part of this thesis, where we explore the impact of our motion on small-scale fluctuations in the CMB.

To better understand these small-scale fluctuations, it is necessary to subtract the dipole contribution from the fluctuation map. The COBE DMR was also pivotal in providing the first map of these fluctuations beyond the dipole in the μK scale. The lower panel of Figure 1.2 displays these fluctuations as detected by the DMR's 53 GHz channel. In the next section, we delve deeper into these fluctuations on a small angular scale, discussing their characteristics and implications in more detail.

---

[1] https://lambda.gsfc.nasa.gov/product/cobe/dmr_image.html

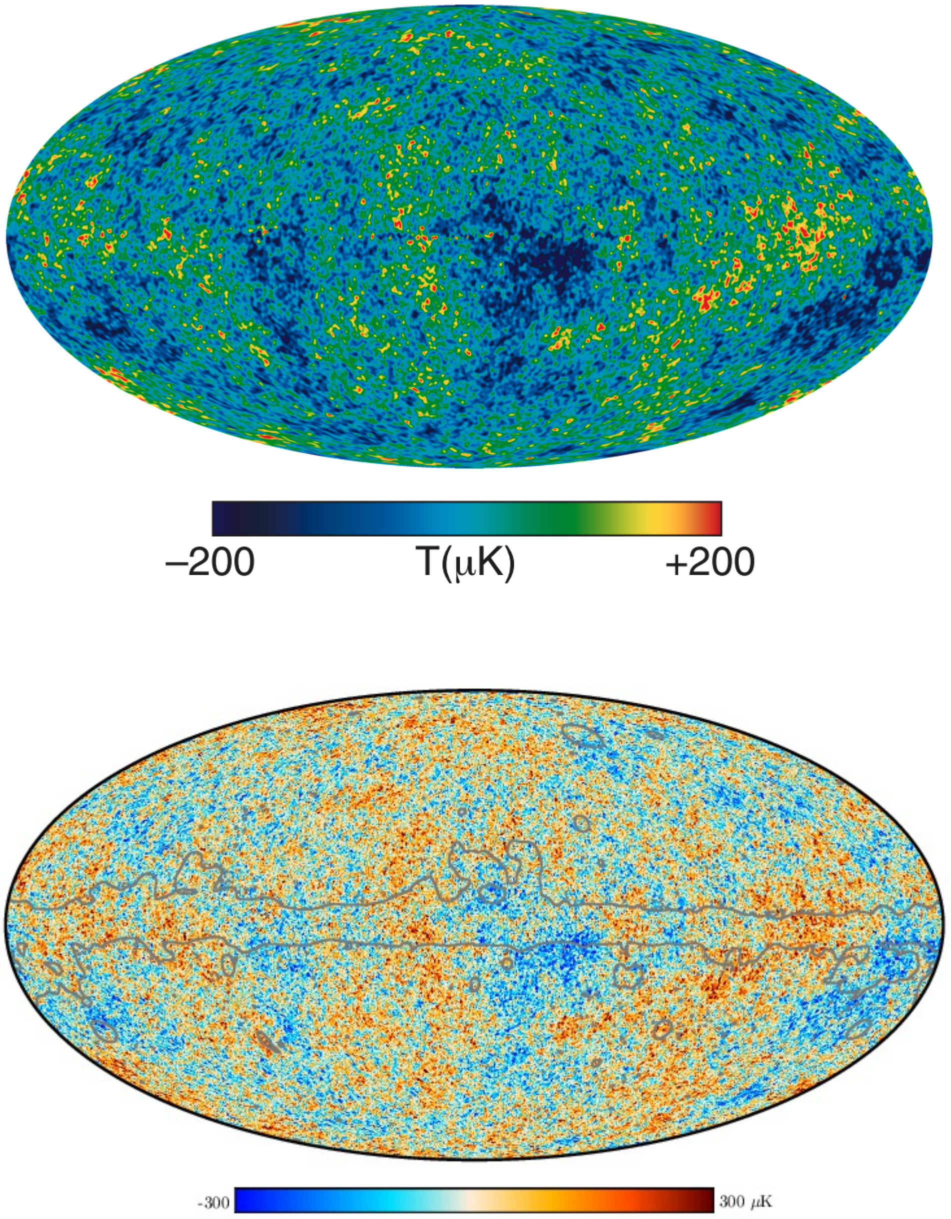

Figure 1.3: *Top panel*: The nine-year observed foreground cleaned WMAP (2001-2010), Image Source: [2]. *Bottom Panel:* Same temperature map as observed by *Planck*, foreground cleaned using `SMICA` [3]

1.3 Small-Scale CMB fluctuations

CMB fluctuations at small angular scales beyond the dipole are pivotal in exploring the primordial universe. Notably, these fluctuations are detectable at a scale of about 10^{-5}K, much smaller than milliKelvin. They offer insights into the universe's conditions during the last scattering. These fluctuations, which originated as primordial quantum fluctuations during inflation, have evolved to leave discernible imprints on the CMB. These fluctuations are also the seeds of the web-like structures observed in the universe's Large Scale Structure (LSS) at later stages. Additionally, the CMB photons exhibit fluctuations in polarization, approximately 10% the amplitude of temperature fluctuations, providing another layer of understanding about the early universe.

1.3.1 Temperature Fluctuations

The observation of CMB temperature fluctuations has significantly advanced since the initial detection by the COBE DMR. In the first decade of the 21st century, NASA's Wilkinson Microwave Anisotropy Probe (WMAP) [2] took over, offering improved resolution measurements. Following WMAP, the European Space Agency's *Planck* [3] satellite, in the second decade, provided the most detailed full-sky image of the CMB temperature fluctuations to date. The measured fluctuations by these two missions are illustrated in Figure 1.3. Besides these major space missions, numerous other ground-based and balloon-borne experiments have contributed to our understanding by providing high-resolution data, albeit for limited sky fractions.

The observed CMB fluctuations, which are CMB monopole and dipole subtracted fluctuations, are basically a function on a sphere. They have a functional form that depends on the direction unit vector $\hat{n} \equiv \{\theta, \phi\}$, where θ and ϕ are the polar and azimuthal angle, respectively. It is always convenient to study these fluctuations in spherical harmonic basis,

$$\delta T(\hat{n}) = \sum_{l} \sum_{m=-l}^{l} a_{lm} Y_{lm}(\hat{n}). \tag{1.2}$$

Here, $Y_{lm}(\hat{n})$ denotes the spherical harmonic functions, while a_{lm} represents the spherical harmonic coefficients, defined as $a_{lm} = \int d\Omega_{\hat{n}} \delta T(\hat{n}) Y^*_{lm}(\hat{n})$. The index l and m are the CMB multipoles. For Gaussian random fields, two-point correlation functions are sufficient to characterize the field's statistics. In the case of a statistically isotropic sky, the spherical harmonic coefficients at distinct multipoles are expected to be uncorrelated, as expressed by:

$$\langle a_{lm} a^*_{l'm'} \rangle = \delta_{ll'} \delta_{mm'} C_l. \tag{1.3}$$

Here, C_l represents the power spectrum of the field and essentially indicates the variance of the Gaussian random variables a_{lm}. The ensemble average in the above equation can also be obtained as an average over multiple independent realizations of the Gaussian sky. As we can only observe the CMB from a single point in the universe, we have access to only one realization of the signal. Nevertheless, the statistical isotropy of the sky allows the construction of an estimator for C_l from averaging over all the CMB multipoles at any l, as follows:

$$\hat{C}_l = \frac{1}{2l+1} \sum_{m=-l}^{l} |a_{lm}|^2. \tag{1.4}$$

In this equation, a_{lm} represents the spherical harmonic coefficients of the observed data. The essence of this estimator is that, instead of averaging over different realizations, the statistical isotropy allows for averaging over different multipoles m corresponding to the same l, providing an unbiased estimator of C_l. For a full-sky analysis, the number of multipoles available for a single l is $(2l + 1)$. If the analysis is conducted on a fraction of the sky, the term $(2l + 1)$ in Eq. 1.4 is substituted with the available number of modes $f_{\text{sky}}(2l + 1)$, where f_{sky} represents the fraction of the sky under analysis.

1.3.2 Polarization Fluctuations

Towards the end of the epoch of recombination, photons underwent the last Thomson scattering off free electrons, leading to a remnant polarization pattern in the CMB photons. This scattering, in the presence of a quadrupole temperature anisotropy, produces a remnant linear polarization. The CMB polarization is typically analyzed using Stokes parameters Q, U, and V. However, in the standard physics, the circular polarization (V) in CMB photons is negligible, so it is often excluded from consideration. Linear polarization can be conceptualized as a headless vector field on the celestial sphere. Consequently, the zero-spin spherical harmonic basis is insufficient for its decomposition. Notably, the quantity $(Q \pm iU)$ transforms as a spin-2 field under rotations of the coordinate system around the unit vector $\hat{n}$. This allows for the use of a spin-2 spherical harmonic basis for its representation. Mathematically, this is expressed as [20, 21],

$$(Q \pm iU)(\hat{n}) = \sum_{l} \sum_{m=-l}^{l} a_{\pm 2,lm} \, {}_{\pm 2}Y_{lm}(\hat{n}). \tag{1.5}$$

Here, ${}_{\pm 2}Y_{lm}(\hat{n})$ represents the spin ± 2 spherical harmonics, and $a_{\pm 2,lm}$ are the corresponding coefficients in this expansion. The quantities Q and U are dependent on the choice of the coordinate system around the unit vector $\hat{n}$. In order to make them in-

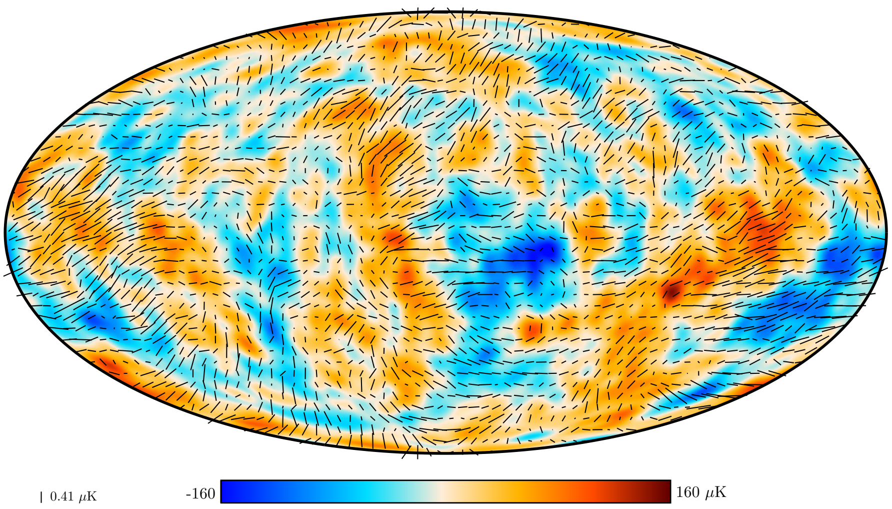

Figure 1.4: Polarization anisotropy map measured by *Planck*, depicting headless vectors to represent the polarization field. This is overlaid on a temperature map for context. Both maps are at a resolution of 5 degrees for consistency and clearer interpretation. Image source: [3]

dependent of the choice of the coordinate system, we write the coefficients in terms of parity eigenstates, such as

$$a_{\pm 2,lm} = E_{lm} \pm iB_{lm}. \tag{1.6}$$

Here, E_{lm}'s and B_{lm}'s are the parity even and parity odd modes. Under parity transformation, they behave in the following manner,

$$\begin{aligned} E_{lm} &\rightarrow (-1)^l E_{lm}, \\ B_{lm} &\rightarrow (-1)^{l+1} B_{lm}. \end{aligned} \tag{1.7}$$

These E and B modes now can be expressed in real space in the same footing of scaler fields, similar to the temperature field T, such as

$$\begin{aligned} E(\hat{n}) &= \sum_l \sum_{m=-l}^{l} E_{lm} Y_{lm}(\hat{n}), \\ B(\hat{n}) &= \sum_l \sum_{m=-l}^{l} B_{lm} Y_{lm}(\hat{n}). \end{aligned} \tag{1.8}$$

The polarization anisotropy map contains a wealth of information and offers an independent probe of the fluctuations in the primordial universe. Despite the challenge posed by their polarization anisotropy being merely 10% of the temperature's amplitude, significant progress has been made. *Planck* first mapped full-sky polarization, as shown in Figure 1.4. Higher sensitivity observations have since been achieved by ground-based telescopes like the Atacama Cosmology Telescope (ACT) [22], South Pole Telescope (SPT) [23], BICEP [24], and POLARBEAR [25]. The next few decades promise even more detailed maps from projects like Simon's Observatory (SO) [26], Ali CMB Polarization Telescope (AliCPT) [27], and CMB Stage-4 [28], along with the space-based mission LiteBIRD [29], which promises to provide full-sky polarization maps with 1000 times the sensitivity of *Planck*. These advancements underscore the importance of studying CMB polarization to detect the imprints of primordial gravitational waves, providing direct evidence of the universe's inflationary stage.

1.4 Cosmological Principle and Statistical Isotropy (SI)

At the largest scales, the universe adheres to the cosmological principle, which states that the universe is homogeneous and isotropic. This principle suggests that the universe lacks any privileged locations and no preferred direction in space exists. Consequently, this principle extends to the concept of statistical homogeneity and statistical isotropy (SI) in fluctuation fields across the universe.

1.4.1 CMB Power-spectrum

The SI of the CMB fluctuations is described by the two-point correlation function $\langle X(\hat{n})X'(\hat{n}')\rangle$, where this function depends only on the angular separation between two points. The function is expressed as:

$$\langle X(\hat{n})X'(\hat{n}')\rangle = C(\theta) = \frac{1}{4\pi}\sum_{l=2}^{\infty}(2l+1)C_l^{XX'}P_l(\cos\theta). \tag{1.9}$$

Here, X and X' denote scalar fields associated with temperature and polarization, specifically $X \in T, E, B$. The angular separation θ between points $\hat{n}$ and $\hat{n}'$ is defined as $\theta = \arccos(\hat{n}\cdot\hat{n}')$. The second equality comes from decomposing the function of the angular separation into a series of Legendre polynomials. The coefficients $C_l^{XX'}$ represent the auto and cross power spectra of these fields. The criteria of SI in Eq. 1.4.1 directly boils down to the diagonality of the covariance matrix in the harmonic space. The non-zero diagonal terms are limited to the pairs TT, EE, BB, and TE, when the physics adhere to the principle of parity invariance. These relationships are described as follows:

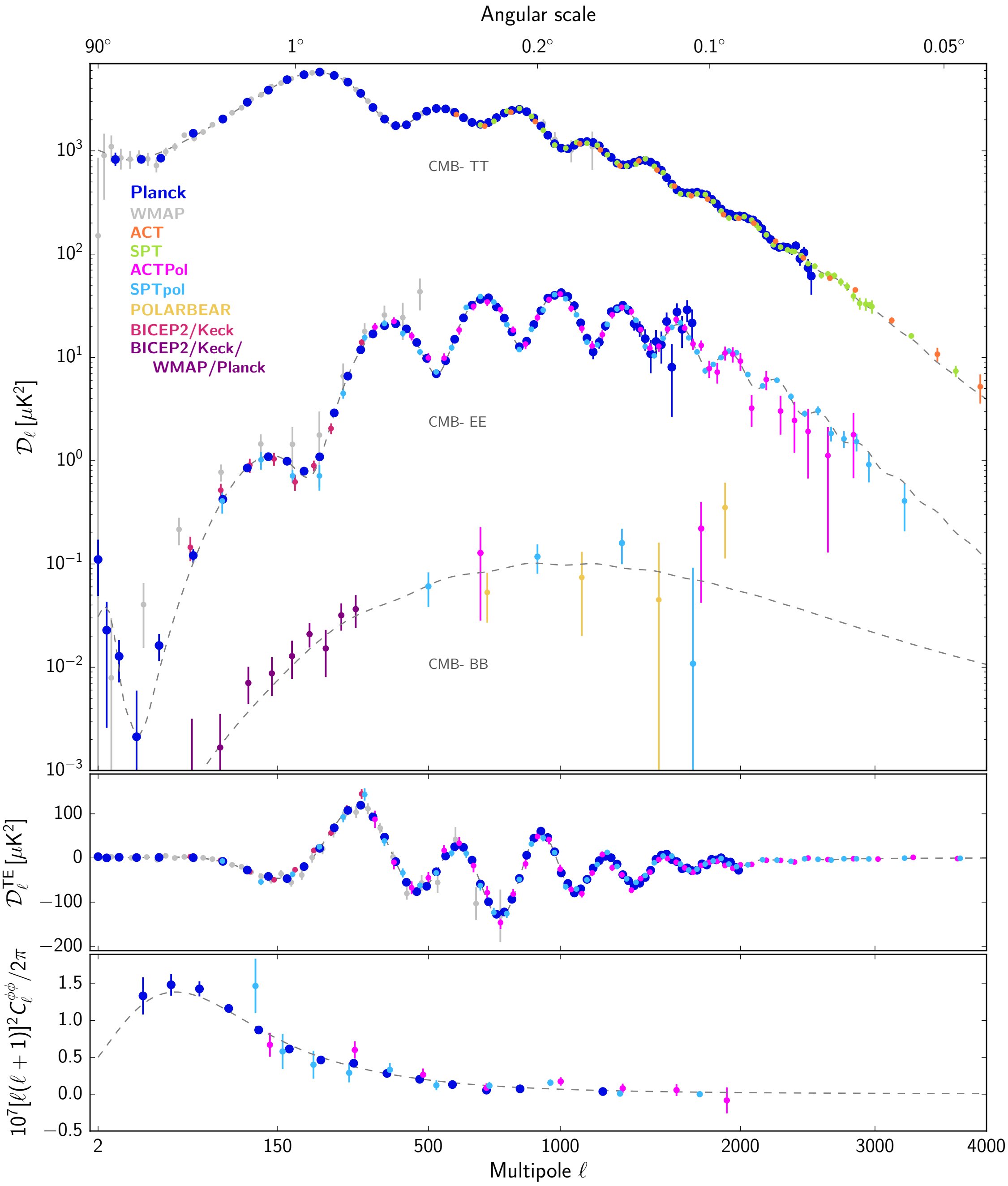

Figure 1.5: The summary of power spectrum measurements with different CMB-probes. *Upper pannel:* `CMB-TT`, `CMB-EE` and `CMB-BB` are the auto angular power-spectrum as defined in Eq. 1.10. The B-mode power spectrum is mostly due to the lensing of E-modes by the large-scale structure mass distribution of the late time universe. *Middle panel:* The cross power-spectrum between T and E modes. *Lower panel :* The power spectrum of the lensing potential, as defined in more detail in Section 1.5. Image source: [3]

$$
\begin{aligned}
\langle a_{lm} a^*_{l'm'} \rangle &= C_l^{TT} \delta_{ll'} \delta_{mm'}, \\
\langle E_{lm} E^*_{l'm'} \rangle &= C_l^{EE} \delta_{ll'} \delta_{mm'}, \\
\langle B_{lm} B^*_{l'm'} \rangle &= C_l^{BB} \delta_{ll'} \delta_{mm'}, \\
\langle T_{lm} E^*_{l'm'} \rangle &= C_l^{TE} \delta_{ll'} \delta_{mm'},
\end{aligned}
\tag{1.10}
$$

In recent decades, advancements in space and ground-based CMB probes have allowed us to measure these power spectra with increasing precision. These measurements, summarized in Figure 1.5, display the quantity $D_l = \frac{l(l+1)}{2\pi} C_l$.

1.4.2 Violation of SI and BipoSH Representation

As discussed previously, the assumption of SI in CMB fluctuations necessitates a diagonal covariance matrix in harmonic space. However, several factors subtly violate this SI nature. These include weak-lensing by large-scale structure mass distribution [30], Lorentz boost due to our observation frame's motion relative to the cosmological rest frame [31], scale-dependent Cosmic Hemispherical Asymmetry (CHA) [32], and observational limitations like non-circular instrument beam patterns and masking [33,34]. These factors introduce off-diagonal terms in the covariance matrix, capturing which is crucial for inferring signals that violate SI.

A convenient method to represent these off-diagonal terms is to use the mathematical framework of Bipolar Spherical Harmonics (BipoSH). This approach, first introduced in the context by Hajian and Souradeep 2003 [33], expands the two-point correlation functions in the BipoSH basis. Fundamentally, any function on the sphere S^2, such as the temperature fluctuation field $\delta T(\hat{n})$, can be expanded in the spherical harmonic basis $Y_{lm}(\hat{n})$, as shown in Eq. 1.2. Likewise, the two-point correlation function of the temperature fluctuation field, $C(\hat{n}_1, \hat{n}_2)$, being a function on $S^2 \times S^2$ space, can be expanded in the basis of this space:

$$
C(\hat{n}_1, \hat{n}_2) = \sum_{l_1, l_2} \sum_{L, M} A^{LM}_{l_1 l_2} \{ Y_{l_1}(\hat{n}_1) \otimes Y_{l_2}(\hat{n}_2) \}_{LM}. \tag{1.11}
$$

Here, $A^{LM}_{l_1 l_2}$'s are coefficients on this basis. The basis functions can be expressed in terms of the basis of S^2, i.e., the spherical harmonics, $Y_{lm}(\hat{n})$, as follows,

$$
\{ Y_{l_1}(\hat{n}_1) \otimes Y_{l_2}(\hat{n}_2) \}_{LM} = \sum_{m_1, m_2} C^{LM}_{l_1 m_1 l_2 m_2} Y_{l_1 m_1}(\hat{n}_1) Y_{l_2 m_2}(\hat{n}_2), \tag{1.12}
$$

where the $C^{LM}_{l_1 m_1 l_2 m_2}$ are the Clebsch-Gordan coefficients [35]. Similar to S^2 space, we can also do an inverse transform of the two-point correlation function $C(\hat{n}_1, \hat{n}_2)$ using the orthogonality condition of the BipoSH basis to obtain the BipoSH coefficients as

$$A^{LM}_{l_1 l_2} = \int d\Omega_{\hat{n}_1} \int d\Omega_{\hat{n}_2} C(\hat{n}_1, \hat{n}_2) \{Y_{l_1}(\hat{n}_1) \otimes Y_{l_2}(\hat{n}_2)\}^*_{LM}. \tag{1.13}$$

If we use the explicit forms of the correlation function and BipoSH basis, we can show that the BipoSH coefficients are actually a linear combination of the elements of the covariance matrix in harmonic space,

$$A^{LM}_{l_1 l_2} = \sum_{m_1, m_2} \left\langle a_{l_1 m_1} a^*_{l_2 m_2} \right\rangle (-1)^{m_2} C^{LM}_{l_1 m_1 l_2 - m_2}. \tag{1.14}$$

The Clebsch-Gordan coefficients constrain the number of non-zero elements in covariance for a given L value by $|l_1 - l_2| < L < l_1 + l_2$. The diagonal terms of the covariance matrix or the power spectrum are $L = 0$ terms of the BipoSH coefficients,

$$A^{00}_{l_1 l_2} = (-1)^{l_1} \sqrt{2 l_1 + 1} C_{l_1} \delta_{l_1 l_2}. \tag{1.15}$$

In the BipoSH expansion (Eq. 1.14), the terms $L \neq 0$, encapsulate the off-diagonal elements in the covariance matrix. These elements indicate deviations from statistical isotropy of the CMB fluctuations. In the second part of this thesis, we analyze the impact of our observational frame's motion on the CMB fluctuations. This motion introduces a relativistic boost to the fluctuations, leading to an observable violation of SI. The BipoSH formalism has been extensively used to study these violations of SI.

1.5 Weak Lensing of CMB

The CMB fluctuations carry a wealth of information about the early universe at a redshift of $z = 1100$. However, during their journey to us through the large-scale structure of the late-time universe, the CMB photons experience gravitational interaction with the large-scale structure. This gravitational effect, while weak, is significant enough to cause small detectable deflections. To simplify the analysis, an effective thin lens approximation is employed, akin to the Born approximation. In this approximation, we consider the cumulative deflection, which is an integration of deflections along the line of sight up to the last scattering surface, as effectively a single deflection by a 'thin lens'. The lensed temperature and polarization Stokes parameters, $\tilde{T}, \tilde{Q}, \tilde{U}$ are remapped due to lensing by a deflection vector $\boldsymbol{d}$ from the unlensed fields T, Q, U,

$$\begin{aligned} \tilde{T}(\hat{n}) &= T(\hat{n} + \boldsymbol{d}), \\ (\tilde{Q} + i\tilde{U})(\hat{n}) &= (Q + iU)(\hat{n} + \boldsymbol{d}). \end{aligned} \tag{1.16}$$

Here, the deflection field $\boldsymbol{d}(\hat{n})$ is a vector field on the sphere, representing the directional gradient of the scalar field, the projected lensing potential $\phi(\hat{n})$,

$$\boldsymbol{d}(\hat{n}) = \nabla_{\hat{n}} \phi(\hat{n}). \tag{1.17}$$

The scalar field $\phi(\hat{n})$ is a line-of-sight integration of the gravitational potential Ψ of the universe's large-scale structure, extending up to the last scattering surface:

$$\phi(\hat{n}) = -2 \int_0^{\chi_*} d\chi \frac{\chi_* - \chi}{\chi \chi_*} \Psi(\chi \hat{n}), \tag{1.18}$$

where χ represents the comoving distance, and χ_* is the comoving distance to the last scattering surface. In the third part of this thesis, we focus on the line-of-sight integrated surface density, closely related to the lensing convergence $\kappa(\hat{n})$, defined as:

$$\kappa(\hat{n}) = -\frac{1}{2} \nabla_{\hat{n}}^2 \phi(\hat{n}). \tag{1.19}$$

This convergence is a result of the quantum fluctuations from the time of inflation and can be treated as Gaussian in nature. Similar to the CMB fluctuation scalar fields, the lensing potential, $\phi(\hat{n})$ can be expressed in spherical harmonic basis:

$$\phi(\hat{n}) = \sum_L \sum_{M=-L}^{L} \phi_{LM} Y_{LM}(\hat{n}), \tag{1.20}$$

where ϕ_{LM} are the spherical harmonic coefficients for the lensing potential field $\phi(\hat{n})$. Throughout this thesis, we use lowercase l, m for CMB multipoles and uppercase L, M for lensing and BipoSH multipoles. For a statistically isotropic lensing potential field, we can define the power spectrum as

$$\langle \phi_{LM}\phi_{L'M'} \rangle = \delta_{LL'}\delta_{MM'}C_L^{\phi\phi}. \tag{1.21}$$

In the third part of the thesis, we study clusters with CMB lensing. These clusters, being a few arc minutes in size, allow for the flat-sky approximation and consequently the use of Fourier transforms, significantly reducing computational complexity. Under the flat-sky approximation, lensing and CMB multipoles are represented as vectors in Fourier space. In real space, lensing causes the remapping of the unlensed map as outlined in Eq. 1.5. For the$E$ and B modes, lensing induces a transfer of power from E modes to B modes. In Fourier space, lensing also causes violation of the SI of CMB fluctuations, resulting in off-diagonal terms [36, 37]

$$\left\langle \tilde{X}(\boldsymbol{l})\tilde{X}'(\boldsymbol{l'}) \right\rangle_{\text{fixed } \phi} = f_\alpha(\boldsymbol{l}, \boldsymbol{l'})\phi(\boldsymbol{L})\delta(\boldsymbol{l} + \boldsymbol{l'} - \boldsymbol{L}). \tag{1.22}$$

Here, the averaging is over different realizations of the unlensed CMB, with a fixed realization of the lensing potential, $\phi(\hat{n})$. The function f_α is a correlation function dependent on the pair $\alpha \in \{TT, EE, BB, TE, TB, EB\}$, as outlined in Table 1 of [36]. Utilizing this correlation, one can construct a minimum variance quadratic estimator for the lensing potential, known as the Hu-Okamoto quadratic estimator [36] and Okamoto-Hu estimator [37] for the full-sky version. Such an estimator was used to reconstruct the lensing map from *Planck*-2018 temperature and polarization maps [4], as presented in the top panel of Figure 1.6. Similar reconstructions have been conducted using ACT DR6 data [5] and SPT-3G data [6], as depicted in middle and bottom panels in Figure 1.6, respectively. The comparison of measured lensing potential power-spectrum across several probes to date has been presented in Figure 1.7.

The third part of the thesis is dedicated to the study of clusters, which act as small arcmin scale lenses. This analysis is conducted in anticipation of upcoming CMB experiments characterized by exceptionally low noise levels and high-resolution data, such as CMB Stage-4 (CMB S4) [28]. In our approach to reconstructing the lensing signature of individual clusters, the reconstructed lensing potential of the large-scale structure is treated as an additional level of Gaussian noise. Furthermore, we utilize lensing multipoles up to $L = 6000$, a range expected to be accessible by CMB S4. A key motivation

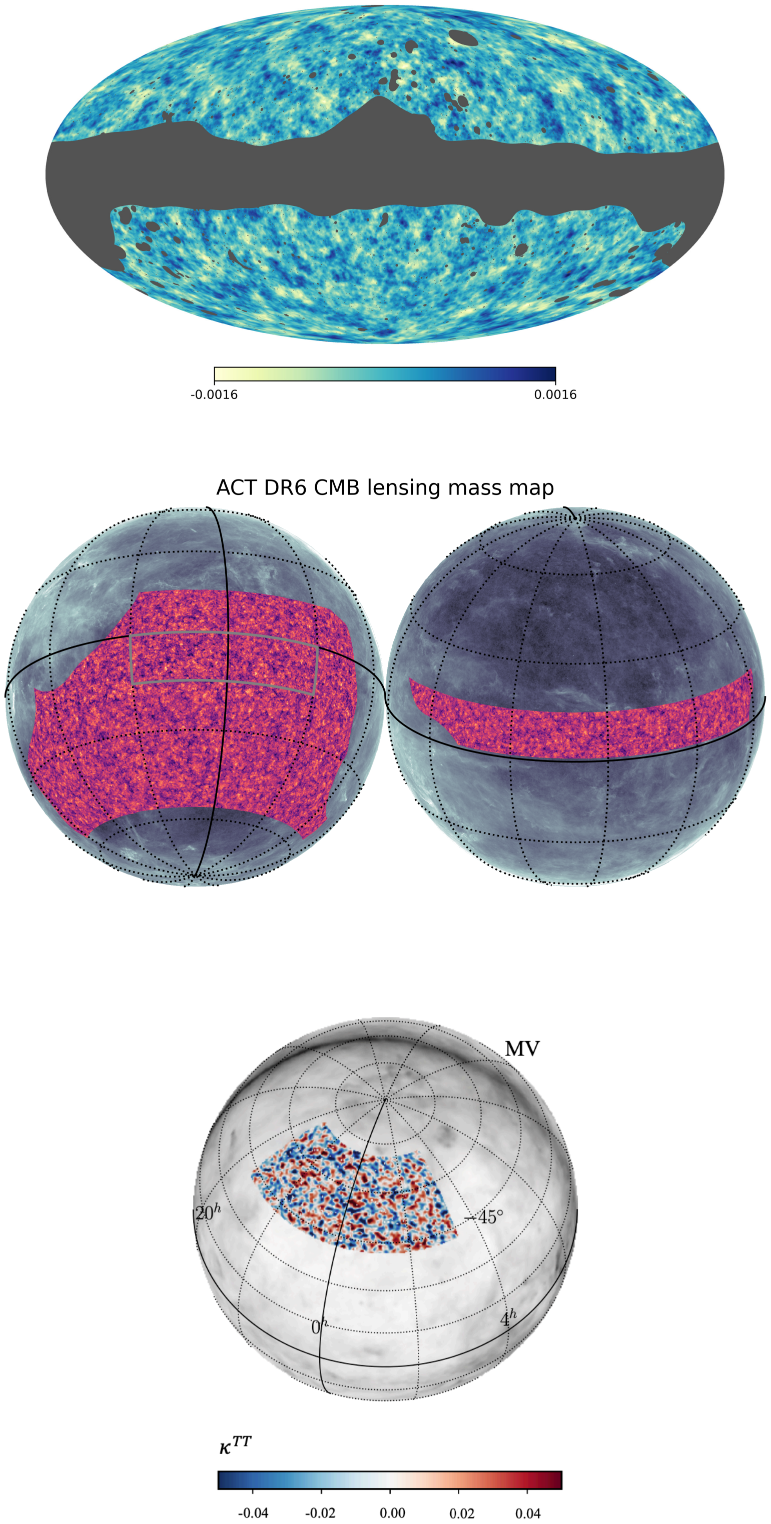
-0.0016
0.0016
ACT DR6 CMB lensing mass map
MV
20h
−45°
0h
4h
κTT
-0.04
-0.02
0.00
0.02
0.04

Figure 1.6: *Top panel*: The reconstructed lensing deflection map from *Planck*-2018 temperature and polarization data in 67% sky-fraction. Image source: [4]. *Middle Panel:* The reconstructed κ map from ACT DR6 data over 9400 deg^2 sky area. Image source [5]. *Bottom Panel:* The reconstructed κ map from SPT-3G 2018 temperature map in 1500 deg^2 sky area in the southern hemisphere. Image source [6]

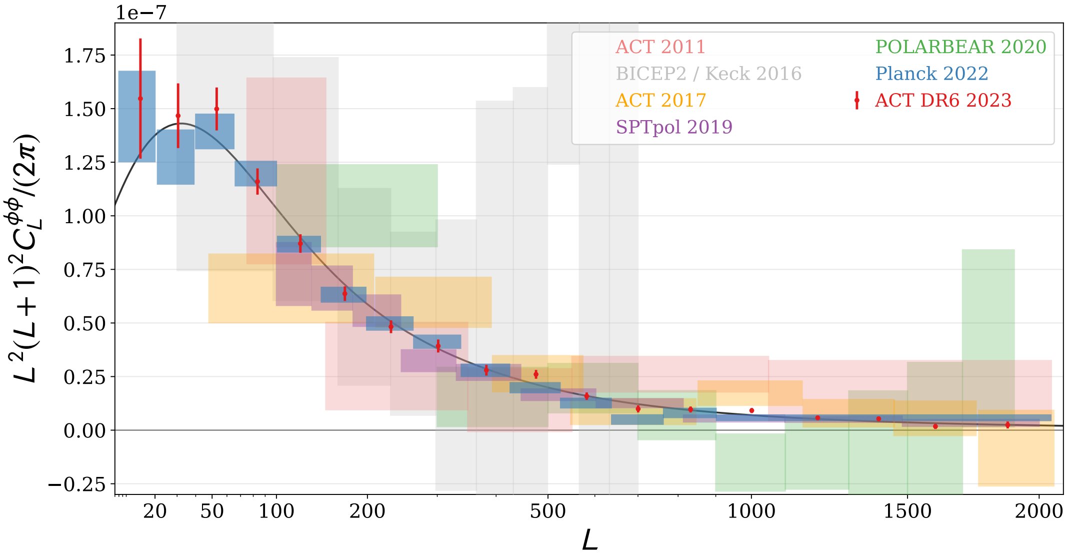

Figure 1.7: Comparison of the measured lensing potential power spectrum $C_L^{\phi\phi}$ across various probes to date. Notably, the ACT DR6 results [7] exhibit the highest signal-to-noise ratio among these measurements, closely matched by the precision of the *Planck* `NPIPE` maps [8]. Image source: [7].

for this study is the anticipation that S4 will detect approximately 10^5 clusters. This substantial number of potential detections underscores the importance of employing cluster cosmology and mass constraints derived from CMB lensing. Such methods are vital for probing cosmological parameters more accurately in future research.

1.6 Bayesian Inferences in Cosmology

A primary theme of this thesis is the application of the Bayesian framework for parameter inference. Contrasting the frequentist approach, which depends on a function of given data, Bayesian inference focuses on exploring the posterior distribution of parameters of interest. This approach is fundamentally rooted in Bayes' theorem:

$$P(\theta|d) = \frac{P(d|\theta)P(\theta)}{P(d)}. \tag{1.23}$$

Here, θ represents the parameters of our model, and d denotes the data. The probability $P(\theta|d)$ is the posterior distribution of the parameters θ, $P(d|\theta)$ is the likelihood function, representing the probability of obtaining the data for a specific parameter value. $P(\theta)$ is the prior probability, reflecting our pre-existing knowledge about the parameters before acquiring the data. $P(d)$, known as the evidence, serves as a normalization factor for the probability distribution.

This thesis primarily focuses on signals that violate the statistical isotropic nature of CMB fluctuations and generate off-diagonal terms in the covariance matrix. The first part involves the motion of the observation frame, while the second part concerns the weak-lensing of CMB photons. The posterior distribution in this context is given by:

$$P(\boldsymbol{C_S}, \boldsymbol{s}|\boldsymbol{d}) = \frac{1}{\sqrt{|2\pi \boldsymbol{C_N}||2\pi \boldsymbol{C_S}|}} \exp\left\{-\frac{1}{2}\left[(\boldsymbol{d}-\boldsymbol{s})^{\dagger}\boldsymbol{C_N}^{-1}(\boldsymbol{d}-\boldsymbol{s}) + \boldsymbol{s}^{\dagger}\boldsymbol{C_S}^{-1}\boldsymbol{s}\right]\right\} P(\boldsymbol{C_S}). \tag{1.24}$$

Here, we explore the joint posterior distribution of the signal $\boldsymbol{s}$ and the covariance matrix $\boldsymbol{C_S}$, given the data $\boldsymbol{d}$. The diagonal terms of $\boldsymbol{C_S}$ represent the power spectrum, and the off-diagonal terms contain the signal of interest. $\boldsymbol{C_N}$ is the noise covariance matrix derived from the experiment's noise information, and $P(\boldsymbol{C_S})$ is the prior distribution of the covariance matrix. For the diagonal terms or power spectrum C_l and the Doppler boost off-diagonal terms, a flat prior is typically assumed. For the lensing potential, a well-motivated Gaussian prior is used.

In the second part of the thesis, the Hamiltonian Monte Carlo (HMC) technique is employed to sample this posterior distribution, effectively addressing the curse of dimensionality. In the third part, an iterative method based on real-space Newton-Raphson scheme is utilized to find the maximum of the posterior distribution, leveraging the gradients of the distribution.

1.7 Summary

This thesis explores the utility of CMB in precision cosmology. The CMB not only serves as a direct probe of the universe's early stages but also informs us about the later stages, as the trajectories of CMB photons respond to the gravitational potential of the mass distribution of the late-time universe. Additionally, the motion of our observation frame relative to the cosmological rest frame introduces measurable effects in the CMB fluctuations. This thesis investigates two primary phenomena related to these aspects.

The second part of the thesis methodically analyzes the modulation and aberration effects resulting from the motion of the observation frame, which are scale-independent. This analysis utilizes full-sky *Planck*-2018 temperature data up to high-resolution multipoles. We report a detection of velocity from these effects, confirming the canonical value of motion derived from the CMB dipole with a statistical significance of approximately 5σ.

In the third part, the focus shifts to galaxy clusters, which are the largest gravitationally bound structures in the universe. These clusters are crucial for understanding the growth of cosmic structures and have implications for various cosmological parameters. While existing CMB surveys typically employ the quadratic estimator [36], this work incorporates the Maximum-a-Posteriori (MAP) estimator [38] for more accurate lensing potential field reconstruction in low-noise settings like CMB-S4. We demonstrate the application of this estimator to improve cluster-mass estimation using simulations.

This chapter introduces the fundamental concepts and methodologies employed throughout the thesis. It discusses the statistical isotropy of CMB fluctuations, its violation, and an introduction to the BipoSH formalism, which has been employed in the second part for analyzing the Doppler boost signal. It also outlines the basics of weak-lensing of CMB by the large-scale structure and summarizes the current state of CMB measurements. Finally, the chapter also presents the Bayesian framework for parameter inference, which underpins the analytical approach of this thesis.

Part II

Doppler Boost of Cosmic Microwave Background

Chapter 2

Overview of the Doppler Boost Model

2.1 Introduction

The isotropic and homogeneous Friedmann-Lemaître-Robertson-Walker (FLRW) cosmological model imposes a natural 3+1 decomposition of spacetime. In this model, there exists a preferred reference frame in which the four-dimensional spacetime can be described as a foliation of homogeneous and isotropic spatial hypersurfaces labeled by cosmic time. The CMB is expected to be statistically isotropic within this framework.

The relative motion of the Solar System with respect to the rest frame of the CMB modifies the statistical properties of the CMB temperature and polarization anisotropies. It is known to be the major contributor to the dipolar $\ell = 1$ fluctuation in the observed CMB anisotropy, the biggest known fluctuation in the observed CMB, which causes mK (10^{-3} K) fluctuations on the mean CMB temperature $T_0 = (2.7255 \pm 0.0006)K$ [16, 17]. The velocity of the Solar System barycentre, inferred from the CMB dipole measurement, has been found to be $v = (369\pm0.9)$ km/s in the direction $(\ell, b) = (263.99\pm0.14°, 48.26\pm0.03°)$ [16, 39–42].

Along with the well-known dipole anisotropy, this motion also causes correlation between the neighbouring spherical harmonic coefficients l and $(l \pm 1)$ of the observed CMB sky [31, 43, 44], which leads to non-zero off-diagonal terms in the harmonic space covariance matrix of temperature and polarization field, which can be captured in terms of the dipole spectra of the bipolar spherical harmonics (BipoSH) [33, 45, 46]. The Lorentz transformation of the CMB photons in our observation frame gives rise to two effects in the relative intensity fluctuations, *modulation* and *aberration*, which we jointly refer as *Doppler boost*. The first one is a frequency dependent effect that causes the CMB sky to appear brighter (or dimmer) by an amount[1] $\beta \equiv v/c = (1.23 \times 10^{-3})$ in the direction (or opposite direction) of motion. The second effect, aberration is frequency independent and results in the deflection of the original directions of the incoming CMB photons. The strength of Doppler boost varies across the sky and it depends on the projection $(\hat{\beta} \cdot \hat{n})$ of the direction of the incoming photons $(\hat{n})$ and the direction of local motion $(\hat{\beta})$. The imprints of these effects in the CMB temperature field is shown in Figure 2.1, where we plot the difference between a simulated Doppler boosted CMB map at 217 GHz (generated using `CoNIGS` [9]) with the known value of the velocity amplitude $\beta = 1.23 \times 10^{-3}$ in the known dipole direction (shown by the black plus symbol) and a statistically isotropic (SI) map generated with the same initial random seed. This difference map shows the fluctuations at all angular scales as a result of the scale-independent nature of Doppler boost. The imprints of Doppler boost vary with the sky direction by the factor $\hat{\beta} \cdot \hat{n}$. The effect is stronger in the direction (or in the opposite direction) of motion, rather in the sky directions 90° away from the direction of local motion.

Several other cosmological probes have also been used to infer the motion of the Solar System with respect to *the cosmological rest-frame*. One of the prominent probes is the number count of radio galaxies [47–49]. Radio galaxies can be observed out to cosmological distances and hence the contamination due to sample variance in the local universe can be mitigated. Various works using data of radio sources available so far have provided differing estimates of the Solar System motion [48]. However, current and next-generation radio surveys are poised to make an accurate and high significance detection [50–53]. More recently, the effect of the Solar System motion on the thermal Sunyaev-Zeldovich effect [54] of galaxy clusters [55] in *Planck* data has been used to estimate the Doppler boost signal [56].

Correlations in the CMB introduced by the Doppler boost provide an equally competitive probe of the Solar System motion. Also, it is an important cross-check of the estimate of the Solar System motion from CMB Dipole and that of consistency of the CMB data-set. For high-resolution CMB maps, the detectability of such anisotropic im-

---

[1] The speed of light in vacuum is denoted by $c = 2.997 \times 10^5$ km/s.

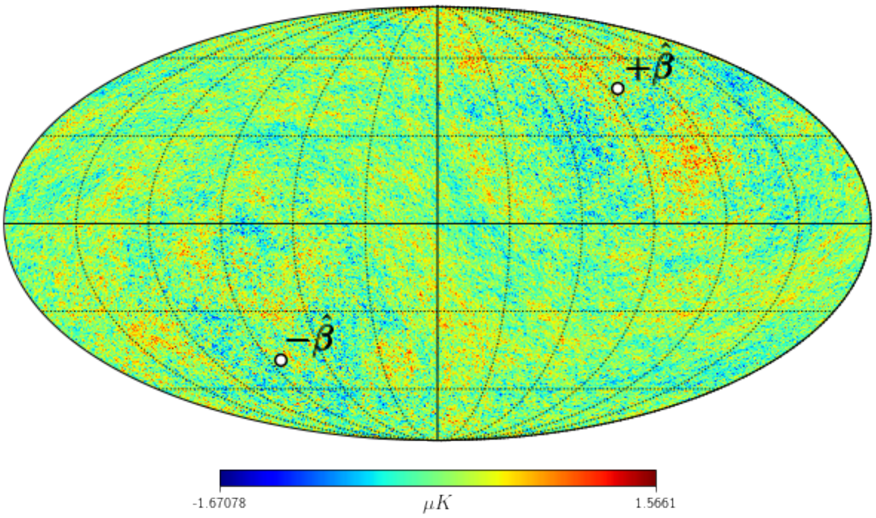

Figure 2.1: We show the difference between a simulated statistically isotropic map and a Doppler boosted map at 217 GHz generated with the same value of the initial random seed using `CoNIGS` [9] with an injected signal in the fiducial dipole direction $\ell = 264°$, $b = 48°$, with the known amplitude $v/c \equiv \beta = 1.23 \times 10^{-3}$ for the illustration purpose.

prints in the covariance matrix has been discussed in [57, 58]. The earliest detection of such SI violation due to local motion, was done by the *Planck* team [59] in 2013, using quadratic estimators proposed in [60]. Consequently, various other estimators have been used to infer the Doppler boost signal [61, 62]. The effect of these correlations on other quantities of interest in CMB studies is discussed in [63–65]. A better understanding of the Doppler boost signal is also important for determining the possible contribution of the intrinsic CMB dipole [66–68]. There are also works in the literature alluding to possible hints of an axis of evil [69, 70], which indicates strong directional alignment of the lowest multipoles CMB dipole, quadrupole and octopole along with the direction of parity asymmetry of CMB corresponding to the largest angular scale. However, our inference of the local motion has been carried out from the effects of the motion on the CMB anisotropy at significantly smaller angular scales ($l_{\text{range}} = 800 - 1950$). Hence, we can safely say that our analysis circumvents any possible contamination from the said effect and is expected not to have implications for the same.

This chapter offers a comprehensive overview of the Doppler boost model and outlines the necessary formalism for analyzing the Planck 2018 `SMICA` temperature map. The Doppler boost signal, being frequency-dependent, impacts data across different frequency channels in distinct ways. The `SMICA` CMB map amalgamates maps from nine frequency channels, introducing complexity in extracting the Doppler boost signal. To navigate this challenge, we introduce a novel parameter, the `SMICA` boost factor $b^{\texttt{SMICA}}(l)$, designed to isolate our local motion's signature from the `SMICA` map. In Section 2.2, we detail the analytical expressions for the observed fluctuation map in both real and harmonic spaces, highlighting the additional terms introduced by the Doppler boost effect. Section 2.3 delves into the derivation of the off-diagonal terms in the covariance matrix specifically for the `SMICA` map, providing the necessary analytical expressions. Finally, Section 2.4 summarizes the key points of this chapter.

2.2 Imprint of Doppler boost on CMB

We denote the CMB temperature in the direction $\hat{n}'$ in the CMB rest frame by $T'(\hat{n'})$. Our observation frame, fixed with respect to the Solar System barycentre, is moving with the velocity $\boldsymbol{\beta}$ relative to the CMB rest frame. The observed CMB temperature in the direction $\hat{n}$, $T(\hat{n})$ is given by the following expression [31],

$$T(\hat{n}) = \frac{T'(\hat{n}')}{\gamma(1 - \hat{n} \cdot \boldsymbol{\beta})}, \tag{2.1}$$

where $\gamma = (1 - \beta^2)^{-\frac{1}{2}}$ is Lorentz factor and $\beta \equiv |\boldsymbol{\beta}|$. The observed direction $\hat{n}$, in terms of $\hat{n}'$ and $\boldsymbol{\beta}$, is [31, 58, 59]

$$\hat{n} = \frac{\hat{n}' \cdot \hat{\beta} + \beta}{1 + \hat{n}' \cdot \boldsymbol{\beta}}\hat{\beta} + \frac{\hat{n}' - (\hat{n}' \cdot \hat{\beta})\hat{\beta}}{\gamma(1 + \hat{n}' \cdot \boldsymbol{\beta})}. \tag{2.2}$$

Expanding the observed temperature $T(\hat{n})$ up to linear order in β, the observed temperature fluctuations (excluding the CMB dipole) can be derived to be [44, 59]

$$\delta T(\hat{n}) = \delta T'(\hat{n} - \nabla(\hat{n} \cdot \boldsymbol{\beta}))(1 + \hat{n} \cdot \boldsymbol{\beta}). \tag{2.3}$$

The *Planck* detectors measure the intensity fluctuations at nine frequency channels. The intensity of CMB radiation at frequency ν is [43, 59]

$$I_\nu(\hat{n}) = \frac{2h\nu^3}{c^2}\frac{1}{\exp[h\nu/k_B T(\hat{n})] - 1}. \tag{2.4}$$

Hence, the temperature fluctuation $\delta T(\hat{n})_I$ inferred from the intensity fluctuation $\delta I_\nu(\hat{n})$ at frequency ν is [44, 59]

$$\delta T(\hat{n})_I = \frac{\delta I_\nu(\hat{n})}{dI_\nu/dT|_{T_0}} = \delta T'(\hat{n} - \nabla(\hat{n}\cdot\boldsymbol{\beta}))(1 + b_\nu \hat{n}\cdot\boldsymbol{\beta}), \tag{2.5}$$

where the frequency dependent boost factor b_ν has the following form

$$b_\nu = \frac{\nu}{\nu_0}\coth\left(\frac{\nu}{2\nu_0}\right) - 1. \tag{2.6}$$

Here, ν_0 refers to the characteristics frequency corresponding to the CMB monopole temperature T_0, defined as:

$$\nu_0 \equiv \frac{k_B T_0}{h} \approx 57\ \text{GHz}, \tag{2.7}$$

where k_B is Boltzmann's constant and h is Planck's constant.

We carry out the whole analysis in the spherical harmonic space. For given $\boldsymbol{\beta}$, $D(\hat{n})$ represents the dipole field[2], which has a form $\boldsymbol{\beta}\cdot\hat{n}$. In the spherical harmonic basis

$$D(\hat{n}) \equiv \boldsymbol{\beta}\cdot\hat{n} = \sum_{N=-1}^{1} \beta_{1N} Y_{L=1,N}(\hat{n}), \tag{2.8}$$

where the peculiar velocity vector $\boldsymbol{\beta}$ has an amplitude β and a direction $\hat{\beta} \equiv (\theta_\beta, \phi_\beta)$ in the real space. For convenience, we use β_{10}, the real part of β_{11} (β^r_{11}) and the imaginary part β_{11} (β^i_{11}) as three real valued independent variables in our analysis. The real space variables, β, θ_β and ϕ_β are related to the spherical harmonic coefficients of the dipole field as [11],

$$\begin{aligned}
\beta &= \sqrt{\frac{3}{4\pi}}\sqrt{\beta_{10}^2 + 2\beta_{11}^{r2} + 2\beta_{11}^{i2}},\\
\theta_\beta &= \cos^{-1}\left(\frac{\beta_{10}}{\beta}\sqrt{\frac{3}{4\pi}}\right),\\
\phi_\beta &= -\tan^{-1}\left(\frac{\beta^i_{11}}{\beta^r_{11}}\right).
\end{aligned} \tag{2.9}$$

We assume that the CMB sky is statistically isotropic in its rest frame. We simplify Eq. 2.5 and calculate the a_{lm}'s for our boosted observation frame, in terms of the $\tilde{a}_{lm}$'s for the SI CMB rest frame. Up to linear order in β, [44]

---

[2] Since D($\hat{n}$) is a real-valued function, the coefficients β_{11} and β_{1-1} are related as $\beta^*_{1-1} = -\beta_{11}$.

$$\delta T(\hat{n}) = (1 + b_\nu \hat{n}\cdot\boldsymbol{\beta})(\delta T'(\hat{n}) - \nabla_i \delta T'(\hat{n})\nabla^i(\hat{n}\cdot\boldsymbol{\beta})). \tag{2.10}$$

Expressing the above equation in spherical harmonic space, we get

$$\begin{aligned} a_{lm} = \tilde{a}_{lm} + b_\nu \sum_{N=-1}^{1} \beta_{1N} \sum_{l'm'} \tilde{a}_{l'm'} (-1)^m \frac{\Pi_{l'l}}{\sqrt{12\pi}} C^{10}_{l'0l0} C^{1N}_{l'm'l-m} \\ - \sum_{N=-1}^{1} \beta_{1N} \sum_{l'm'} \tilde{a}_{l'm'} \frac{1}{2}[l'(l'+1) - l(l+1) + 2](-1)^m \frac{\Pi_{l'l}}{\sqrt{12\pi}} C^{10}_{l'0l0} C^{1N}_{l'm'l-m}, \end{aligned} \tag{2.11}$$

where the spherical harmonic coefficients of the SI CMB sky are $\tilde{a}_{lm} = \int \delta T^{\mathrm{SI}}(\hat{n}) Y_{lm}(\hat{n}) d\Omega_{\hat{n}}$. $C^{LN}_{l'm'lm}$ denote the Clebsch-Gordan coefficients and $\Pi_{l_1 l_2 \ldots l_n} \equiv \sqrt{(2l_1+1)(2l_2+1)\ldots(2l_n+1)}$ [35]. This is the expression of a_{lm}'s for a Doppler boosted CMB map at frequency ν. Key aspects of the expression are that the non-SI corrections of a_{lm}'s due to local motion have a dependence on isotropic temperature field $\tilde{a}_{lm}$'s and the corrections are frequency dependent through the boost factor b_ν. In the next section, we will exhibit how these non-SI corrections generate non-zero off-diagonal terms in the harmonic space CMB covariance matrix.

2.3 Covariance matrix of Doppler boosted CMB temperature map

We use the `SMICA` estimate of the CMB temperature anisotropy map provided by *Planck*. The `SMICA` method makes use of maps in all nine frequency channels [71, 72]. However, for the *Planck*-2018 SMICA map, not all the data from all the channels are used for the whole sky. Though `SMICA` is a harmonic space method, for the *Planck* 2018 release, it makes use of a real space filter in the form of a mask along with a harmonic space filter [73]. The `SMICA` map provided in the 2018 data release of the *Planck* is constructed as summarised in the following expression [73]

$$X_{\texttt{SMICA}} = X_{\mathrm{full}} + P(X_{\mathrm{high}} - X_{\mathrm{full}}), \tag{2.12}$$

where X_{full} and X_{high} have the following form,

$$X_{\text{full}}(\hat{n}) = \sum_{\nu}^{\text{full}} \sum_{lm} a_{lm}^{\nu} Y_{lm}(\hat{n}) W_{\nu}^{\text{full}}(l),$$
$$X_{\text{high}}(\hat{n}) = \sum_{\nu}^{\text{high}} \sum_{lm} a_{lm}^{\nu} Y_{lm}(\hat{n}) W_{\nu}^{\text{high}}(l). \tag{2.13}$$

In the above expressions, "full" stands for all the nine *Planck* frequency channels and "high" stands for only the six HFI frequency channels. The weights $W_{\nu}^{\text{full}}(l)$ and $W_{\nu}^{\text{high}}(l)$ are defined and given by *Planck*[3], and has been presented in Figure 2.2. The operator P in Eq. 2.12, is a hybridization of two operators. One is an apodized galactic mask M[4], the other one is an apodized high-pass filter $\mathcal{F}$ in harmonic space. $\mathcal{F}$ has the following functional form[5],

$$\begin{aligned}
\mathcal{F} &= 0 && \text{for } l < l_1, \\
&= \frac{1}{2} - \frac{1}{2}\cos\left[\frac{\pi(l - l_1)}{l_2 - l_1}\right] && \text{for } l_1 \leq l \leq l_2, \\
&= 1 && \text{for } l > l_2.
\end{aligned} \tag{2.14}$$

So the combined effect of the operator P is as follows. In masked regions of CMB sky, where $M = 0$, $X_{\texttt{SMICA}} = X_{\text{full}}$. In unmasked regions, where $M = 1$, for $l < l_1$, $X_{\texttt{SMICA}} = X_{\text{full}}$ and for $l > l_2$, $X_{\texttt{SMICA}} = X_{\text{high}}$. In the `SMICA` pipeline, $l_1 = 50$ and $l_2 = 150$ values are used[5]. As long as we consider regions where $M = 1$ and l_{range} over 150, it is safe to approximate $X_{\texttt{SMICA}} = X_{\text{high}}$. The a_{lm}'s of `SMICA` map ($a_{lm}^{\texttt{SMICA}}$), in terms of the a_{lm}'s of the single frequency maps (a_{lm}^{ν}) is then

$$a_{lm}^{\texttt{SMICA}} = \sum_{\nu}^{\text{high}} W_{\nu}^{\text{high}}(l) a_{lm}^{\nu}. \tag{2.15}$$

---

[3] `weights_T_smica_R3.00_Xfull.txt` and `weights_T_smica_R3.00_Xhigh.txt` in `COM_Code_SMICA-weights-propagation_R3.00.tar.gz` available in https://wiki.cosmos.esa.int/planck-legacy-archive/index.php/SMICA_propagation_code

[4] `transition_mask.fits.gz` in `COM_Code_SMICA-weights-propagation_R3.00.tar.gz`

[5] See `smica_coadd.py` in `COM_Code_SMICA-weights-propagation_R3.00.tar.gz`

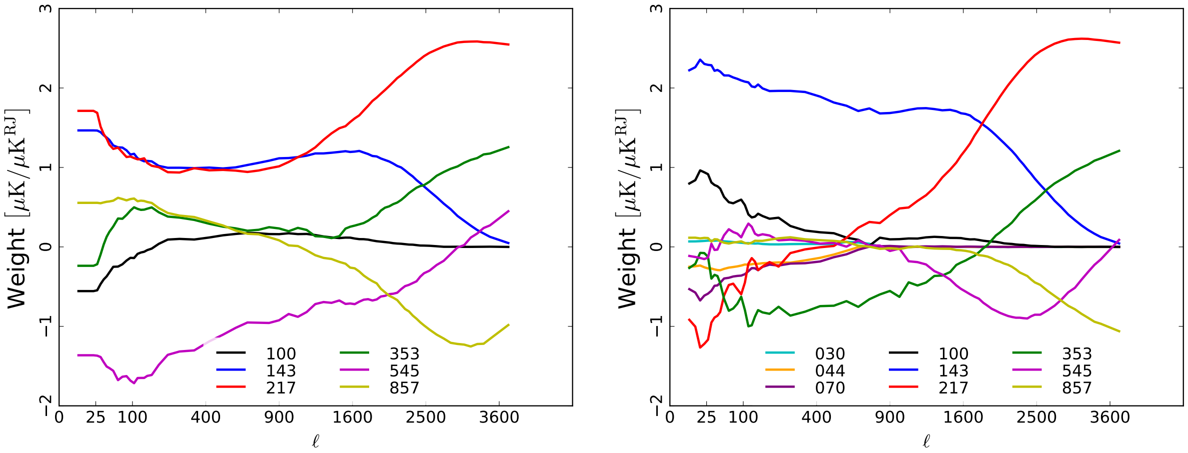

Figure 2.2: The harmonic space `SMICA` weights used to construct the temperature maps $X_{\rm high}(\hat{n})$ (left panel) and $X_{\rm full}(\hat{n})$ (right panel), as mentioned in Eq. 2.13. Image source: [10]

Using the expression in Eq. 2.11 of the a_{lm}'s for the boosted single channels in Eq. 2.15, we get the expression of a_{lm}'s of boosted `SMICA` map

$$a_{lm}^{\tt SMICA} = \tilde{a}_{lm}^{\tt SMICA} + b_{lm}^{\tt SMICA} \sum_{N=-1}^{1} \beta_{1N} \sum_{l'm'} \tilde{a}_{l'm'}^{\tt SMICA} (-1)^m \frac{\Pi_{l'l}}{\sqrt{12\pi}} C_{l'0l0}^{10} C_{l'm'l-m}^{1N}$$
$$- \sum_{N=-1}^{1} \beta_{1N} \sum_{l'm'} \tilde{a}_{l'm'}^{\tt SMICA} (-1)^m \frac{1}{2} [l'(l'+1) - l(l+1) + 2] \frac{\Pi_{l'l}}{\sqrt{12\pi}} C_{l'0l0}^{10} C_{l'm'l-m}^{1N}, \tag{2.16}$$

which is a reduced form similar to a single channel expression, but with a boost factor $b_{lm}^{\tt SMICA}$, given by

$$b_{lm}^{\tt SMICA} \equiv \frac{\sum_{\nu}^{\rm high} b_\nu W_\nu^{\rm high}(l) a_{lm}^\nu}{a_{lm}^{\tt SMICA}}. \tag{2.17}$$

We calculate this $b_{lm}^{\tt SMICA}$ from the six HFI frequency channels, with the aid of publicly available `SMICA` propagation code[5]. We choose the most probable values from the $b_{lm}^{\tt SMICA}$ distributions of $(2l+1)$ modes at every multipole l, to obtain $b^{\tt SMICA}(l)$[6]. The value chosen as $b^{\tt SMICA}(l)$ makes sure that it is a representative values for most of the $b_{lm}^{\tt SMICA}$ values at a fixed l. The non-SI corrections of $a_{lm}^{\tt SMICA}$ due to local motion in Eq. 2.16 are constituted from all the quantities that are accessible to us through the `SMICA` map. For our analysis, we compute $b^{\tt SMICA}(l)$ for three different choices of masks shown in Figure 2.3. The increase

---

[6] We avoid using the mean value of $b_{lm}^{\tt SMICA}$, as it is going to be driven by the extended tail of the distribution.

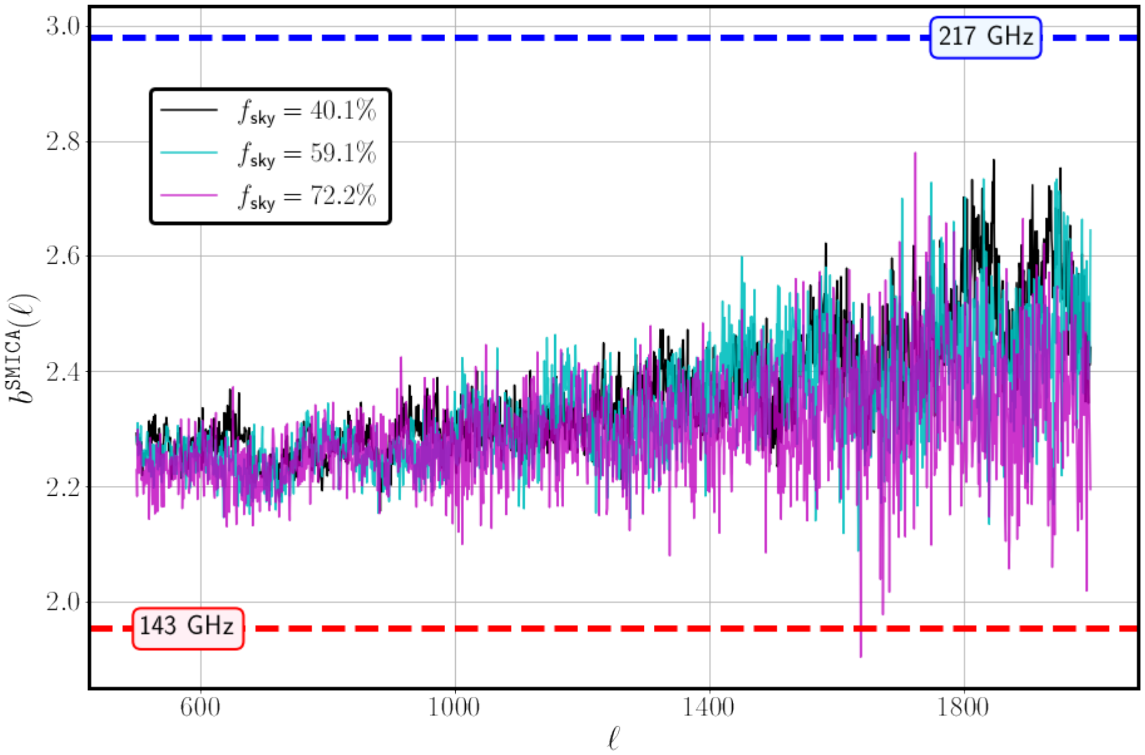

Figure 2.3: In this figure we show the `SMICA` boost factor $b^{\mathtt{SMICA}}(l)$ for 3 different masks, $f_{\rm sky} = 40.1\%$ (black curve), 59.1% (cyan curve) and 72.2% (magenta curve), which are depicted in Figure 4.1. $b^{\mathtt{SMICA}}(l)$ corresponding to each mask is obtained by taking the peaks of histograms of $b^{\mathtt{SMICA}}_{lm}$ (we have $(2l+1)$ modes at each l). As a reference, the red and the blue lines show the boost factor b_ν for the *CMB channels*, 143 GHz and 217 GHz, respectively.

in the value of $b^{\mathtt{SMICA}}(l)$ at high l arises due to larger value of the `SMICA` weights for the frequency channel 217 GHz at values of $l \geq 1600$ [73].

We use Eq. 2.16 to compute the covariance matrix elements for the `SMICA` map due to the Doppler boost. Up to leading order in β,[7]

$$\begin{aligned}\langle a_{lm}a^*_{l'm'}\rangle =& C_l\delta_{ll'}\delta_{mm'} \\ &+(-1)^{m'}\frac{\Pi_{ll'}}{\sqrt{12\pi}}\sum_{N=-1}^{1}\beta_{1N}[(b^{\mathtt{SMICA}}(l)-\frac{1}{2}\{l(l+1)-l'(l'+1)+2\})C_l \\ &+(b^{\mathtt{SMICA}}(l')-\frac{1}{2}\{l'(l'+1)-l(l+1)+2\})C_{l'}]C^{10}_{l0l'0}C^{1N}_{lml'-m'}. \qquad (2.18)\end{aligned}$$

---

[7] $\langle . \rangle$ denotes the ensemble average.

A few important aspects of this expression are as follows. The first term in Eq. 2.18, provides the diagonal elements C_l's, which come from the $\tilde{a}_{lm}^{\texttt{SMICA}}$'s in Eq. 2.16. The second term in Eq. 2.18, represents the leading order off-diagonal terms, that are linear in β. If the velocity of our local motion β were zero, then the β_{1N}'s would have been zero and we would have been left with a diagonal covariance matrix as expected for a SI sky. The off-diagonal part has a dependence on the C_l's, which again reinforces the point that joint analysis of local motion variables along with the C_l's, is essential. There is a correction in the diagonal terms as well, if we include the next order for β in our calculation. We have ignored the corrections to C_l due to local motion in this analysis, as it can lead to a maximum relative difference in its value by about a few times 10^{-3}– 10^{-4} for the partial-sky analysis relevant for this work (with a minimum $f_{\text{sky}} = 40.1\%$) [64, 65, 74, 75]. These values are sub-dominant in comparison to the total uncertainties (cosmic variance + Planck instrument noise [76]) in the value of C_l at high multipole values considered in this analysis [77]. However, for future high-resolution and more sensitive CMB experiments, higher-order terms will play a crucial role and cannot be ignored [64, 65].

Any particular cause behind the violation of SI of the CMB manifests through non-zero values of only certain off-diagonal terms in the covariance matrix. BipoSH coefficients ($A^{LN}_{l_1 l_2}$) provide an elegant way to group these particular terms according to the nature of the isotropy violating correlations, organizing them according to how they transform under rotations [78]. The elements of the covariance matrix can be written as a linear combination of the BipoSH coefficients,

$$\langle a_{lm} a^*_{l'm'} \rangle = (-1)^{m'} \sum_{LN} A^{LN}_{ll'} C^{LN}_{lml'-m'}. \tag{2.19}$$

The BipoSH coefficients form a complete basis for expressing all the terms in the covariance matrix. In particular, the diagonal elements of the covariance matrix are just the $L = 0$, $M = 0$ terms of the BipoSH coefficients, given by

$$A^{00}_{ll'} = (-1)^l \sqrt{2l+1} C_l \delta_{ll'}. \tag{2.20}$$

The Clebsch-Gordon coefficients in Eq. 2.18 limit the number of off-diagonal terms we get in the covariance matrix for a boosted sky. We get only the mixing of l and $l \pm 1$ terms.

Therefore the diagonal terms and just the immediately adjacent terms on both sides of the diagonal terms in the covariance matrix are non-zero. As the BipoSH coefficients for this case are symmetric under the exchange of lower indices, l and $l+1$, we only need the $A^{1N}_{l,l+1}$ terms to express all the off-diagonal terms. We compare Eq. 2.18 and Eq. 2.19 to get the expression of the BipoSH coefficients as

$$A^{1N}_{l,l+1} = \beta_{1N}\mathcal{S}_{l,l+1}, \tag{2.21}$$

where β_{1N} is the amplitude of the Doppler boost signal and $\mathcal{S}_{l,l+1}$ is called the *shape factor* which is defined as,

$$\mathcal{S}_{l,l+1} \equiv \frac{\Pi_{l,l+1}}{\sqrt{12\pi}}[(l + b^{\texttt{SMICA}}(l))C_l - (l + 2 - b^{\texttt{SMICA}}(l+1))C_{l+1}]C^{10}_{l0l+10}. \tag{2.22}$$

We use this particular form of the shape factor in our analysis to extract the Doppler boost signal from the *Planck*-2018 `SMICA` temperature map [77].

2.4 Summary

The motion of our observation frame introduces significant effects on the CMB observations. At the largest scales, this motion results in the Doppler boost of the CMB monopole, creating an observable dipole pattern. Beyond these large scales, our motion also influences the fluctuations at smaller angular scales through modulation and aberration effects. Modulation amplifies the brightness of fluctuations in the direction of motion while dimming them in the opposite direction. Aberration, on the other hand, deflects the original trajectory of incoming photons. These are purely relativistic effects stemming from our motion. Although it is challenging to isolate an intrinsic dipole component from the observed CMB dipole, we can infer our velocity through these relativistic effects on smaller angular scales. This approach helps in constraining the potential contribution of an intrinsic dipole at the milli-Kelvin (mK) scale.

As discussed in this chapter, these small-scale effects violate the statistical isotropy of the fluctuations, introducing off-diagonal terms in the CMB covariance matrix in spherical harmonic space. Specifically, the Doppler boost causes correlations between adjacent multipoles (a_{lm} and $a_{l\pm1m}$), resulting in non-zero off-diagonal terms in the covariance matrix. We represent these correlations using the BiPoSH formalism. The correlation strength is scale-independent, unlike the modulation due to Cosmic Hemispherical Asymmetry (CHA) [32], which is scale-dependent and predominant at larger scales or lower l values [11]. Therefore, we focus our analysis on high CMB multipole ranges to minimize CHA contamination, as elaborated in Chapter 4 (Section 4.2). Another key aspect of the Doppler boost signal, as outlined in this chapter, is its frequency dependence. Different frequency channel maps exhibit varying signal strengths. We utilize the *Planck*-2018 `SMICA` temperature map, which combines all frequency channels using optimized weights in harmonic space. This comprehensive approach enhances our analysis, yielding better detection significance than previous studies.

The parameters of interest in this estimation problem are the complete covariance matrix and the signal a_{lm}. The off-diagonal terms consist of both the power spectrum C_l and the spherical harmonic coefficients of the dipole field (β_{10}, β^r_{11}, and β^i_{11}), as indicated in Eq. 2.18. A Bayesian approach is adopted to explore the joint posterior distribution of these parameters. To address the high dimensionality challenge, Hamiltonian Monte-Carlo (HMC) sampling is employed. The methodology and the ensuing posterior distribution are comprehensively discussed in the subsequent chapter.

Chapter 3

Methodology

3.1 Introduction

In the previous chapter, we explored how the Doppler boost, resulting from the motion of the observation frame, introduces observable effects in CMB data. These effects manifest as off-diagonal terms in the CMB covariance matrix. Building on the model of these off-diagonal terms, it is possible to develop a minimum variance quadratic estimator, as outlined by [60], to infer the velocity of the observation frame from the data. This approach has been successfully applied to derive the motion from the *Planck*-2013 data set [79].

In this work, we analyze *Planck*-2018 `SMICA` temperature map [77] in the BipoSH framework [44]. Our approach involves a joint Bayesian inference to simultaneously determine the CMB power spectrum (C_l), the dipolar ($L = 1$) BipoSH coefficients (which encapsulate the off-diagonal terms induced by local motion), and the temperature field in spherical harmonic space (a_{lm}). As elaborated in Section 2.3, this comprehensive inference is necessitated owing to the fact that the non-SI off-diagonal part of the harmonic space covariance matrix is influenced by the SI diagonal part. Due to high dimensional parameter space, we employ the *Hamiltonian Monte-Carlo* (HMC) method [80] to explore the posterior distribution of our model parameters, i.e., the Doppler boost signal, C_l's and a_{lm}'s of the CMB map. We use the inference formalism developed in [11, 81].

This chapter presents an in-depth explanation of the methodology employed in this study. In Section 3.2, we delve into the specifics of the data model, including a discussion on the likelihood and prior distributions. This section finally provides the expression of the posterior distribution, which we want to explore. Following this, Section 3.3 is dedicated to the HMC sampling technique. Here, we outline the foundational principles of the HMC sampler and present the expressions for the momentum derivatives of the parameters concerned, which are essential for executing the sampling process. The chapter concludes with a summary in Section 3.4, encapsulating the key points discussed.

3.2 Data Model and the Parameter Posterior

We use the following model for the data $\boldsymbol{d}$ [8],

$$\boldsymbol{d} = \boldsymbol{\mathcal{B}}\boldsymbol{s} + \boldsymbol{N}, \tag{3.1}$$

where $\boldsymbol{s}$ is the CMB signal vector, $\boldsymbol{N}$ is the noise vector and $\boldsymbol{\mathcal{B}}$ is the beam convolution operator. We assume the noise to be Gaussian [77,82]. Hence, the probability of the data $\boldsymbol{d}$ given signal $\boldsymbol{s}$ is

$$\mathcal{P}(\mathbf{d}|\boldsymbol{s}) = \frac{1}{\sqrt{|2\pi \boldsymbol{C_N}|}} \exp\Big[-\frac{1}{2}(\boldsymbol{d}-\boldsymbol{s})^\dagger \boldsymbol{C_N}^{-1}(\boldsymbol{d}-\boldsymbol{s})\Big], \tag{3.2}$$

where, $\boldsymbol{C_N}$ is the noise covariance matrix. We want to sample the joint posterior distribution of the parameters a_{lm}, C_l and β_{1N}. Using the probability distributions given above, we can express the posterior distribution of a_{lm}, C_l and β_{1N} as

$$\mathcal{P}(\boldsymbol{C_S}, \boldsymbol{s}|\boldsymbol{d}) = \frac{\mathcal{L}(\boldsymbol{d}|\boldsymbol{s}, \boldsymbol{C_S})\Pi(\boldsymbol{s}, \boldsymbol{C_S})}{\mathcal{E}(\boldsymbol{d})}, \tag{3.3}$$

where $\mathcal{L}$ is the likelihood, $\mathcal{E}$ is the evidence and Π is the prior. For the likelihood, conditioned on $\boldsymbol{s}$, $\boldsymbol{d}$ is independent of $\boldsymbol{C_S}$, implying $\mathcal{L}(\boldsymbol{d}|\boldsymbol{s}, \boldsymbol{C_S}) = \mathcal{L}(\boldsymbol{d}|\boldsymbol{s})$. Hence, we have

$$\mathcal{P}(\boldsymbol{C_S}, \boldsymbol{s}|\boldsymbol{d}) = \frac{\mathcal{L}(\boldsymbol{d}|\boldsymbol{s})\Pi(\boldsymbol{s}|\boldsymbol{C_S})\Pi(\boldsymbol{C_S})}{\mathcal{E}(\boldsymbol{d})}, \tag{3.4}$$

where we used $\Pi(\boldsymbol{s}, \boldsymbol{C_S}) = \Pi(\boldsymbol{s}|\boldsymbol{C_S})\Pi(\boldsymbol{C_S})$. For the prior on the signal amplitude $\Pi(\boldsymbol{s}|\boldsymbol{C_S})$, we use the theoretically motivated and empirically established fact that the Gaussianity of the CMB fluctuations is a very good approximation [83–86]. Hence,

$$\Pi(\boldsymbol{s}|\boldsymbol{C_S}) = \frac{1}{\sqrt{|2\pi \boldsymbol{C_S}|}} \exp\Big[-\frac{1}{2}\boldsymbol{s}^\dagger \boldsymbol{C_S}^{-1}\boldsymbol{s}\Big]. \tag{3.5}$$

---

[8] We denote vectors and matrices by bold symbol.

In the above equations, $\mathcal{E}(\boldsymbol{d})$ is the Evidence of the data and is a normalization constant. The explicit expression for the Evidence for this problem would be

$$\mathcal{E}(\boldsymbol{d}) = \int \boldsymbol{dC_S ds}\mathcal{L}(\boldsymbol{d}|\boldsymbol{s})\Pi(\boldsymbol{s}|\boldsymbol{C_S})\Pi(\boldsymbol{C_S}). \tag{3.6}$$

Evidence is generally computed for the purpose of model comparison. However, for the probability distributions we consider, brute force computation of the evidence is intractable. Instead, we bypass explicit computation of the above integration by using the Savage Dickey Density Ratio [87] to perform model comparison in Section 5. $\Pi(\boldsymbol{C_S})$ is now the prior on the CMB signal covariance matrix and we assume it to be flat. The robustness of analysis for different choices of prior has been discussed in [11], for similar scenario. Hence, the probability distribution to be sampled has the same functional form as $\mathcal{P}(\boldsymbol{d}|\boldsymbol{s})\mathcal{P}(\boldsymbol{s}|\boldsymbol{C_S})$, explicitly expressed as

$$\mathcal{P}(\boldsymbol{C_S}, \boldsymbol{s}|\boldsymbol{d}) = \frac{1}{\sqrt{|2\pi \boldsymbol{C_N}||2\pi \boldsymbol{C_S}|}} \exp\left\{ -\frac{1}{2}\Big[(\boldsymbol{d}-\boldsymbol{s})^\dagger \boldsymbol{C_N}^{-1}(\boldsymbol{d}-\boldsymbol{s}) + \boldsymbol{s}^\dagger \boldsymbol{C_S}^{-1}\boldsymbol{s}\Big]\right\}. \tag{3.7}$$

Note that the dependence of the posterior distribution on the parameters a_{lm}, C_l and β_{1N} is through the signal vector $\boldsymbol{s}$ and the signal covariance matrix $\boldsymbol{C_S}$. The above formalism presents the Bayesian hierarchical model for the problem at hand. The a_{lm} form one set of model parameter which are directly compared with the data. Parameters of the signal covariance matrix form another set of parameters at a different level of hierarchy.

Given the large number of parameters, we use the Hamiltonian Monte Carlo (HMC) method [80, 88] to jointly sample the posterior distribution $\mathcal{P}(\boldsymbol{C_S}, \boldsymbol{s}|\boldsymbol{d})$. The details of the sampling of this particular distribution, using the language of BipoSH coefficients to describe the covariance matrix, are discussed in [11, 81]. Details of the particular methodology used here are discussed in [11] in the context of dipole modulation (cosmic hemispherical asymmetry) of CMB temperature anisotropy [83–85, 89]. We adopt this formalism for the inference of the Doppler boost signal. In the next section, we describe HMC in brief and provide some of the relevant mathematical expressions.

3.3 Sampling method: Hamiltonian Monte Carlo

HMC is an efficient Monte Carlo sampling method and makes use of the Hamiltonian dynamics to propose the sample [80, 88]. Further, HMC avoids the curse of dimensionality that affects the Metropolis algorithm, especially for high dimensional inference and therefore potentially achieves much higher acceptance probability for proposed samples in the chain. HMC has been used in cosmology research for various challenging inference problems with hierarchical Bayesian models; some examples are cosmological parameter estimation [90], CMB power spectrum inference [91], various inference problems in large scale structure [92–94], and inference of CMB lensing potential [95, 96].

The Hamiltonian is defined as

$$\mathcal{H}(\{q_i, p_i\}) = \frac{1}{2}\boldsymbol{p}^T\boldsymbol{\mu}^{-1}\boldsymbol{p} - \ln[\mathcal{P}(\boldsymbol{q})], \tag{3.8}$$

where $\boldsymbol{q}$ is a vector of the parameters of interest, $\boldsymbol{p}$ is a vector of the momentum associated with the parameters and $\boldsymbol{\mu}$ is the *mass matrix*. The term $-\ln[\mathcal{P}(\boldsymbol{q})]$ is called the *potential energy* for the distribution being sampled, here denoted by $\mathcal{P}(\boldsymbol{q})$. For our problem, $\mathcal{P}(\boldsymbol{q})$ is given by the expression in Eq. 3.7. Hamilton's equations are

$$\dot{q} \equiv \frac{dq}{dt} = \frac{\partial \mathcal{H}}{\partial p} \quad \text{and} \quad \dot{p} \equiv \frac{dp}{dt} = -\frac{\partial \mathcal{H}}{\partial q}. \tag{3.9}$$

The main calculation involved in HMC concerns the evaluation of the momentum derivative for the parameters of interest. Hence, one needs to get the following quantity for all the parameters of interest

$$\dot{p_j} \equiv \frac{dp_j}{dt} = -\frac{\partial \mathcal{H}}{\partial q_j} = \frac{\partial \ln[\mathcal{P}(\{q_i\})]}{\partial q_j}. \tag{3.10}$$

For our problem, the expression for the momentum derivative can be obtained analytically. In the remaining section, we present calculations of $\frac{\partial \ln[\mathcal{P}(\{q_i\})]}{\partial q}$, with $q = \{a_{lm}, C_l, \beta_{1N}\}$.

The momentum derivative corresponding to a_{lm} is given by

$$\dot{p}_{lm} = -\frac{1}{2}\sum_{l_1 m_1}[\boldsymbol{C}_{\boldsymbol{S}}^{-1}]_{l_1 m_1 l m} a^*_{l_1 m_1} + \frac{1}{2}\sum_{l_1 m_1}[\boldsymbol{C}_{\boldsymbol{N}}^{-1}]_{l_1 m_1 l m}(d^*_{l_1 m_1} - a^*_{l_1 m_1}). \tag{3.11}$$

To deal with the mask, we express the probability distribution of the data given signal using real space representation of the data and the signal. The joint likelihood for the signal in N_{pix} pixels is

$$\mathcal{P}(\boldsymbol{s}|\boldsymbol{d}) = \frac{1}{|2\pi \boldsymbol{C_N}|^{1/2}} \exp\Big[-\frac{1}{2}\sum_{i=1}^{N_{pix}} \frac{(d_i - \mathcal{B}s_i)^2}{\sigma_i^2} \Big], \tag{3.12}$$

where $\mathcal{B}s_i$ is the signal in the i^{th} pixel of the map smoothed with the beam $\mathcal{B}$ and σ_i^2 is the noise variance in the i^{th} pixel. To accommodate the presence of mask, we express $\dot{p}_{lm}$ in the following form

$$\dot{p}_{lm} = -\frac{1}{2}\sum_{l_1 m_1} S^{-1}_{l_1 m_1 l m} a^*_{l_1 m_1} + \frac{1}{2}\sum_{i=1}^{N_{pix}} \frac{1}{\sigma_i^2}\Big[\sum_{l'm'} (d_{l'm'} - b_l p_l a_{l'm'}) b_l p_l Y_{l'm'}(\hat{n}_i)\Big] Y_{lm}(\hat{n}_i). \tag{3.13}$$

The momentum derivative corresponding to the BipoSH coefficient $A^{LM}_{ll'}$ is [11]

$$\begin{aligned} \dot{p}^{LN}_{ll'} = & - \frac{1}{2}\sum_{m'} \frac{(-1)^{m'}}{D_{l'm'l'm'}} C^{LN}_{lm'l'-m'} \delta_{ll'} \\ & - \frac{1}{2}\sum_{m',m} \frac{(-1)^{m'} O_{l'm'lm}}{D_{l'm'l'm'} D_{lmlm}} C^{LN}_{lml'-m'} + \frac{1}{2}\sum_{m',m} \frac{(-1)^{m'} a_{l'm'} a^*_{lm}}{D_{l'm'l'm'} D_{lmlm}} C^{LN}_{lml'-m'}. \end{aligned} \tag{3.14}$$

In particular, the momentum derivative for the BipoSH coefficient with $L = 0, M = 0$ is

$$\dot{p}^{00}_{ll'} = \frac{2l+1}{2A^{00}_{ll}} (\frac{\hat{A}^{00}_{ll'}}{A^{00}_{ll}} - 1), \quad \text{where} \quad \hat{A}^{00}_{ll'} = \sum_{mm'} a_{lm} a^*_{l'm'} C^{00}_{lml'm'}. \tag{3.15}$$

The momentum derivative with respect to β_{1N} parameter is

$$\frac{\partial \mathcal{H}}{\partial \beta_{1N}} = \sum_l \Big[\frac{\partial A^{1N}_{ll+1}}{\partial \beta_{1N}} \frac{\partial \mathcal{H}}{\partial A^{1N}_{ll+1}} + \frac{\partial A^{1N}_{l+1l}}{\partial \beta_{1N}} \frac{\partial \mathcal{H}}{\partial A^{1N}_{l+1l}} \Big]. \tag{3.16}$$

The momentum derivatives for the real and imaginary parts of β_{11} are obtained using the following expressions

$$\frac{\partial \mathcal{H}}{\partial \beta^r_{11}} = 2\Re\Big[\frac{\partial \mathcal{H}}{\partial \beta_{11}}\Big] \quad \text{and} \quad \frac{\partial \mathcal{H}}{\partial \beta^i_{11}} = -2\Im\Big[\frac{\partial \mathcal{H}}{\partial \beta_{11}}\Big], \tag{3.17}$$

where $\Re$ and $\Im$ are operators giving real and imaginary parts of the expression, respectively.

3.4 Summary

In this chapter, we explore the Bayesian framework adopted to infer the parameters of interest. We explain the data model and discuss the likelihood and prior distributions, ultimately leading to the joint posterior distribution of the signal covariance matrix and the signal in the spherical harmonic basis. The subsequent section delves into the application of the Hamiltonian Monte-Carlo (HMC) sampler for sampling this posterior distribution. Specifically, we focus on calculating the momentum derivatives for parameters such as a_{lm}, C_l, and the velocity parameters β_{1N}.

Moreover, this chapter addresses the non-ideal aspects of the data, incorporating these considerations into the expressions for momentum derivatives. We formulate the likelihood for the pixelated data, accounting for the beam effects, masking in the galactic region, and extra-galactic point sources. These factors are crucial in our analysis pipeline, especially given our focus on the *Planck*-2018 data. In the following chapter, we will delve into the implementation details of our pipeline on this data set and discuss the outcomes of our analysis.

Chapter 4

Analysis on *Planck*-2018 CMB temperature map

4.1 Introduction

This chapter delves into our analysis of the *Planck*-2018 temperature data [3]. Employing a Bayesian framework, we examine the joint posterior distribution of the signal covariance matrix and the signal through the *Hamiltonian Monte-Carlo* (HMC) technique, as detailed in the preceding chapter. As highlighted in Chapter 1, the *Planck* satellite represents a monumental achievement over the past decade, providing high-resolution and sensitivity measurements of the CMB fluctuation maps. This advance enabled the probe of cosmological parameters with unprecedented accuracy. The *Planck* satellite was equipped with a Low-Frequency Instrument (LFI) and a High-Frequency Instrument (HFI), comprising 73 detectors across nine frequency bands. The LFI covered 30, 44, and 70 GHz, while the HFI spanned 100, 143, 217, 353, 545, and 857 GHz. The scanning strategy allowed *Planck* to scan the entire sky twice annually, with beam resolutions ranging from 32.29 arcminutes at the 30 GHz channel to 4.22 arcminutes at the 857 GHz channel.

The CMB maps from these frequency channels were then synthesized into a combined map using several foreground-cleaning techniques. These techniques eliminate galactic and extragalactic foregrounds, which are typically frequency-dependent, unlike the CMB signal. *Planck* offers such foreground-cleaned maps through four component-separation methods: `NILC`, `SEVEM`, `Commander`, and `SMICA` [10]. Our primary analysis focuses on the

`SMICA` map, though we also present results from the other foreground-cleaned maps to affirm the robustness of our findings. The `SMICA` algorithm has been thoroughly described in Section 2.3, where we detailed the covariance matrix expression for the `SMICA` map in Eq. 2.18, utilizing the `SMICA` weights provided by *Planck*. In this chapter, Section 4.2 outlines the implementation details of our algorithm on the `SMICA` data. Section 4.4 presents the core results obtained from applying the algorithm to the *Planck*-2018 `SMICA` temperature maps, including the marginalized distributions and the maximum-a-posteriori estimates derived from those distributions. In Section 4.5, we extend our analysis to other foreground-cleaned maps, such as `NILC` and `SEVEM`, to further validate our results. The chapter concludes with a summary in Section 4.6.

4.2 Implementation Details

As discussed in Section 2.3, the `SMICA` pipeline provides us a hybrid map from the nine *Planck* frequency channels. The `SMICA` map is constructed in a specific manner [73] to minimize the contamination from foregrounds. Hence, as long as we are considering the cleaner regions of the CMB sky well away from the galactic plane and using multipoles higher than $l = 150$ for our analysis, we can use the approximation given in Eq. 2.15. Accordingly, we have performed our analysis on *Planck*-2018 `SMICA` temperature map for three different choices of masking and three different choices of the maximum CMB multipoles, which we have discussed elaborately later. These three masks have been shown in Figure 4.1a, 4.1b and 4.1c. To obtain the noise variance in each pixel to be used in Eq. 3.13, we use 200 FFP10 simulations of the `SMICA` noise [76]. At every pixel, we compute the variance of 200 FFP10 simulated noise maps[10] stored as `HEALPix` [97] maps with $N_{\text{side}} = 2048$. The noise variance map is provided in Figure 4.2. A more accurate computation of noise covariance matrix in pixel-space can be performed using a recipe developed in [98] and will be used in a future work. For the masked pixels that exclude regions with high galactic foreground contamination and known point source locations at high-latitudes, we assign infinite noise variance by making $1/\sigma^2 = 0$ in Eq. 3.13. This is the equivalent of having no information at those pixels. The anisotropy of the noise is encoded in the noise variance map. For the calculation of the mass matrix of a_{lm}'s [91], the noise power spectrum N_l is obtained from the difference of the two `SMICA` 2018 half-

---

[10] https://pla.esac.esa.int/

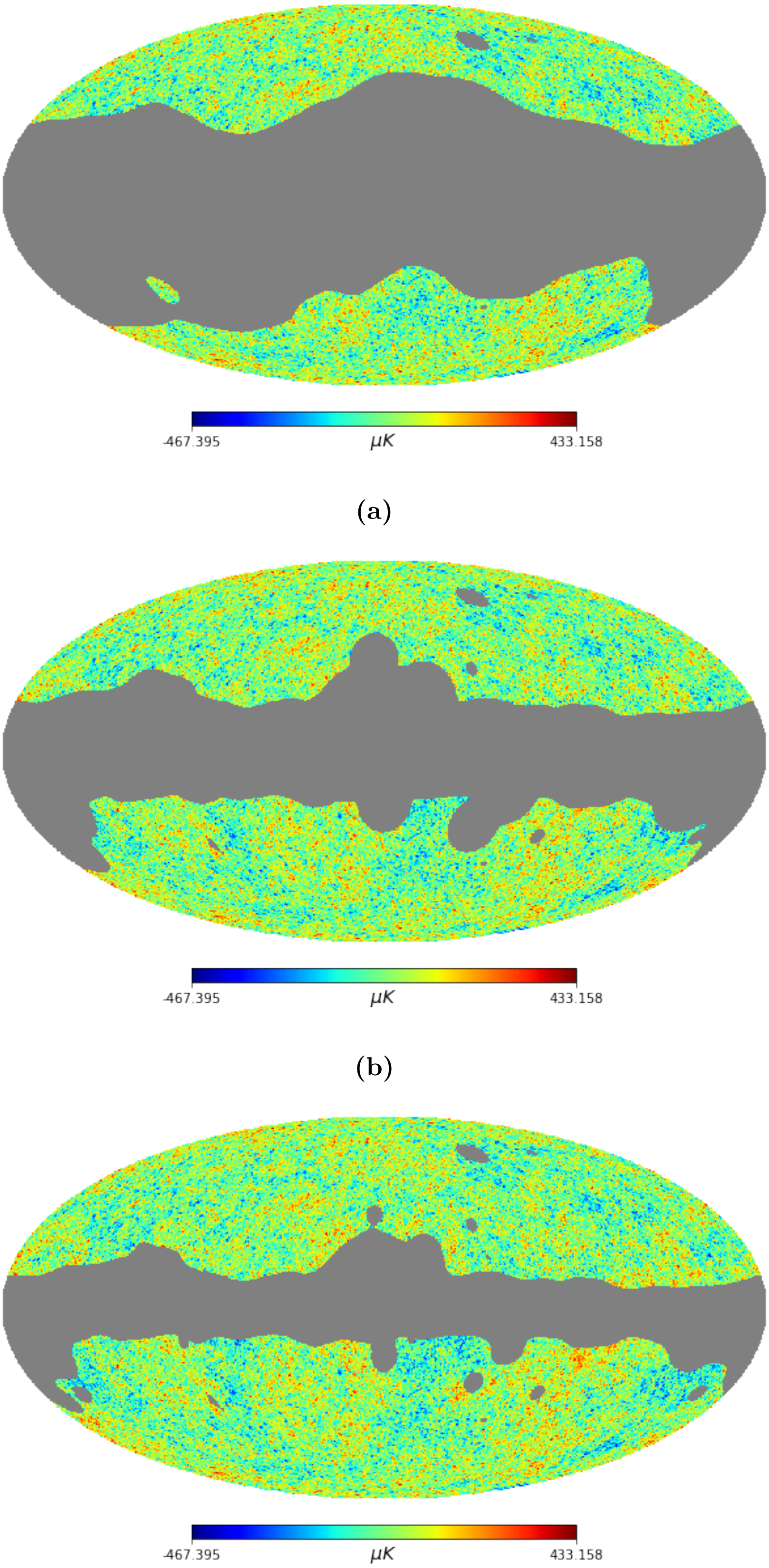
-467.395
μK
433.158
-467.395
μK
433.158
-467.395
μK
433.158

(a)

(b)

(c)

Figure 4.1: The grey regions in Figure 4.1a, 4.1b and 4.1c are the three different masks ($f_{\rm sky} = 40.1\%$, 59.1% and 72.2% respectively), that have been used in our analysis.

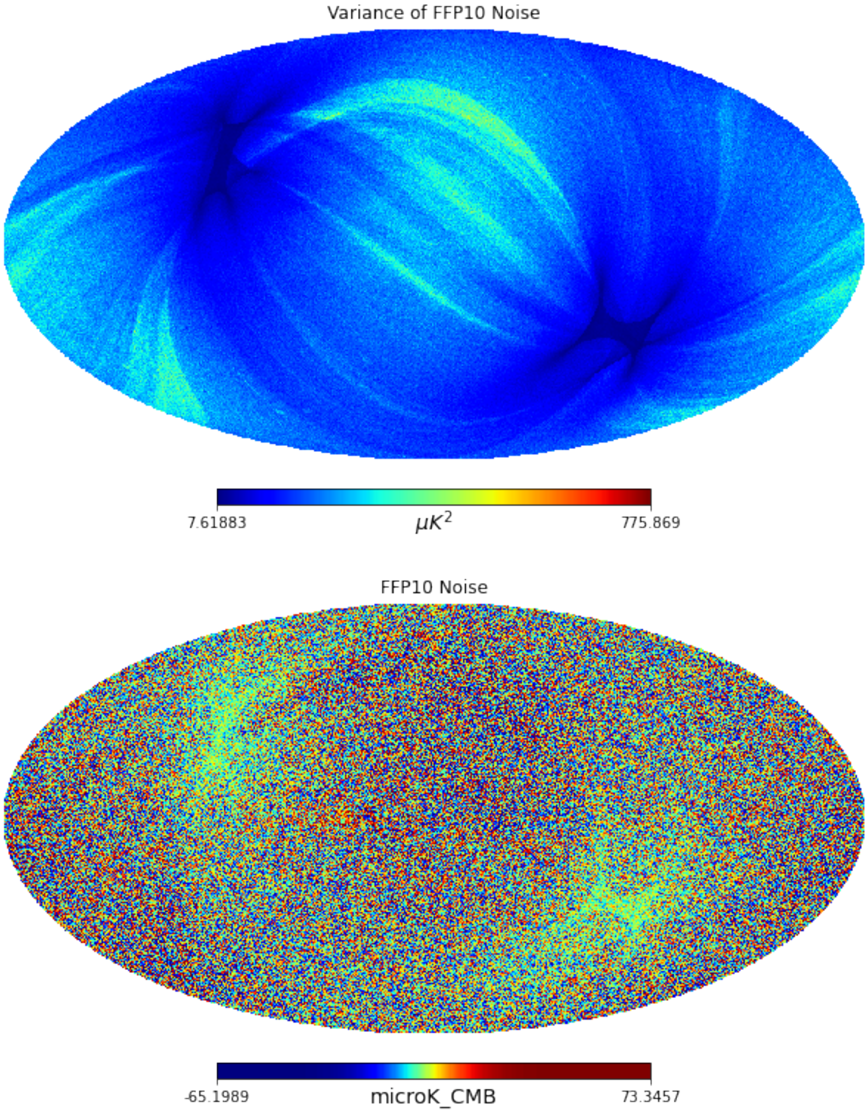

Figure 4.2: *Top panel:* The noise variance map, obtained from 200 FFP10 noise simulations, used in our analysis. *Bottom panel:* One of the FFP10 noise realizations.

mission maps[11], using the fact that noises of the two half-mission maps are uncorrelated. We have used a smooth N_l (with $l_{\text{width}} = 40$) in our analysis. In this joint inference approach, we also smooth the auxiliary C_l using a rectangular window function of bin width $l_{\text{width}} = 40$ and apply it in momentum derivative expressions of BipoSH, given in Eq. 3.14.

The whole analysis has been carried out at a resolution $N_{\text{side}} = 2048$, which grants us sufficiently high l_{range}. The modulation part of the Doppler boost signal is degenerate with

---

[11] `COM_CMB_IQU-smica_2048_R3.00_hm1.fits` and `COM_CMB_IQU-smica_2048_R3.00_hm2.fits` available at https://pla.esac.esa.int/

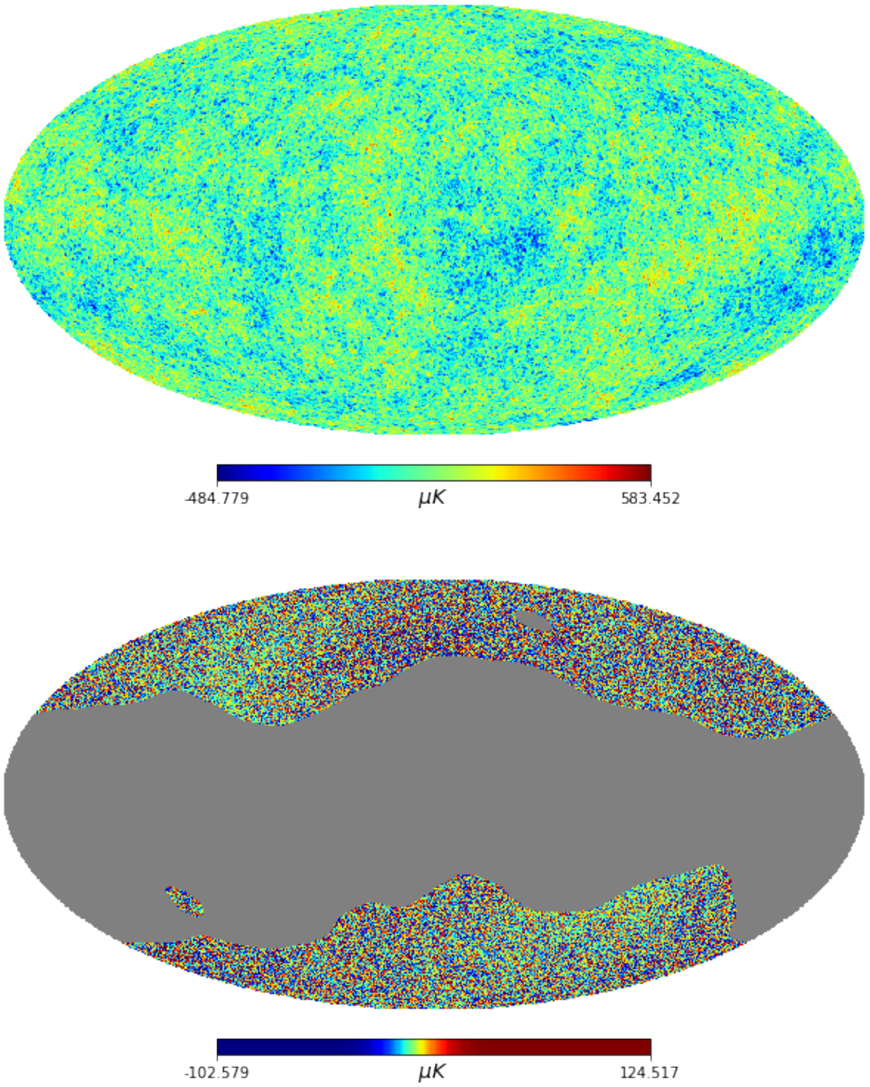

Figure 4.3: *Top panel:* One of the sample maps ($N_{\rm side} = 2048$) obtained from the a_{lm} samples with the primary set-up ($f_{\rm sky} = 40.1\%$, $l_{\rm max} = 1950$). *Bottom panel:* The difference between the SMICA map and the sample map at unmasked regions

the dipolar modulation signal of cosmic hemispherical asymmetry [11, 83–85, 89] at low l. Hence we restrict the multipoles used in our analysis to $l > l_{\rm min} = 800$ to circumvent possible contamination in the estimation of β. We carry out our analysis using two different $l_{\rm range}$ from $l_{\rm min} = 800$, with $l_{\rm max} = 1500$ and 1950[12]. Since the Doppler boost signal is scale-independent and the variance of the β_{1N} is inversely proportional to the number of modes considered [11, 44], it is crucial to perform the analysis up to high values of the multipoles l. The analysis using the mask $f_{\rm sky} = 40.1\%$, with $l_{\rm max} = 1950$ is our primary set-up in this work as it is the most conservative choice of a mask to reduce the contamination from galactic foregrounds and in obtaining a more reliable inference of the Doppler boost signal. In the next subsection, we present the detailed results obtained with this primary setup. We also provide the inferred values from the other variations of the setup as well.

---

[12] We have also obtained the result for $l_{\rm max} = 1700$. It agrees well with the other $l_{\rm max}$ choices.

4.3 HMC samples of CMB maps

We have obtained 5×10^4 samples of the model parameters using HMC sampling method discussed in Section 3. We discard the first 4000 samples as burn-in. In the top panel of Figure 4.3, we show one of the samples of a_{lm}. In the bottom panel of Figure 4.3, we show the difference between the sample map and the input `SMICA` map over the unmasked regions. From this figure, it is very prominent that the sample map and the input map agrees well, in the regions with less noise variance (see top panel of Figure 4.2).

4.4 Inference of the Covaraince Matrix

4.4.1 The Diagonal Part

In the rest of this section we discuss the distribution of the CMB covariance matrix parameters obtained using the HMC technique. By allowing a_{lm} to vary subject to the assumptions of the data likelihood, we assimilate all the information present in the data map. However, it is the samples of the covariance matrix parameters, C_l and β_{1N}, that confront the Doppler boost model. In the top panel of Figure 4.4, we present the distributions of C_l samples for some specific values of l. For comparison, we also provide the realisation C_l values of `SMICA` map (accounting for the N_l and the beam) and the ΛCDM best-fit theory C_l's provided by *Planck* [99], at those l's. The fitted curves in these figures are the analytic form of marginalised posterior distributions of C_l's as given in [100, 101]

$$\mathcal{P}(C_l|\boldsymbol{d}) \approx \frac{1}{N_{\text{sample}}} \sum_i \mathcal{P}(C_l|\sigma_l^i), \tag{4.1}$$

where σ_l^i is the realisation power spectra of the a_{lm} samples and the index i runs overs the N_{sample} number of samples. The conditional distribution of C_l given σ_l^i, has the following

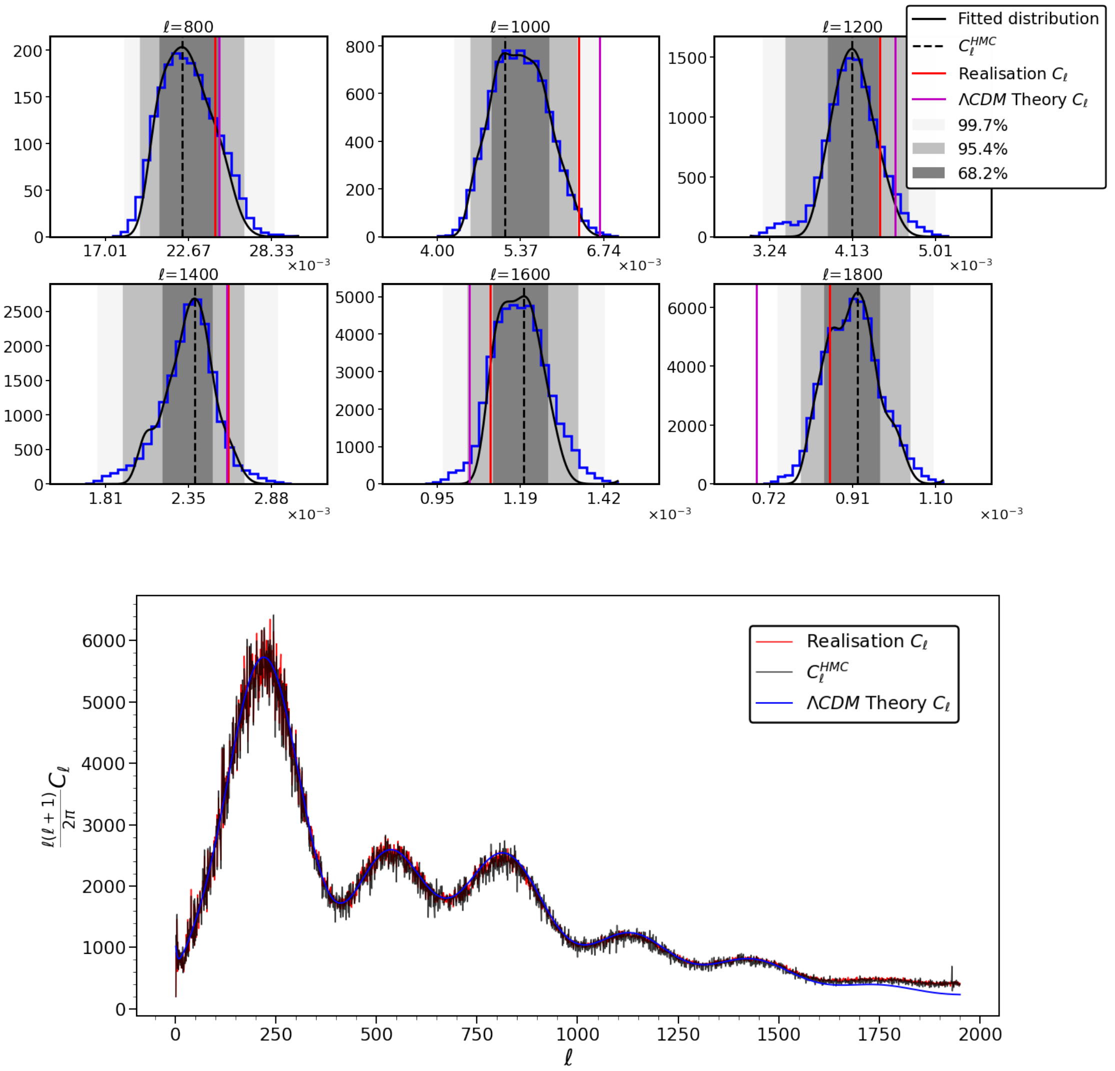

Figure 4.4: *Top panel:* The distributions of C_l's for six different l values. Histograms are obtained using the samples of C_l. The solid black curve is the analytic distribution curve of that specific C_l. The black dashed line shows the peak values. The solid red line represents the value of C_l obtained from `SMICA` map. The magenta line shows the best fit ΛCDM theory C_l given by *Planck*. *Bottom panel:* The Maximum-a-posteriori estimate of C_l distribution inferred in this analysis (black curve) along with the realisation C_l (red curve) obtained from the `SMICA` map. The blue curve represents the best fit ΛCDM theory C_l given by *Planck*. We have an evidence in the power spectrum of a SMICA residual of an isotropic unresolved extra-galactic point source background.

form [100, 101]

$$\mathcal{P}(C_l|\sigma_l^i) \propto C_l \left(\frac{\sigma_l^i}{C_l}\right)^{\left(\frac{2l+1}{2}-1\right)} \exp\left[-\frac{2l+1}{2}\frac{\sigma_l^i}{C_l}\right]. \tag{4.2}$$

We use this analytical form to fit the corresponding distributions[13]. We present the peaks of the distributions as the estimated value of C_l's in our analysis. In the bottom panel of Figure 4.4, we plot the inferred power spectrum along with the realisation C_l of `SMICA` map and the ΛCDM best-fit theory C_l's.

4.4.2 The off-diagonal part

Next, we present the inference of the off-diagonal terms in the covariance matrix. As the expression of the off-diagonal terms Eq. 2.21 suggests, this eventually boils down to the inference of the Doppler boost signal in our case. We have provided the summary of our results with the three choices of masking (as given in Figure 4.1) using multipoles up to $l_{\text{max}} = 1950$, in Table 4.1. In this table, we present the maximum posterior points as the inferred values of the β_{10}, β^r_{11} and β^i_{11} parameters in our analysis, along with the error bars. We also provide the velocity amplitudes β and the direction of the velocity in Galactic coordinates (ℓ, b), obtained from the maximum posterior points of their distributions, along with their corresponding error bars. The reported β is obtained from the corresponding maximum posterior points of the β_{10}, β^r_{11} and β^i_{11} distributions. We report the signal to noise ratio (SNR) of the measurement of the Doppler boost signal for different choices of galactic mask in Table 4.1. A 5.23σ detection of the non-zero value of Doppler boost is achieved from the case with $f_{\text{sky}} = 72.2\%$. For the other choices of masks, $f_{\text{sky}} = 59.1\%$ and $f_{\text{sky}} = 40.1\%$, we have made a 4.97σ and 4.54σ detection of the Doppler boost signal respectively.

For our primary setup ($f_{\text{sky}} = 40.1\%$, $l_{\text{max}} = 1950$) we present the joint posterior distributions of β_{10}, β^r_{11} and β^i_{11} samples in Figure 4.5. We also compare the estimated values of Doppler boost parameters β_{1N} in this analysis, with the canonical values known from the CMB dipole measurements $\beta = 1.23 \times 10^{-3}$ [16, 40–42]. The 2D joint distributions of the β_{1N} parameters show that there is no significant correlation among them. The distribution of the velocity amplitude β and the joint distribution of the direction coordinates (ℓ, b) are given in Figure 4.6 and Figure 4.7, respectively. The samples of the real-space variables β, ℓ and b have been obtained from the β_{10}, β^r_{11} and β^i_{11} samples using the transformation relation Eq. 2.9. Galactic latitude b is related to the `HEALPix`

---

[13] An extremely large number of independent σ_l samples is required in Eq. 4.1 to get the accurate distribution at high l. So instead, we take $N_{\text{sample}} = 10$ and treat those ten σ^i_l as free parameters in the analytical form of the distribution. We use the subroutine `scipy.optimise.curve_fit` [102] to optimize the values of these parameters to get the best-fit curve for the posterior distribution.

Table 4.1: Summary of results for different choices of mask, with $l_{\text{min}} = 800$ and $l_{\text{max}} = 1950$

$f_{\text{sky}} = 40.1\%$, SNR= 4.54

Parameter	$\beta_{10} \times 10^3$	$\beta_{11}^r \times 10^3$	$\beta_{11}^i \times 10^3$	$\beta \times 10^3$	ℓ	b
Inferred Value	1.840	0.014	-0.620	0.996	268.5°	61.8°
Standard Deviation	0.436	0.298	0.378	0.219	49.8°	12.3°

$f_{\text{sky}} = 59.1\%$, SNR= 4.97

Parameter	$\beta_{10} \times 10^3$	$\beta_{11}^r \times 10^3$	$\beta_{11}^i \times 10^3$	$\beta \times 10^3$	ℓ	b
Inferred Value	2.058	0.031	-0.248	1.020	264.5°	75.2°
Standard Deviation	0.427	0.327	0.366	0.205	88.2°	9.7°

$f_{\text{sky}} = 72.2\%$, SNR=5.23

Parameter	$\beta_{10} \times 10^3$	$\beta_{11}^r \times 10^3$	$\beta_{11}^i \times 10^3$	$\beta \times 10^3$	ℓ	b
Inferred Value	2.104	-0.002	-0.509	1.087	270.4°	68.2°
Standard Deviation	0.428	0.326	0.340	0.208	57.1°	10.3°

polar angle θ_β as $b = 90 - \theta_\beta$, whereas Galactic longitude ℓ is the same as the `HEALPix` azimuthal angle ϕ_β. We have also presented the inferred directions for three different masks with $l_{\text{max}} = 1950$ and $l_{\text{max}} = 1500$ in Figure 4.7.

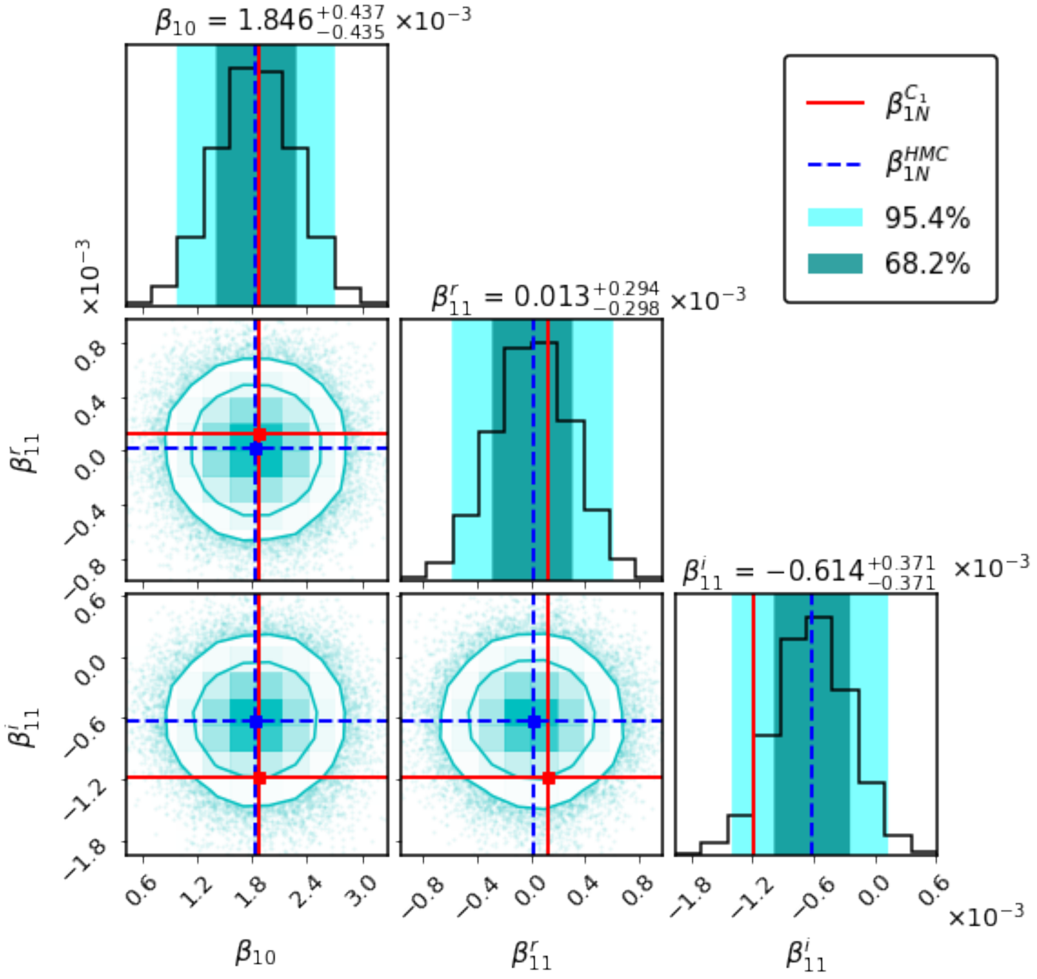

Figure 4.5: The figure presents the 1D distributions and 2D joint distributions of β_{10}, β^r_{11} and β^i_{11} samples. These samples are obtained from the analysis of the `SMICA` 2018 temperature map, with $f_{sky} = 40.1\%$ mask, using multipoles up to $l_{max} = 1950$. The contours in the joint distribution show the levels for 68% and 90% of the sample points, respectively. The blue dashed line shows the peak values of the distribution and the red solid line represents the canonical value of our local motion from CMB dipole.

The amplitude of the signal is consistent with the value measured from the CMB dipole, for all the three choices of mask and the values of $l_{\max}$ considered in this analysis. The direction of the signal is most consistent with the choice $f_{\rm sky} = 40.1\%$ (as shown in Table 4.1 and Figure 4.7), as it is the most conservative choice to avoid galactic contamination. We do not explore below this sky fraction as that would mask the Doppler boost signal significantly causing loss of information in inferred amplitude. The choice of $l_{\max}$ is also crucial in our analysis. As we can see from the C_l inference in Figure 4.4, there is a mismatch between the best-fit theory C_l given by *Planck* and the realisation

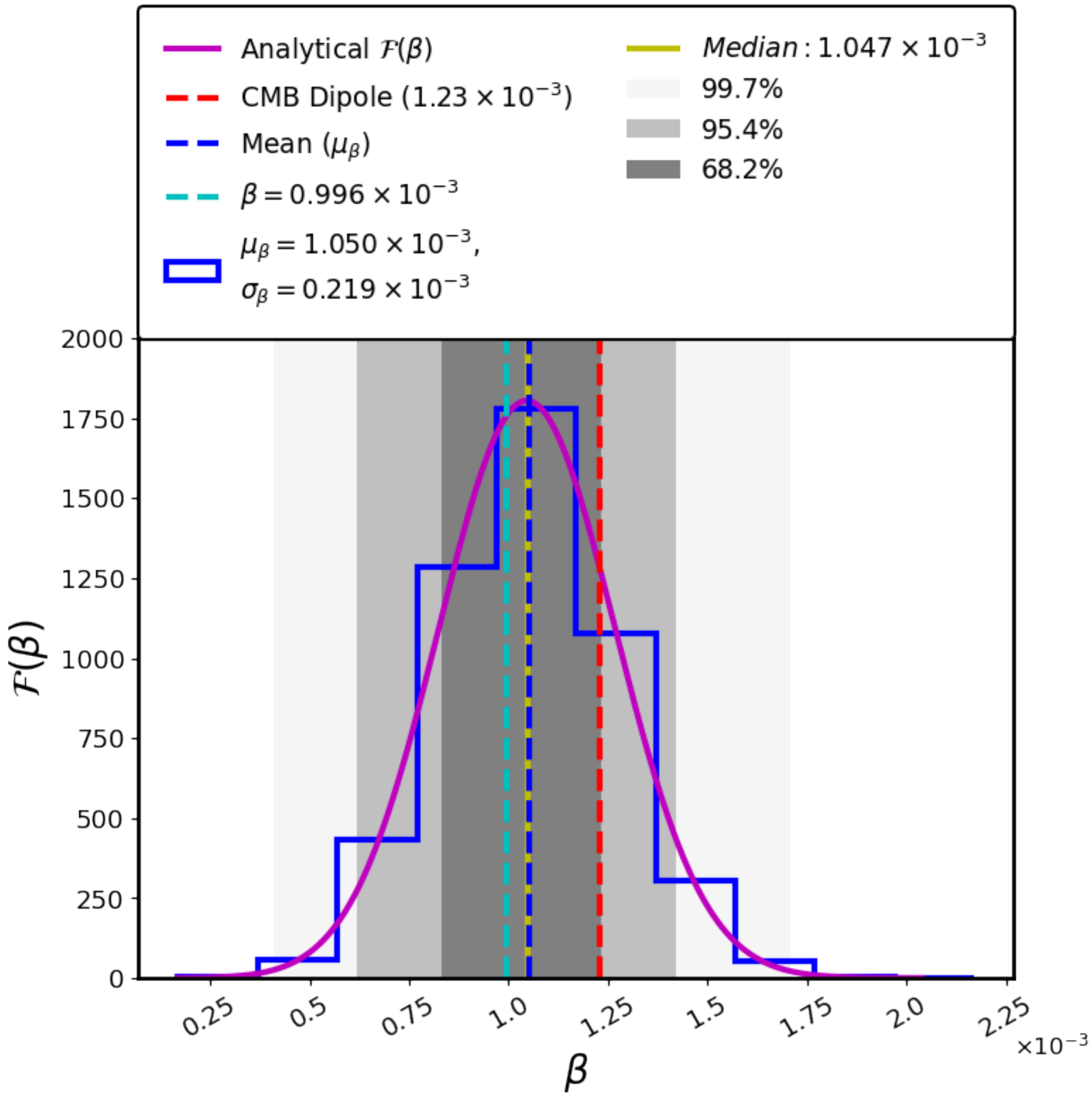

Figure 4.6: the distribution of β. The samples of β, θ_β and ϕ_β has been obtained from the β_{10}, β_{11}^r and β_{11}^i samples using Eq. 2.9.

C_l of `SMICA` at $l \geq 1500$, likely due to the unresolved point sources contributions at those scales [99,103,104]. For an isotropic distribution of point sources, we do not expect a statistically significant departure of the inferred direction of Doppler boost from the fiducial value inferred from CMB dipole [16,39–42]. Furthermore the inferred C_l from our analysis is consistent with the `SMICA` realisation C_l as expected. So, we consider a Galactic mask with a low available sky fraction and include CMB multipoles up to $l_{\max} = 1950$ to reduce the contamination from anisotropic Galactic foregrounds in the estimation of Doppler boost signal, and also maximize the signal to noise ratio (SNR) of the detection of the signal, even though it costs us a slight shift in the inference of its direction (see

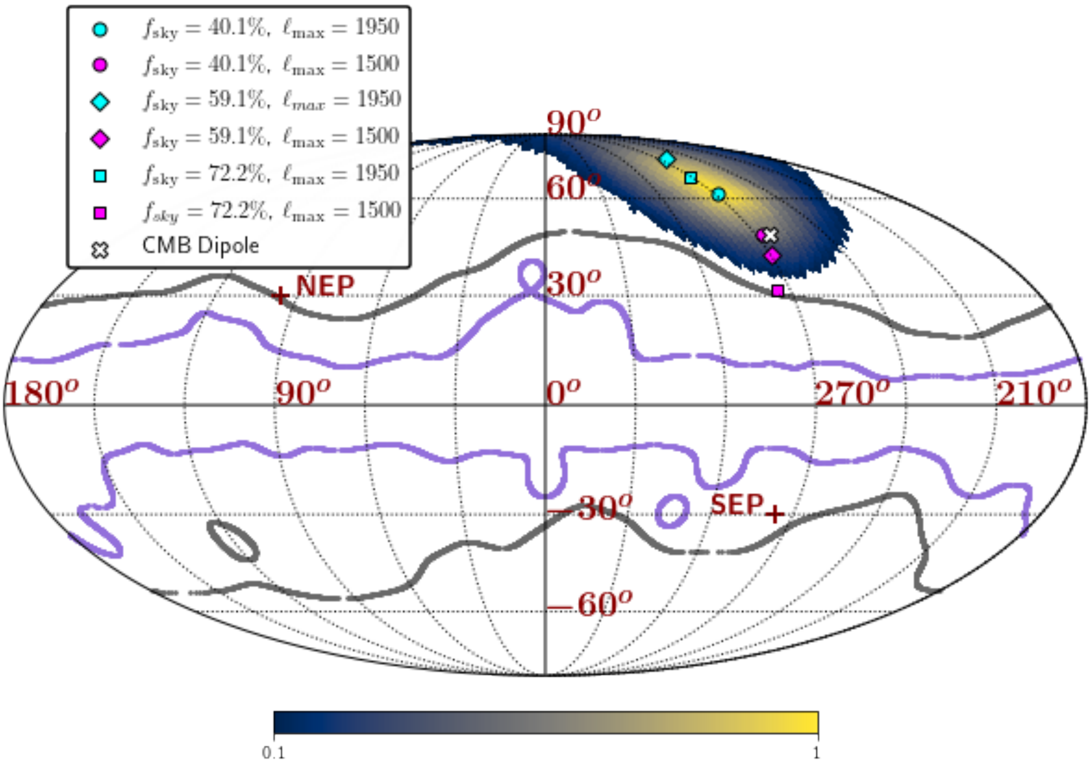
$f_{\rm sky} = 40.1\%,\ \ell_{\rm max} = 1950$
$f_{\rm sky} = 40.1\%,\ \ell_{\rm max} = 1500$
$f_{\rm sky} = 59.1\%,\ \ell_{max} = 1950$
$f_{\rm sky} = 59.1\%,\ \ell_{\rm max} = 1500$
$f_{\rm sky} = 72.2\%,\ \ell_{\rm max} = 1950$
$f_{sky} = 72.2\%,\ \ell_{\rm max} = 1500$
CMB Dipole
90°
60°
30°
NEP
180°
90°
0°
270°
210°
−30°
SEP
−60°
0.1
1

Figure 4.7: The joint distribution of θ_β and ϕ_β with $f_{\rm sky} = 40.1\%$ mask, using multipoles up to $l_{\rm max} = 1950$. The samples of β, θ_β and ϕ_β has been obtained from the β_{10}, β^r_{11} and β^i_{11} samples using Eq. 2.9. In Figure 4.6, the dashed blue line is the mean of this histogram, whereas the dashed cyan line depicts the β value corresponding to the maximum posterior points of β_{10}, β^r_{11} and β^i_{11} parameters. The purple curve represents the analytical form of this distribution (as derived in [11]). The dashed red line presents the known dipole amplitude corresponding to the Solar System velocity 1.23×10^{-3}. In Figure 4.7, the θ_β and ϕ_β samples are binned in a `HEALPix` grid of $N_{\rm side} = 32$, normalized by its peak value and smoothed by a Gaussian kernel. The cyan circle represents the maximum posterior point of the distribution with our primary set-up. The white cross represents the known dipole direction. In this figure, we also depict the inferred direction for the other analysis setups: $f_{\rm sky} = 59.1\%$, $l_{\rm max} = 1950$ (cyan diamond); $f_{\rm sky} = 72.2\%$, $l_{\rm max} = 1950$ (cyan square); $f_{\rm sky} = 40.1\%$, $l_{\rm max} = 1500$ (magenta circle); $f_{\rm sky} = 59.1\%$, $l_{\rm max} = 1500$ (magenta diamond) and $f_{\rm sky} = 72.2\%$, $l_{\rm max} = 1500$ (magenta square). The grey and purple lines show the borders of $f_{\rm sky} = 40.1\%$ and $f_{\rm sky} = 72.2\%$ masks respectively.

Figure 4.7) from the fiducial value inferred from CMB dipole [16, 40–42]. In future work, we will do a joint estimation of the point source and foreground contamination, along with the CMB and the Doppler boost signal to explore the reason for this minor shift in the Doppler boost direction.

4.5 Robustness of Results on Different Foreground Cleaned Maps

In this section, we replicate the analysis on the `NILC` and `SEVEM` maps[1] with the mask $f_{\rm sky} = 40.1\%$, using multipoles from $l_{\rm min} = 800$ up to $l_{\rm max} = 1950$. The noise variance maps needed for the analysis have been obtained by computing variances at every pixel of FFP10 noise simulations[2] for each kind.

To express the spherical harmonic coefficients (a_{lm}'s) of a Doppler-boosted sky for component-separated CMB maps and to compute the effective boost factor, it is necessary to use specific weights (for `NILC`) or coefficients (for `SEVEM`). These are then integrated according to the formula applicable to each component separation map. While the necessary weights and codes for performing these operations on the `SMICA` map are publicly accessible[3], similar resources for `NILC` and `SEVEM` is not available. As a result, our analysis of these maps does not employ the same level of rigor in calculating the effective boost factor as done for the `SMICA` map. Instead, we have adopted a constant effective boost factor $b_{\rm eff} = 2.38$, matching the average `SMICA` boost factor for the given mask and $l_{\rm range}$

For a comparative analysis with the `SMICA` results, our findings are summarized in Table 4.2. Moreover, we present the distributions of velocity amplitude and inferred directions for `NILC` and `SEVEM`, alongside those from `SMICA`, in the top and bottom panels of Figure 4.8, respectively.

4.6 Summary

In this chapter, we have presented the findings from our analysis of the *Planck*-2018 temperature data within a Bayesian framework. Employing Hamiltonian Monte Carlo (HMC) sampling, as detailed in the preceding chapter, we have navigated the joint posterior distribution of the entire covariance matrix and the signal itself. The diagonal elements of the covariance matrix represent the power spectrum C_l's, and the inference of its off-diagonal elements primarily involves determining the observation frame's velocity, denoted as $\boldsymbol{\beta}$. The spherical harmonic components of the dipole field, which arise due to motion, $D(\hat{n}) = \boldsymbol{\beta} \cdot \hat{n}$, are parameterized by β_{10}, β_{11}^r, and β_{11}^i. These are the key parameters of interest. Conversion to the amplitude and direction of the velocity

---

[1] `COM_CMB_IQU-nilc_2048_R3.00_full.fits` and `COM_CMB_IQU-sevem_2048_R3.01_full.fits` available at https://pla.esac.esa.int/

[2] https://pla.esac.esa.int/

[3] `COM_Code_SMICA-weights-propagation_R3.00.tar.gz` available in https://wiki.cosmos.esa.int/planck-legacy-archive/index.php/SMICA_propagation_code

Table 4.2: Summary of results for different component separation CMB maps, with mask $f_{\text{sky}} = 40.1\%$, using multipoles from $l_{\text{min}} = 800$ upto $l_{\text{max}} = 1950$

`SMICA`						
Parameter	$\beta_{10} \times 10^3$	$\beta_{11}^r \times 10^3$	$\beta_{11}^i \times 10^3$	$\beta \times 10^3$	ℓ	b
Inferred Value	1.840	0.014	-0.620	0.996	268.5°	61.8°
Standard Deviation	0.436	0.298	0.378	0.219	49.8°	12.3°

`NILC`						
Parameter	$\beta_{10} \times 10^3$	$\beta_{11}^r \times 10^3$	$\beta_{11}^i \times 10^3$	$\beta \times 10^3$	ℓ	b
Inferred Value	1.522	-0.118	-0.581	0.849	280.5°	57.2°
Standard Deviation	0.432	0.305	0.372	0.217	61.8°	13.9°

`SEVEM`						
Parameter	$\beta_{10} \times 10^3$	$\beta_{11}^r \times 10^3$	$\beta_{11}^i \times 10^3$	$\beta \times 10^3$	ℓ	b
Inferred Value	1.848	-0.016	-0.527	0.974	271.8°	65.5°
Standard Deviation	0.429	0.304	0.359	0.209	62.3°	11.7°

is achieved using Eq. 2.9. We provide the posterior distributions of the C_l's for different multipoles l and the maximum-a-posteriori estimate of C_l from the distribution in Figure 4.4. This analysis emphasizes the importance of jointly inferring the diagonal

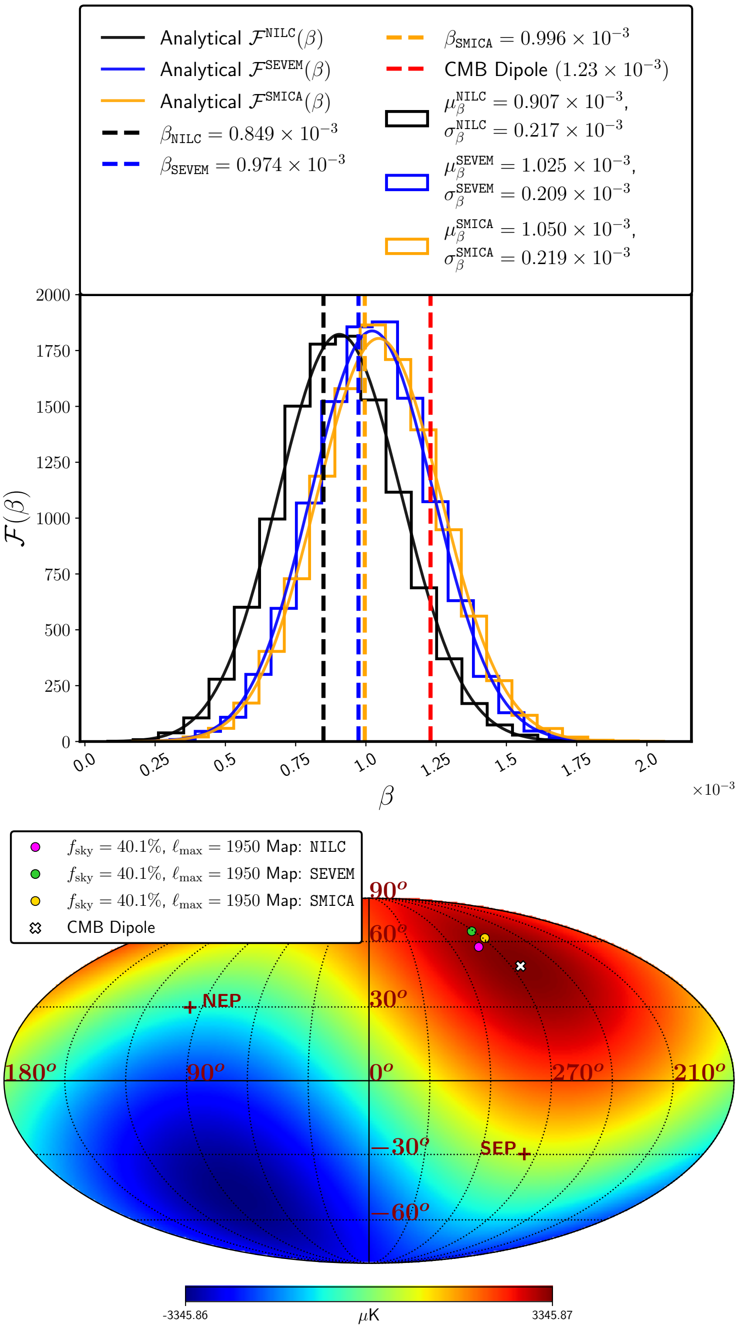

Figure 4.8: *Top panel:* The distributions of the velocity amplitude for `NILC` (black), `SEVEM` (blue) and `SMICA` (orange), with the mask $f_{\rm sky} = 40.1\%$ using multipoles from $l_{\rm min} = 800$ up to $l_{\rm max} = 1950$. The inferred values from these three maps have been indicated by the dashed line, with the same colour choices. The red dashed line represents the value inferred from CMB dipole. *Bottom panel:* The inferred directions for `NILC` (magenta dot), `SEVEM` (green dot) and `SMICA` (yellow dot), with the mask $f_{\rm sky} = 40.1\%$ using multipoles from $l_{\rm min} = 800$ up to $l_{\rm max} = 1950$. The map shown in this figure corresponds to the observed CMB dipole, with the direction indicated by the white cross.

and off-diagonal terms, as the off-diagonal terms also relate to the power spectrum C_l, a relationship previously discussed in Chapter 2.

Next, we discuss the inference results concerning the local motion velocity derived from the *Planck*-2018 `SMICA` temperature map, which constitute the primary findings of our study. The analysis includes the marginalized and 2D joint distributions of the velocity parameters in spherical harmonic space, β_{10}, β^r_{11}, and β^i_{11}, as presented in Figure 4.5. As anticipated, our results indicate no significant correlation among these parameters. We summarise the main results for the multipole range $l_{\rm range} = 800 - 1950$, employing three sets of sky fractions $f_{\rm sky} = 40.1\%, 59.1\%$, and 72.2%, in Table 4.1. The distributions of amplitude and direction of the velocity, computed using Eq. 2.9, are depicted in Figure 4.6. These findings align closely with the canonical values obtained from the CMB dipole, remaining within 1σ margins for both amplitude and direction distributions. For the specified sky fractions, the significance of detection is reported at 4.54σ, 4.97σ, and 5.23σ, respectively. Additionally, this chapter compares the results with analyses conducted on other foreground-cleaned maps, such as `NILC` and `SEVEM` in Section 4.5, demonstrating consistency with the primary `SMICA` findings. We calculate the Bayes factor in the subsequent chapter to evaluate further the likelihood of the canonical value expected from the CMB Dipole.

Chapter 5

Model Comparison with Bayes factor

5.1 Introduction

Bayesian statistics provides a principled way to compare two different models. Using the conditional probabilities involved in the Bayes theorem, one can obtain the expression for the ratio of the probability of two models conditioned on a given data set. This ratio is called the Bayes factor. It is a prime tool for the comparison of two models [105–107] under consideration. The expression of Bayes factor for two models M_1 and M_2 is given by

$$B_{M_1-M_2} = \frac{\mathcal{P}(M_1|d)}{\mathcal{P}(M_2|d)} = \frac{\mathcal{P}(M_1)}{\mathcal{P}(M_2)}\frac{\mathcal{E}(d|M_1)}{\mathcal{E}(d|M_2)}. \tag{5.1}$$

In the absence of any a priori discriminating information between two models, we choose the prior probability $\mathcal{P}(M)$ for the two models M_1 and M_2 to be equal. Hence, the Bayes factor becomes just the ratio of the Bayesian evidence $\mathcal{E}(d|M)$ for those two models. Section 5.2 details the computation of the Bayes factor for the canonical value derived from the CMB dipole. Subsequently, Section 5.3 focuses on calculating the Bayes factor for a velocity value inferred from the dipole observable in quasar data [49]. This structured analysis aims to quantitatively assess the comparative evidence each model provides for the observed data, facilitating a more informed evaluation of the models' validity in explaining the Doppler boost phenomena in CMB fluctuations.

5.2 Bayes Factor for Known CMB Dipole Value

In our work, the two models that we compare are as follows. The M_2 in the denominator, is the Doppler boost model. The M_1 in the numerator, is the hypothesis that the CMB sky is Doppler boosted with the velocity amplitude, $\beta = 1.23 \times 10^{-3}$ (the inferred velocity amplitude from CMB dipole [16, 40–42]). For the sake of convenience, we reparametrize our variables to equal variance parameters [11],

$$w_z = \beta_{10}, w_x = -\sqrt{2}\beta_{11}^r, w_y = \sqrt{2}\beta_{11}^i. \tag{5.2}$$

In this new three dimensional parameter space, the norm r can be defined as

$$r \equiv \sqrt{w_z^2 + w_x^2 + w_y^2} = \sqrt{\beta_{10}^2 + 2{\beta_{11}^r}^2 + 2{\beta_{11}^i}^2} = \sqrt{\frac{4\pi}{3}}\beta. \tag{5.3}$$

So the model M_1 is a nested model within M_2, with the value of the parameter $r = r|_{\beta=1.23\times10^{-3}}$. Hence, the Bayes factor can be obtained using the Savage-Dickey density ratio (SDDR) [87, 108],

$$B_{\rm SDDR} = \left.\frac{\mathcal{P}_{C_l,\theta,\phi}(r|d, DB)}{\Pi(r|DB)}\right|_{\beta=1.23\times10^{-3}}, \tag{5.4}$$

where, $\mathcal{P}_{C_l,\theta,\phi}(r|d, DB)$ is the posterior distribution of the norm (r), marginalised over power spectrum (C_l) and the direction (θ, ϕ). Π is the prior distribution of the norm. We choose Π to be uniform within a sphere of radius $R = r|_{\beta=2.73\times10^{-3}}$, centered at $(w_x, w_y, w_z) = (0, 0, 0)$, and zero outside. The marginalized prior density of the norm is

$$\Pi(r|DB) = \frac{3r^2}{R^3} \quad \text{for } r \leq R. \tag{5.5}$$

With this setup, we find the Bayes factor in favour of M_1, to be

$$B_{\rm SDDR} \approx 7.43 \text{ for } f_{sky} = 40.1\%. \tag{5.6}$$

According to the Jeffreys' scale [105], this indicates that the data substantially favors the value of β from known CMB dipole, as it stays within 1.1σ from the inferred signal strength in our analysis. For the other two masks ($f_{\rm sky} = 59.1\%$ and 72.2%), the values of the Bayes factor in favor of the canonical value of β, are 8.14 and 8.72, respectively. The Bayes factors with $l_{\text{max}} = 1500$ are 5.22, 5.57 and 4.99 for $f_{\text{sky}} = 40.1\%$, 59.1% and 72.2% respectively.

5.3 Bayes Factor for Known Quasar Dipole Value

We also calculate the Bayes factor for the β value inferred using the amplitude of the dipole signal 0.01554 estimated in [49], which makes use of the CatWISE2020 quasar catalog [109] prepared from the WISE [110] and NEOWISE data set [111]. By using the median value of 1.17 for the power-law spectra index (parameter α in Eq. 1 in [49]), we get a value of $\beta = 2.73 \times 10^{-3}$ from the observed dipole amplitude 0.01554 [14]. Now the M_1 in Eq. 5.1 is the hypothesis that the CMB sky is Doppler boosted with an velocity amplitude $\beta = 2.73 \times 10^{-3}$ [49]. We do not have enough samples at this value of β to compute the value of posterior from the histogram. Hence, we use the analytical form of the posterior distribution to obtain the value at the desired point. Since w_x, w_y and w_z are all Gaussian random variables, we can derive the analytic form of the posterior distribution of norm (r), marginalized over (θ, ϕ) to be [11]

$$\mathcal{P}(r) = \frac{r}{\sigma^2}\sqrt{\frac{r}{r_*}}\exp\left[-\frac{r^2 + r_*^2}{2\sigma^2}\right] I_{1/2}\left(\frac{r r_*}{\sigma^2}\right) \qquad \text{for } r \leq R, \tag{5.7}$$

where r_* is the norm of (w_{x*}, w_{y*}, w_{z*}), the maximum likelihood point in the $w_x w_y w_z$-space and σ is the standard deviation of each of these variables. $I_{1/2}$ is the modified Bessel function of first kind with order 1/2. We estimate the values of r_* and σ from the (w_x, w_y, w_z) samples. Using the value of posterior and prior at $\beta = 2.73 \times 10^{-3}$, we find the Bayes factor in favour of this model to be

$$B_{\text{SDDR}} \approx 1.24 \times 10^{-11}. \tag{5.8}$$

This indicates a strong disagreement (according to the Jeffreys' scale [105]) with the value of local motion $\beta = 2.73 \times 10^{-3}$. The mismatch between the amplitude of the velocity inferred from CMB and from quasars differs by about 8σ. For the other two choices of masks, ($f_{\text{sky}} = 59.1\%$ and 72.2%), the values of the Bayes factor in favour of the quasar value are 3.35×10^{-11} and 6.58×10^{-11}, respectively, indicating strong disagreement with the value inferred in this work. The Bayes factors with $l_{\text{max}} = 1500$ are 1.47×10^{-5}, 1.65×10^{-4} and 2.26×10^{-4} for $f_{\text{sky}} = 40.1\%$, 59.1% and 72.2% respectively. So, for both the extreme choices of l_{max} considered in this analysis, a high value of local motion ($\beta \approx 2.73 \times 10^{-3}$) is strongly disfavoured[15].

---

[14] For a mean value of the power-law spectral index $\alpha = 1.26$, one can get a value of $\beta = 2.66 \times 10^{-3}$ [112].

5.4 Summary

This chapter discusses the estimation of the Bayes factor for various values of the local motion velocity. The Bayes factor is a statistical metric used to quantify how much more likely one model is compared to another, given the observed data. When the analysis involves a specific value for the velocity, one model effectively becomes a nested model within a more general model where the velocity is a free parameter. We employed the Savage-Dickey density Ratio (SDDR) to calculate the Bayes factor in such cases.

Initially, we calculated the Bayes factor for the canonical value of β derived from the CMB dipole, which was found to be 1.23×10^{-3}. This yielded a Bayes factor in the range of 7.43 to 8.72. According to Jeffrey's scale, these results strongly indicate that the canonical value of β is favored by the Doppler boost signal observed in the small angular scale fluctuations of the CMB. For comparative purposes, we also calculated the Bayes factor for a value of β derived from the quasar dipole, which was found to be 1.24×10^{-11}. This significantly lower value indicates a strong disfavor towards the quasar dipole-derived β in the context of the Doppler-boost signal in CMB.

By evaluating the Bayes factor for the velocity value from the CMB dipole, we effectively constrain the likelihood of any intrinsic dipole component that might have been present in the observed CMB dipole at the milliKelvin (mK) scale. This approach not only underscores the utility of the Bayes factor in model comparison but also enhances our understanding of the underlying mechanisms contributing to the observed cosmological dipole in CMB.

---

[15] We also calculate the Bayes factor for $\beta = 2.66 \times 10^{-3}$ which corresponds to $\alpha_{\text{mean}} = 1.26$ of the distribution given in [49]. These values are 1.17×10^{-10}, 2.90×10^{-10} and 5.96×10^{-10} with $l_{\text{max}} = 1950$ for $f_{\text{sky}} = 40.1\%$, 59.1% and 72.2% respectively.

Part III

Clusters: Small-Scale CMB Lenses

Chapter 6

CMB lensing by galaxy clusters

6.1 Introduction

Galaxy clusters are the largest gravitationally bound structures in the Universe. Their abundance as a function of redshift and mass is a direct probe of the growth of structures, and thus provides constraints on the matter density $\Omega_{\rm m}$, on the amplitude of matter fluctuations σ_8, as well as on the dark energy equation of state and the sum of neutrino masses [113–123].

To constrain the cluster mass, most surveys rely on either the richness [124–128], the X-Ray emission [113,129,130], or the Sunyaev-Zel'dovich (SZ) effect [116,119,131]. These observables need to be calibrated against the total cluster mass (including both baryonic and dark matter). This scaling relation between the observable and the cluster mass is currently the dominant source of systematic error [132–134]. With future CMB surveys, which are expected to detect of order 10^5 galaxy clusters [26,28,123,135], the systematic uncertainties will dominate the error budget, and as such accurate mass calibration is even more necessary.

The effect of gravitational lensing provides a direct observable of the total mass, free from assumptions on the dynamical state of the gas. Gravitational lensing of background galaxies offers precise calibration of the scaling relation [136–143], but is subject to systematics such as the intrinsic alignment and redshift uncertainties of the sources [144], and is limited by the absence of background galaxies for clusters at high redshift.

The gravitational lensing of the CMB, on which we focus here, is free from the systematics of galaxy weak lensing, and most useful for high redshift clusters. The CMB acts as an extended source at a redshift of 1100, with well understood statistics [30]. Note that CMB lensing reconstruction is however not totally free from systematics, mainly due to astrophysical contaminations, such as the own SZ emission of the cluster [145–147].

In Chapter 1, we introduced the fundamental principles of the weak gravitational lensing formalism of CMB. This segment of the thesis leverages the weak lensing of CMB to investigate galaxy clusters, which, as previously noted, hold significant cosmological information as being the largest gravitationally bound structures. This chapter outlines the model adopted for analyzing the total matter density profile of these clusters and their lensing effects on the observed CMB maps. Section 6.2 describes the Navarro-Frenk-White (NFW) model [148], utilized in this study. The NFW model, a widely accepted fit for the matter density profile in galaxy clusters, is a good approximation for the distribution of dark matter within these structures. In Section 6.3, we explore the CMB lensing formalism in the context of an NFW cluster. This section discusses how galaxy clusters, modeled by the NFW profile, act as lenses that modify the path of CMB photons, thereby imprinting specific signatures on the CMB maps. These lensing effects are crucial for probing the mass distribution of galaxy clusters. The chapter concludes with Section 6.4, summarizing the key points discussed and the implications of utilizing weak gravitational lensing of the CMB to study galaxy clusters.

6.2 NFW Profile

We adopt a truncated version [149] of the NFW profile [148] to model the cluster mass distribution in our analysis. In this model, the dark matter density of the galaxy cluster is

$$\rho(r) = \begin{cases} \dfrac{\rho_0}{(\frac{r}{r_s})(1+\frac{r}{r_s})^2} & \text{if } r < R_{\text{trunc}} \\ 0 & \text{if } r > R_{\text{trunc}} \end{cases}, \tag{6.1}$$

where ρ_0 and r_s are the characteristic cluster density and characteristic scale radius of the profile, respectively. We use M_{200} to characterize the mass of the cluster in terms of the mass enclosed in a sphere of radius R_{200}, within which the average density of the cluster is 200 times the critical density of the Universe ρ_{crit} at the cluster redshift z. We truncate the NFW profile at a radius $R_{\text{trunc}} = 3 \times R_{200}$ to derive more realistic mass profiles [149], addressing the physical limitation that dark matter halos do not extend indefinitely. One can write the following relation between ρ_0 and $\rho_{\rm crit}$ [150],

$$\rho_0 = \rho_{\rm crit}(z)\,\frac{200}{3}\,\frac{c_{200}}{\ln\left(1+c_{200}\right) - \left(\dfrac{c_{200}}{1+c_{200}}\right)}\ , \tag{6.2}$$

where $c_{200} = R_{200}/r_s$ is the concentration parameter. In this spherically symmetric model, the concentration parameter has the following empirical dependence on the cluster mass and redshift [151, 152]

$$c_{200}(M_{200}, z) = 5.71\,(1+z)^{-0.47}\left(\frac{M_{200}}{2\times 10^{12}\,h^{-1}M_\odot}\right)^{-0.084}\ . \tag{6.3}$$

Hence, the NFW density profile is quantifiable with these two parameters, the mass[2] M_{200} and redshift z.

6.3 Lensing by NFW profile

The gravitational field created by the inhomogenity in the mass distribution in the Universe causes deflection of CMB photons. This phenomenon is referred to as weak lensing of the CMB [30]. As a result of weak lensing, the original CMB signal is remapped on the sky. We denote the quantities for the unlensed primordial CMB as $X(\hat{\mathbf{n}})$ and for the remapped lensed CMB as $\widetilde{X}(\hat{\mathbf{n}})$, respectively. Here, X can represent temperature (T) or polarization Stokes parameters (Q and U). Assuming the flat-sky approximation, the remapping of the unlensed quantity can be expressed as

$$\widetilde{X}(\hat{\mathbf{n}}) = X(\hat{\mathbf{n}} + \boldsymbol{\alpha}(\hat{\mathbf{n}})), \tag{6.4}$$

where $\boldsymbol{\alpha}(\hat{\mathbf{n}})$ is the deflection field, which can be expressed as the gradient of the lensing potential: $\boldsymbol{\alpha}(\hat{\mathbf{n}}) = \boldsymbol{\nabla}_{\hat{\mathbf{n}}}\phi(\hat{\mathbf{n}})$, neglecting the LSS lensing rotational component which is a second order effect in the scalar perturbations. The convergence $\kappa(\hat{\mathbf{n}})$ is the most relevant observable in our work [30],

$$\kappa(\hat{\mathbf{n}}) = -\frac{1}{2}\nabla^2_{\hat{\mathbf{n}}}\phi(\hat{\mathbf{n}}). \tag{6.5}$$

Since we assume a spherically symmetric profile for the cluster (see Eq. 6.1), the cluster convergence is circularly symmetric, and depends only on the radial distance from the cluster center, denoted as $r = |\mathbf{r}|$ [149, 153]

---

[2] We express M_{200} in units of solar mass $M_\odot$, which is 1.99×10^{30} kg.

$$\kappa_{\text{cl}}(r) = \frac{\Sigma_{\text{cl}}(r)}{\Sigma_{\text{crit}}(z)}, \tag{6.6}$$

where $\Sigma_{\text{cl}}(r)$ is the projected surface density of the cluster along the line of sight [149, 152]

$$\Sigma_{\text{cl}}(r) = 2\int_{r}^{R_{\text{trunc}}} \frac{x\rho(x)}{\sqrt{x^2 - R^2}} \mathrm{d}x \ , \tag{6.7}$$

and $\Sigma_{\text{crit}}(z)$ represents the critical surface density of the universe at the cluster redshift [149, 153]

$$\Sigma_{\text{crit}}(z) = \frac{c^2}{4\pi G} \frac{d_{A,\text{CMB}}}{d_{A,\text{cl}} d_{A,\text{cl-CMB}}} \ , \tag{6.8}$$

where c is the speed of light, G is the Newtonian gravitational constant, and $d_{A,\text{CMB}}$, $d_{A,\text{cl}}$, and $d_{A,\text{cl-CMB}}$ represent the angular diameter distances to the hypersurface of the last scattering of CMB, the cluster, and between the cluster and the hypersurface of the last scattering of CMB, respectively. In the small angle approximation we can relate the angular separation θ and the radial distance from the cluster center as $\theta = \frac{r}{d_{A,\text{cl}}}$. The expression for the cluster convergence is then obtained as [154]

$$\kappa_{cl}(x) = \frac{2\rho_s r_s}{\Sigma_{crit}(z)} g(x), \tag{6.9}$$

where $x = r/r_s = \theta/\theta_s$ and $g(x)$ is a circularly symmetric function depending on the truncation of the profile,

$$g(x) = \begin{cases} -\frac{\sqrt{x_{\max}^2 - x^2}}{(1-x^2)(1+x_{\max})} + \frac{1}{(1-x^2)^{\frac{3}{2}}} & \cosh^{-1}\left(\frac{x^2+x_{\max}}{x(1+x_{\max})}\right), (x < 1) \\ \frac{\sqrt{x_{\max}^2 - 1}}{3(1+x_{\max})}\left[1 + \frac{1}{1+x_{\max}}\right], & (x = 1) \\ -\frac{\sqrt{x_{\max}^2 - x^2}}{(1-x^2)(1+x_{\max})} - \frac{1}{(x^2-1)^{\frac{3}{2}}} & \cosh^{-1}\left(\frac{x^2+x_{\max}}{x(1+x_{\max})}\right), (1 < x \leq x_{\max}), \end{cases} \tag{6.10}$$

where we introduced $x_{\max}$, the ratio of the truncation radius to r_s, which in our case is equal to $3 \times c_{200}$. We rewrite the cluster convergence as a product of a normalization κ_0 and a template function κ_t, that depends on the chosen density profile of the dark-matter halo (and hence, on its mass and redshift), so that $\kappa_{\text{cl}}(x) = \kappa_0 \, \kappa_t(x)$. Here, κ_t is a circularly symmetric template function, which has a functional dependence on $\frac{r}{r_s} = \frac{\theta}{\theta_s}$. The normalisation κ_0 is chosen such that $\kappa_t = 1$ at scale radius r_s and the

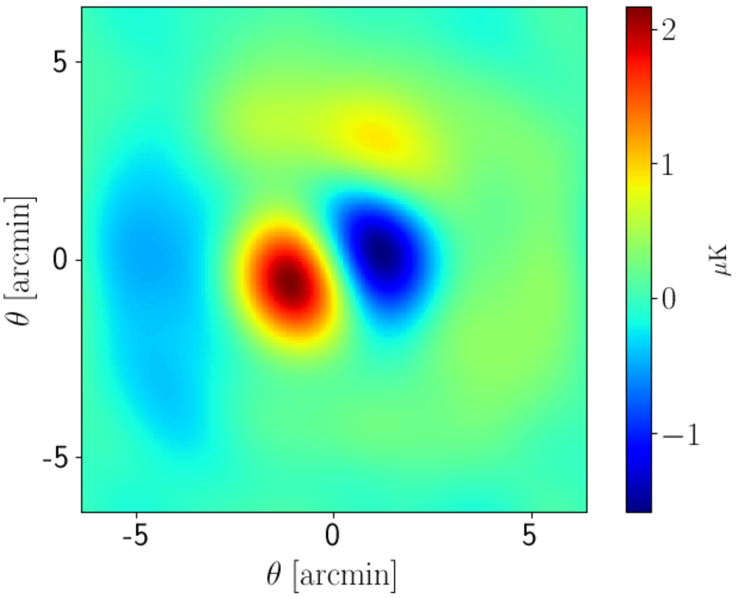

Figure 6.1: The well-known dipole-like structure that we expect in (lensed-unlensed) [1] sky when there is a cluster with $M_{200} = 2 \times 10^{14} M_\odot$ [2], $z = 0.7$ present in our line of sight.

cluster convergence is κ_0 there. When there is a circularly symmetric convergence profile in front of a temperature gradient, we expect a dipole-like structure in the lensed-unlensed CMB [155], as depicted in Figure 6.1. The intensity of this induced dipole is contingent upon two factors: the mass of the galaxy cluster and the magnitude of the background CMB temperature gradient. Furthermore, the orientation of this dipole is dictated by the direction of the temperature gradient in the background CMB. Given the definition of κ_0, it has direct proportionality relation with the mas of the cluster M_{200} [149],

$$\kappa_0 \theta_s^2 \propto \frac{M_{200}}{\Sigma_{\text{crit}}(z) d_A^2(z)}. \tag{6.11}$$

The analytical form of the Fourier transform to the convergence profile, is given by [154, 156, 157]

$$\kappa_a(l; z) = \frac{M_{200}\tilde{u}(k = \ell/\chi; z)}{(1+z)^{-2}\Sigma_{\text{crit}}(z)}, \tag{6.12}$$

---

[1] The simulations have been obtained using our code LensIt: https://github.com/carronj/LensIt

[2] $M_\odot$ is the solar mass, i.e. 1.99×10^{30} kilogram

where $\tilde{u}(k = \ell/\chi; z)$ is given by

$$\begin{aligned} \tilde{u}(k = \ell/\chi; z) = \frac{1}{m_{\rm nfw}}[\sin y\{\mathrm{Si}[y(1 + x_{\rm max})] - \mathrm{Si}(y)\} \\ + \cos y\{\mathrm{Ci}[y(1 + x_{\rm max})] - \mathrm{Ci}(y)\} - \frac{\sin(yx_{\rm max})}{y(1 + x_{\rm max})}]. \end{aligned} \tag{6.13}$$

Here, we define a new Fourier variable, $k = \ell/\chi$. χ is the comoving angular diameter distance at that redshift, defined as $\chi(z) = \int_0^z dz' \frac{1}{H(z')} = (1 + z)d_A(z)$. In the above equation, $y = (1 + z)kr_s$; $\mathrm{Si}(x)$ and $\mathrm{Ci}(x)$ denote the sine and cosine integrals and the normalisation $m_{\rm nfw} = \ln(1 + c_{200}) - \left(\frac{c_{200}}{1+c_{200}}\right)$.

6.4 Summary

This chapter serves as an introduction to the section of the thesis dedicated to probing galaxy clusters via weak-lensing effects on CMB. Galaxy clusters, the largest bound structures in the observable universe, began forming relatively recently around redshifts $z \sim 1$, collapsing within the gravitational wells generated by dark matter. By analyzing the distribution of these clusters in terms of their mass and redshift, we gain valuable insights into the evolution of the universe and are able to impose constraints on dark energy. This analysis also provides direct information on the growth of cosmic structures, enhancing our comprehension of the universe's matter density (Ω_m), the amplitude of matter fluctuations (σ_8), and the total mass of neutrinos ($\sum m_\nu$). With the advent of next-generation CMB surveys like CMB Stage 4 (S4), which is expected to detect around 10^5 clusters, galaxy clusters are poised to become a crucial and independent tool for refining our estimates of cosmological parameters. However, to effectively use galaxy clusters as a cosmological probe, precise measurement of their masses is crucial. The following part of the thesis is dedicated to developing an improved estimator for cluster mass by leveraging the lensing signals present in CMB data in anticipation of future CMB experiments such as CMB-S4.

This introductory chapter outlines the theoretical model for the mass profiles of galaxy clusters. We review the well-known NFW profile, introducing parameters such as the characteristic scale radius and density, essential to the work in this thesis. Additionally, we study the expected lensing signatures in the CMB maps lensed by such profiles. In the subsequent chapters, we will elaborate on this foundation to construct an estimator for cluster mass through a Bayesian inference approach to the lensing potential.

Chapter 7

Cluster mass estimators

7.1 Intrduction

The standard tool to reconstruct the lensing deflection field from the CMB is the quadratic estimator (QE) [4,36,37,158], which combines pairs of CMB maps to estimate the statistical anisotropies created by lensing. It has been shown that the standard temperature QE underestimates the strong deflection field of massive clusters due to a bias in the estimated gradient (unlensed) CMB field [159]. Filtering out the small scales on the gradient leg of the QE greatly reduces this bias [12], at the expense of losing a moderate amount of signal to noise.

For current and upcoming CMB surveys, the QE reconstructed cluster lensing field is noise dominated. One possibility is to stack the reconstructed lensing map and measure the average cluster mass [146,152,160,161]. Similarly, one can obtain the mean cluster mass with matched-filtering [149,162–164].

Other estimators have been developed to reconstruct the lensing field around galaxy clusters, such as stacking CMB maps along the gradient direction to extract the lensing dipole [165,166], the gradient inversion estimator [167,168], or the maximum likelihood estimator (MLE) [169–171]. The MLE directly fits the few parameters of a lensing template on observed CMB maps, and thus estimates the cluster mass without reconstructing the actual lensing map signal. This estimator is adequate for stacking analyses, provided the template shape accurately describes the mass profile and the mass distribution around the cluster, including potential sources of contamination such as the SZ effect. Recently, machine learning based tool to estimate the cluster mass from lensed CMB maps, using neural networks trained on simulations, have also been proposed [172–174].

First introduced in [175, 176], likelihood-based CMB lensing mass map estimators aim to optimally reconstruct the large scale deflection field. Refs. [177, 178] introduced similar technology in the context of cluster lensing. The approach is built on assuming a cluster convergence profile, and iteratively delensing the observed maps to obtain the cluster mass. The lensing template at each iteration is estimated by stacking a set of reconstructed cluster convergence profiles. Some approximations are made for a tractable implementation, due to systematics introduced by the beam of the instrument.

Recent years have seen further development of the CMB lensing likelihood-based estimator of Ref. [175, 176] (often called now maximum a posteriori estimator (MAP)), and other Bayesian attempts, [38, 96, 179–184]. It has been demonstrated that the MAP estimator outperforms the QE, in particular for deep polarization surveys such as CMB-S4 [28], where most of the observed B-modes are created by lensing. Indeed, while the QE is limited by the cosmic variance of the lensed B-modes, the likelihood estimator is able to delens more of these B-modes (provided the noise is below the lensing level of $\sim 5\mu\mathrm{K}\,\mathrm{arcmin}$), and thus decreases the variance. The MAP lensing mass map estimator essentially achieves what is expected to be the lowest possible reconstruction noise.

The scope of this work is to test the performance of the MAP estimator (as implemented in Ref. [38]) in the vicinity of galaxy clusters. Contrary to the likelihood approximations of Refs. [177, 178], or to the MLE of [169–171], our MAP estimator does not assume a cluster profile, or the presence of a cluster signal at all, and is thus agnostic about the true deflection field. We take into account the large scale structures (LSS) deflection field together with the one from the cluster specifically. LSS lensing increases the reconstruction noise substantially at low noise levels, making the analysis more realistic.

Our results, including the CMB simulations and the lensing reconstructions, were obtained with the publicly available code LensIt[1]. We describe the MAP reconstruction methodology in Section 7.2. We follow Ref. [38] very closely, but introduce some adoptiontion details to enable the algorithm to work reliably at high resolution and high multipoles in the presence of clusters. In Section 7.3, we describe the simple matched filter we use to recover the mass of the cluster from the MAP lensing maps.

---

[1] https://github.com/carronj/LensIt

7.2 Lensing Reconstruction

7.2.1 Data Model and the Covaiance Matrix

We work in the flat sky approximation, and identify multipoles to 2D plane wave vectors $\boldsymbol{\ell} = (\ell_x, \ell_y)$. As standard in literature, we use $\boldsymbol{\ell}$ for the CMB multipoles and $\boldsymbol{L}$ for the lensing multipoles.

Let X be the unlensed CMB temperature or polarisation field, $X \in \{T, Q, U\}$, expressed in Fourier space. The covariance of these unlensed fields are the primordial power spectra $\left\langle X_{\boldsymbol{\ell}}, X^{\dagger}_{\boldsymbol{\ell}'} \right\rangle = \delta^{\boldsymbol{\ell}}_{\boldsymbol{\ell}'} C^{\mathrm{unl}}_{\boldsymbol{\ell}}$.

The observed CMB field in pixel space can be expressed as

$$X^{\mathrm{dat}} = BDX + n \tag{7.1}$$

where D is the operator that maps the unlensed CMB modes to the lensed CMB in real space (and thus contains the Fourier transform and lensing remapping operations). The operator B is the linear response matrix of the instrument, including beam and pixel window functions, and n is an independent noise, expressed in pixel space. When considering the temperature estimator, we have $X^{\mathrm{dat}} \equiv T$, polarization only estimators have $X^{\mathrm{dat}} \equiv (Q, U)$, while the minimum variance estimators have $X^{\mathrm{dat}} \equiv (T, Q, U)$.

For a fixed deflection field, the covariance of the observed CMB fields is

$$\mathrm{Cov}_{\boldsymbol{\alpha}} \equiv \left\langle X^{\mathrm{dat}} X^{\mathrm{dat},\dagger} \right\rangle_{\boldsymbol{\alpha}} = BDC^{\mathrm{unl}} D^{\dagger} B^{\dagger} + N\,, \tag{7.2}$$

where N is the noise covariance matrix in pixel space. Averaging on the deflection fields as well, we can write this covariance as

$$\mathrm{Cov} \equiv \left\langle X^{\mathrm{dat}} X^{\mathrm{dat},\dagger} \right\rangle = B\mathcal{Y} C^{\mathrm{len}} \mathcal{Y}^{\dagger} B^{\dagger} + N\,, \tag{7.3}$$

where C^{len} is the covariance of the lensed CMB fields, given by the fiducial lensed CMB power spectra, and $\mathcal{Y}$ is the Fourier transform operator.

7.2.2 Quadratic Estimator (QE)

For current CMB experiments, the minimum variance quadratic estimator (QE) [36, 37] stands out as the most conventional method. They are based on the principle that the lensing of CMB fluctuations breaks the statistical isotropy, creating correlations among the CMB multipoles. Specifically, the correlation between two CMB multipoles separated by L is directly proportional to the lensing potential $\phi(L)$. This relationship is elaborated upon in Section 1.5 of Chapter 1, particularly in Equation 1.22. By optimally weighting the sum of these two-point statistics for the pairs of CMB multipoles separated by the same lensing multipole L, we can reconstruct the lensing potential $\phi(L)$, with minimum error.

In pixel space, the unnormalized quadratic estimator of the lensing deflection field can be expressed as the product of two filtered CMB maps

$$\hat{\boldsymbol{\alpha}}^{\mathrm{QE}}(\boldsymbol{n}) = \bar{X}(\boldsymbol{n})\,\nabla X^{\mathrm{WF}}(\boldsymbol{n})\,, \tag{7.4}$$

where the inverse variance filtered and Wiener filtered legs are

$$\begin{aligned} \bar{X} &= B^{\dagger}\mathrm{Cov}^{-1}X^{\mathrm{dat}}\,, \\ X^{\mathrm{WF}} &= C^{\mathrm{len}}\mathcal{Y}^{\dagger}B^{\dagger}\mathrm{Cov}^{-1}X^{\mathrm{dat}}\,. \end{aligned} \tag{7.5}$$

The normalisation of the QE is chosen to obtain an unbiased estimator, and is expressed in Fourier space as the isotropic response function $\mathcal{R}^{\mathrm{QE}}(L)$ [36]. This gives the normalised QE convergence field in Fourier space,

$$\hat{\kappa}^{\mathrm{QE}}(\boldsymbol{L}) = -\frac{1}{2}\frac{i\boldsymbol{L}\cdot\hat{\boldsymbol{\alpha}}^{\mathrm{QE}}(\boldsymbol{L})}{\mathcal{R}^{\mathrm{QE}}(L)}\,. \tag{7.6}$$

- **HDV QE:** The presence of strong non-Gaussianity at the center of the cluster introduces a bias in the temperature QE, leading to an underestimation of the cluster's mass. This issue has been explored in greater detail in the following chapter. To highlight this limitation, we also present results using a modified QE that incorporates a scale cut on the gradient leg of the temperature map at $\ell_{\mathrm{cut}} = 2000$. This approach, referred to as the Hu-Dedeo-Vale QE (HDV QE), offers a way to mitigate the bias and provide a more accurate estimation of the cluster mass [12].

7.2.3 Maximum a Posteriori (MAP) Estimator

The maximum a posteriori estimator of the deflection field that maximizes the likelihood of the lensed CMB fields, assuming a Gaussian prior on the lensing potential, with power spectrum $C_L^{\kappa\kappa,\mathrm{fid}}$, is given by

$$\ln\mathcal{P}(\boldsymbol{\alpha}|X^{\mathrm{dat}}) = \ln\mathcal{L}(X^{\mathrm{dat}}|\boldsymbol{\alpha}) - \frac{1}{2}\sum_{\boldsymbol{L}}\frac{|\kappa(\boldsymbol{L})|^2}{C_L^{\kappa\kappa,\mathrm{fid}}}, \tag{7.7}$$

where the lensed CMB likelihood is assumed to be Gaussian, and given by

$$\ln\mathcal{L}(X^{\mathrm{dat}}|\boldsymbol{\alpha}) = -\frac{1}{2}X^{\mathrm{dat},\dagger}\mathrm{Cov}_{\boldsymbol{\alpha}}^{-1}X^{\mathrm{dat}} - \frac{1}{2}\ln\det\mathrm{Cov}_{\boldsymbol{\alpha}}. \tag{7.8}$$

In practice, the MAP lensing deflection field $\hat{\boldsymbol{\alpha}}^{\mathrm{MAP}}$ is determined by Newton-Raphson iterations on the posterior, starting from $\hat{\boldsymbol{\alpha}}^{\mathrm{QE}}$ until convergence is achieved, using the gradient of Eq. 7.7 (with respect to the $\boldsymbol{\alpha}$) as search direction. Specifically, the gradients are given by,

$$g^{\mathrm{tot}} \equiv \frac{\delta\ln p(\boldsymbol{\alpha}|X^{\mathrm{dat}})}{\delta\boldsymbol{\alpha}(\hat{n})} = g^{\mathrm{QD}} - g^{\mathrm{MF}} + g^{\mathrm{PR}}, \tag{7.9}$$

where:

- g^{QD} is the gradient originating from the quadratic term of the log likelihood, as detailed in Eq. 7.8
- g^{MF} represents the mean-field contribution, coming from the determinant of the covariance matrix part of the likelihood function.
- g^{PR} is the gradient arising from the prior part of the likelihood.

The main term of the gradient, g^{QD} can be obtained exactly by running a QE with modified weights on partially delensed CMB maps (see [38] for more details). This is the gradient of the first term on the right-hand side in Eq. 7.8, quadratic in the data for fixed $\boldsymbol{\alpha}$, whose role is to capture the residual lensing signal. The gradient of the second term on the right-hand side, independent of the data for fixed $\boldsymbol{\alpha}$, is the 'mean-field', that removes from the quadratic piece signature of anisotropies unrelated to lensing. In our analysis, there is no masking and the noise is statistically isotropic, making the traditional main sources of mean-field to vanish. In principle there is however also a noise contribution to the mean-field during the iterative procedure: the delensed data noise during the iterative process is not isotropic anymore, because at each step the data is delensed to reduce the CMB statistical anisotropy. This compresses or dilates regions of the sky according to the local estimate of the convergence field, changing the local effective noise levels. Ref. [185] discusses in some details this contribution for reconstruction from polarization, showing that it is very small and limited to large lensing multipoles that contributes negligibly to the signal. Hence, for simplicity, we neglect the mean field altogether in this paper. This mean-field is possibly more relevant in temperature, since reconstruction from temperature is more sensitive to convergence-like signals than from polarization, but our results support the idea that it cannot have a large impact overall. A more precise analysis of the role of the mean-field in temperature reconstruction deferred to for future work.

We note that the normalization of this estimator is not tractable analytically. We follow [181, 183] and obtain an empirical normalization of our MAP estimator from a set of simulations. We generate 1000 CMB flat sky patches, and lens them with Gaussian random realizations of the large scale structures deflection field. Note that in these simulations we do not include any cluster signal. The empirical normalization is assumed to be isotropic, and is obtained from the cross correlation between the reconstructed $\hat{\kappa}^{\mathrm{MAP}}$ and the input convergence κ^{in}, averaged over our set of simulations

$$\mathcal{W}_L^{\mathrm{MAP}} = \left\langle \frac{C_L^{\kappa^{\mathrm{in}},\hat{\kappa}^{\mathrm{MAP}}}}{C_L^{\kappa^{\mathrm{in}},\kappa^{\mathrm{in}}}} \right\rangle . \tag{7.10}$$

As demonstrated in [181,183], this empirical normalization is not sensitive to variations in cosmology, input lensing, or data noise. This robustness ensures accurate normalization even when the fiducial components, such as the input lensing potential map, or the noise levels utilized in the simulations, do not closely align with those present in the data.

In the posterior maximization process, delensing of the CMB occurs via the operator $D^{\dagger}$. Our first implementations of the MAP solver in Ref. [38] made the additional assumption of the invertibility of the deflection field, and performed remappings of the maps using a standard bicubic spline algorithm. To improve stability and performance, we update our flat-sky tools with the lensing method of Ref. [184], based on non-uniform FFTs techniques [186, 187]. This method is extremely accurate and at the same time removes this unnecessary assumption of an invertible deflection. With this, we found that the search for the MAP point converges without issues on all relevant scales, after only 10-20 iterations.

In this section, we discuss various estimators for reconstructing lensing information, including the QE, HDV QE, and the MAP estimator. For these estimators, we can utilize pairs of maps to extract lensing information across different channels. Specifically:

- **Temperature Only Channel (T):** Here, we use pairs of temperature maps to derive two-point statistics, focusing solely on temperature data.

- **Polarization Only Channel (Q,U):** This channel leverages all possible pair combinations of polarization maps, specifically the E and B modes (X,Y $\in$ {E,B}), to reconstruct lensing signals from polarization data alone.

- **Combined Channel (T,Q,U):** As the most efficient approach, the combined channel integrates all available data from temperature and polarization maps. This method is the global minimum variance estimator, as outlined in [188]. It utilizes all possible pair combinations of temperature and polarization maps for the most effective reconstruction of lensing information.

For illustrative purposes, Figure 7.1 presents the analytical prediction of the reconstruction noise for the combined channel (TQU) estimators. This plot emphasizes the better performance of the MAP estimator over the QE for CMB S4 experimental setup. Additionally, it demonstrates that implementing a scale cut in the HDV QE leads to an increase in reconstruction noise compared to the traditional QE, as expected.

7.3 Cluster Signal Reconstruction

Once we have reconstructed the lensing map $\hat{\kappa}(\boldsymbol{L})$ from the simulated CMB data, we fit our theoretical template $\kappa_0 \kappa_t(\boldsymbol{L})$. In practice the template would be obtained with a first guess of the cluster angular scale θ_s. This can be estimated for instance from the tSZ emission of the cluster as in [149]. Here we take the template which corresponds to the angular scale of the simulated clusters. Our estimator assumes an isotropic Gaussian noise spectrum $N(\boldsymbol{L})$, such that $\langle \hat{\kappa}(\boldsymbol{L})\hat{\kappa}(\boldsymbol{L}')\rangle - \langle \hat{\kappa}(\boldsymbol{L})\rangle\langle \hat{\kappa}(\boldsymbol{L}')\rangle = \delta(\boldsymbol{L} - \boldsymbol{L}')N(\boldsymbol{L})$. This allows us to construct a minimum variance estimator for κ_0, following [149], and using

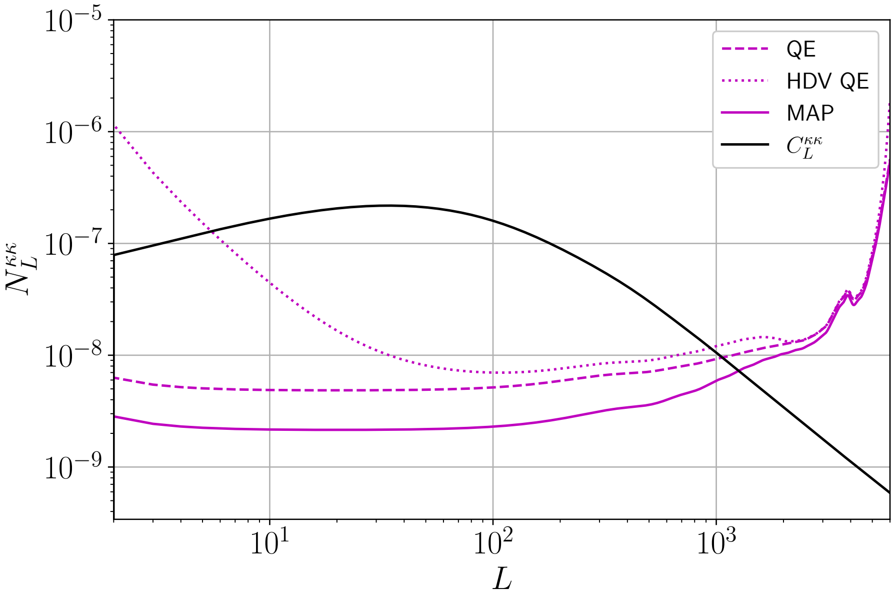

Figure 7.1: Comparison of reconstruction noises for QE, HDV QE, and MAP estimators in the combined TQU channel under CMB-S4 noise and beam conditions.

the asymmetric Fourier convention,

$$\hat{\kappa}_0 = \frac{\displaystyle\int \frac{\mathrm{d}^2\boldsymbol{L}}{(2\pi)^2}\frac{\kappa_t(\boldsymbol{L})\hat{\kappa}(\boldsymbol{L})}{N(\boldsymbol{L})}}{\displaystyle\int \frac{\mathrm{d}^2\boldsymbol{L}}{(2\pi)^2}\frac{|\kappa_t(\boldsymbol{L})|^2}{N(\boldsymbol{L})}}. \tag{7.11}$$

This is the matched filter that we use throughout our paper. Owing to spherical symmetry, all quantities but $\hat{\kappa}(\boldsymbol{L})$ in the aforementioned expression are functions of $L = |\boldsymbol{L}|$. The theoretical error $\sigma_{\kappa_0}^{2,\mathrm{th}}$ for the estimator is as follows [149]:

$$\frac{1}{\sigma_{\kappa_0}^{2,\mathrm{th}}} = \frac{1}{2\pi}\int_{L_{\min}}^{L_{\max}} dLL\frac{|\kappa_t(L)|^2}{N(L)}, \tag{7.12}$$

Due to the proportionality between κ_0 and M_{200} in Eq. 6.11, we use $\frac{\hat{\kappa}_0}{\sigma_{\kappa_0}}$ in order to get the mass constraint, $\frac{\hat{M}_{200}}{\sigma_{M_{200}}}$. This quantity is referred to as the signal to noise ratio (SNR) throughout this paper.

In the above equations, the noise of the $\hat{\kappa}(\boldsymbol{L})$ estimate is given by

$$N(L) = C_L^{\kappa\kappa} + N_L^{(0)} + N_L^{(1)}, \tag{7.13}$$

where $C_L^{\kappa\kappa}$ represents the power spectrum of the background convergence profile of the large-scale structure, without including the cluster. This contributes to the noise on the cluster lensing signal. In the case that $\hat{\kappa}$ is the QE estimate, $N_L^{(0)}$ is the leading CMB-lensing reconstruction noise (the disconnected four-point function), and $N_L^{(1)}$ the connected part originating from the secondary trispectrum contractions, proportional to $C_L^{\kappa\kappa}$ [30, 189]. In the MAP case, the same Eq. (7.13) provides a good fit to the spectrum, with both noise terms calculated with partially delensed spectra, following Ref. [181]. On hypothetical maps where the cluster lensing signal were the only lensing-like signal, only $N_L^{(0)}$ would be present.

On small scales, the non diagonal terms in the covariance $N(L, L')$ of $\hat{\kappa}(L)$ could become important and reduce the constraining power, as discussed in [167]. We check from our set of simulations (described in the next chapter) that for all the estimators we considered, and up to $L = 5000$, the covariance $N(L, L')$ of $\hat{\kappa}(L)$ is very close to diagonal, justifying that it is nearly optimal to use $N(L)$ for our matched filtering.

In Fig. 7.2, we show the contribution of each lensing multipole to the theoretical signal to noise of Eq. 7.12. The y axis is the integrand at each L, which must be summed over to obtain the inverse noise of the cluster mass estimate. These curves are obtained with the theoretical $N_L^{(0)}$ and $N_L^{(1)}$ of each estimator, considering a CMB-S4 like experiment with white noise level of 1μK-arcmin in temperature and $\sqrt{2}\mu$K-arcmin in polarization and a beam full width at half-maximum (FWHM) of 1 arcmin. We considered a cluster of mass of $M_{200} = 2 \times 10^{14} M_\odot$, at $z = 0.7$, that matches the expected mean mass and redshift of the CMB-S4 clusters detected with thermal SZ effect [28].

We include multipoles $\ell_{\rm min}^{\rm CMB} = 100$ to $\ell_{\rm max}^{\rm CMB} = 4000$ of the CMB temperature and polarization maps for the lensing reconstruction. We compare both the QE and the MAP estimators.

In Fig. 7.2, We also show that for both QE and MAP, the lensing scales that dominates the signal to noise are around $L \sim 2000$ in the temperature and around $L \sim 1100$ in the polarization. The HDV QE estimator mainly loses information on the large scales, for $L \lesssim 2000$, while smaller scales contain similar information as compared to the QE. This shows that for the CMB-S4 like configuration and cluster convergence profile assumed in our analysis, temperature and polarization channels bring similar level of information, albeit from different scales. Finally we clearly see that the MAP estimator outperforms the QE at all lensing scales, and this improvement is primarily due to increased signal

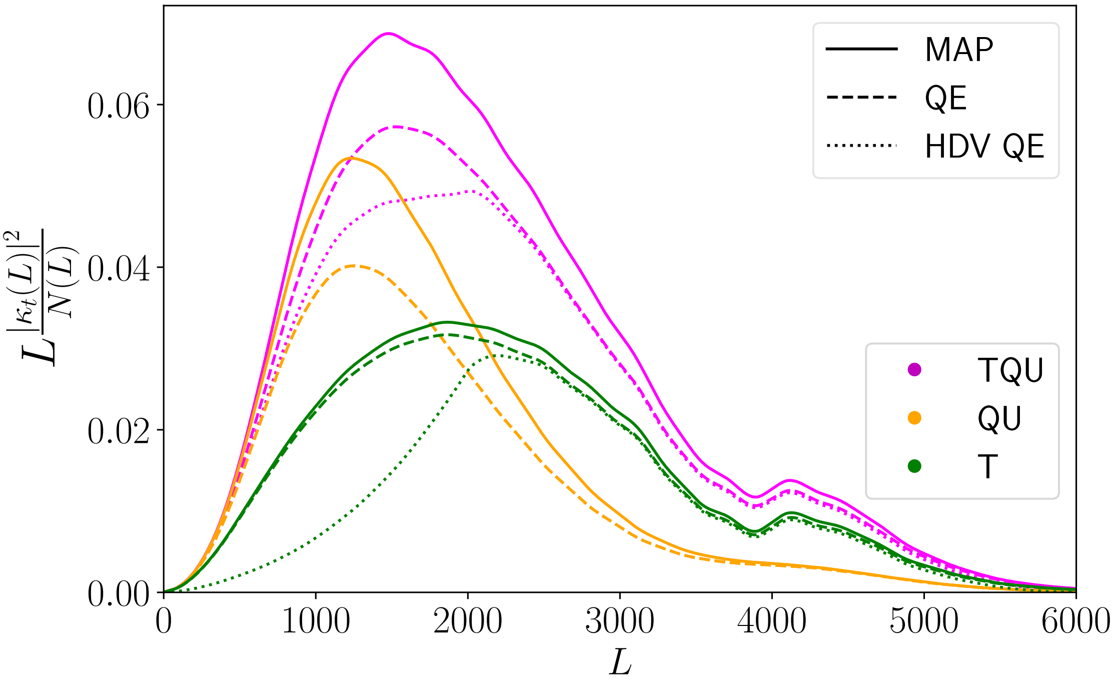

Figure 7.2: Contribution per lensing multipole to the cluster mass SNR (the integrand of Eq. 7.12) shown in case of a $2 \times 10^{14} M_\odot$ cluster at $z = 0.7$, for the CMB-S4-like configuration described in the text. Green, orange and magenta show temperature-only, polarization-only and combined reconstruction respectively. Dashed shows the quadratic estimator case and solid the CMB lensing maximum a posteriori method of this work. Dotted shows the QE with a high-ℓ cut on the gradient leg [12]. While the MAP approach is exactly the same than for optimal CMB lensing power spectrum reconstruction, this probes much smaller scales (the spectrum SNR is almost entirely confined to $L < 1500$ for this configuration).

from the polarization channel.

7.4 Summary

This chapter introduces the tools used to reconstruct the lensing potential from observed CMB maps. The most conventional method for current CMB experiments is the QE. They are based on the principle that the lensing of CMB fluctuations breaks the statistical isotropy, creating correlations among the CMB multipoles. Ideally, we reconstruct the lensing information using optimally weighted two-point statistics. This approach can utilize temperature maps (T), polarization maps (Q,U), or any combination thereof (T,Q,U) for reconstruction. With the noise levels of current experiments, the QE is nearly optimal. However, for future experiments like CMB S4, with polarization noise levels potentially below 5 μK-arcmin, we need more sophisticated reconstruction techniques to efficiently utilize all available lensing B-mode information, thereby reducing reconstruction noise.

An alternative, the MLE-based methods, have shown promise for more efficient lensing reconstruction in low-noise settings. Carron et al. [38] introduced an iterative technique for maximizing the posterior distribution of the lensing potential using a Newton-Raphson iteration scheme. This method, briefly overviewed here, employs gradients of the posterior distribution iteratively to locate its maximum. We discuss the expected reduction in reconstruction noise using this method compared to the traditional QE at CMB S4 noise levels. This noise suppression directly benefits parameter estimations reliant on lensing reconstructions, such as cluster mass estimation using matched filtering techniques from reconstructed lensing information.

In addition to introducing the iterative MAP estimator for lensing reconstruction, this chapter provides the matched filtering expression for estimating cluster mass, which will be used to obtain the results on simulations in the next chapter. In that chapter, we aim to present theoretical predictions for mass constraints derived using various channel estimators. Furthermore, we will showcase our simulation results obtained under noise conditions like those expected for the CMB S4 experiment. Additionally, we delve into the analysis of a bias in temperature-QE arising from the strong non-Gaussianity at the cluster center and evaluate the performance of our MAP estimator in mitigating this bias.

Chapter 8

Results

8.1 Introduction

In this chapter, we present results on the cluster convergence profile and on the cluster mass from reconstructions of the lensing signal from a set of simulations. Our simulations assume a CMB S4-like experiment [28], with white noise level of 1μK-arcmin in temperature and $\sqrt{2}\mu$K-arcmin in polarization and a beam with a full width at half-maximum (FWHM) of 1 arcmin. Our flat sky patches have a pixel size of 0.3 arcmin with 1024 pixels on a side. The simulations recreate observed lensed sky patches through a two-stage lensing process. First the a Gaussian random realisation of the unlensed primordial CMB patch is lensed by a Gaussian random realisation of a LSS lensing potential. Subsequently, this map is further lensed by a circularly symmetric cluster convergence field at the center of the sky-patch. In our implemention, the lensing effects from the LSS and the cluster are assumed to be independent, which is a slightly unrealistic assumption, however deemed adequate for the purposes of this work.

We test both the quadratic estimator and the MAP estimator, as introduced in Section 7.2, to obtain the estimated $\hat{\kappa}(L)$. We then estimate the mass of the cluster with the matched filtering, as described in Section 7.3. We compare our results for the temperature only (T), the polarization only (QU) and the minimum variance (TQU) estimators. The polarisation channel (QU) is constructed from the all the possible combination XY, where X,Y $\in$ {E,B}. The TQU channel estimator is the global minimum varaince estimator as defined in [188]. In the Section 8.2 we use simulations with a cluster-mass of $M_{200} = 4 \times 10^{14} M_\odot$ and use CMB multipoles for lensing reconstruction up to $l_{\max} = 5000$, to highlight the amount of bias in the reconstructed profile prominently. In the Section 8.3 we use simulations with $M_{200} = 2 \times 10^{14} M_{\odot}$ and CMB multipole up to $l_{\max} = 4000$. The reason behind such choice of mass is that it corresponds to the expected mean mass of CMB-S4 clusters, while the $l_{\max}$ is chosen to be conservative, as we expect that the smaller CMB scales will be foreground dominated. For both Sections, the redshift has been chosen to be $z = 0.7$, and the lower limit of the CMB multipoles used in the lensing reconstruction has been set at $l_{\min} = 100$.

8.2 Profile Reconstruction

As discussed in the literature [12, 159], the temperature QE is biased low due to strong to moderate lensing close to the cluster center. As lensing by the cluster magnifies the background CMB, the gradient of the observed CMB is smaller than the unlensed CMB gradient. Since the weak lensing signature, manifested as a dipole-like pattern in the difference between the lensed and unlensed sky, is sensitive to both the strength of the gradient and the mass of the cluster, it decreases that signature as well. As a consequence, when we estimate the cluster signal using weak lensing temperature QE, the estimator is biased low. The temperature quadratic estimator is nothing but a product of two filtered maps as given in Eq. 7.4. The bias comes mainly from the small scales in the gradient leg. A solution to this bias, as demonstrated in [12], is to use a low-pass filter for the gradient leg and only include multipoles below $\ell = 2000$. We denote this modified QE with a scale cut, as Hu-Dedeo-Vale QE (HDV QE) from now on.

We run all the estimators (QE, HDV QE and MAP) with the temperature only channel, on 1000 simulations, and stack the reconstructed maps. To assess the noise in each reconstruction, we performed additional runs of the estimators on the same simulation, with the same CMB and LSS realization, but without the cluster present. To reduce the variance during the stacking process, for each reconstructed map we first subtract the convergence estimated from the simulation without the cluster, before stacking them. Of course, an analysis on real data does not allow for this approach: we only use it here to estimate the bias more precisely.

In the upper panel of Figure 8.1, we provide the comparison for the real-space deflection angle profile ($\hat{\alpha}(\theta)$). The deflection α, which is the gradient of the lensing potential ϕ is a vector quantity, but only its radial component is non-zero on average, since our

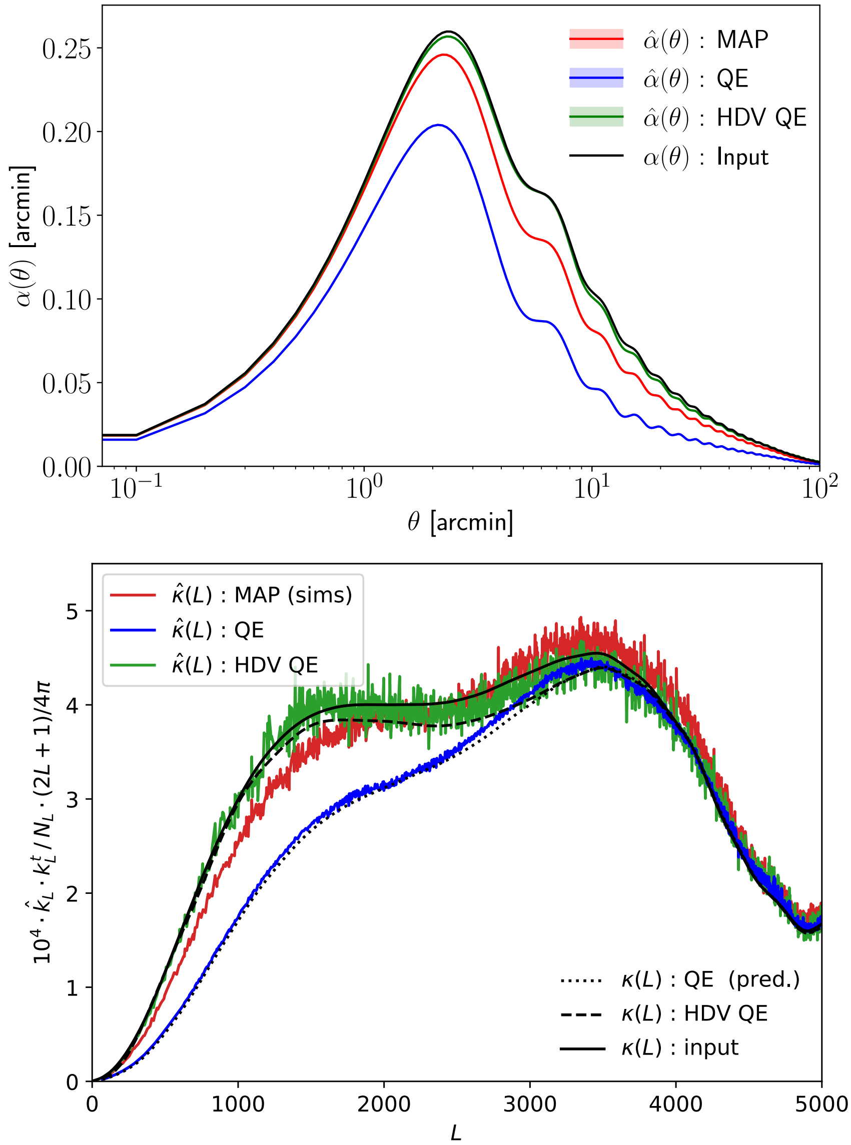

Figure 8.1: *Top panel*: Reconstructed deflection angle profiles $\alpha(\theta)$ from stacking a set of 1000 temperature-only reconstructions ($M = 4 \times 10^{14} M_\odot, z = 0.7$). CMB multipoles $100 \leq \ell \leq 5000$ are used to reconstruct the lensing multipoles $100 \leq L \leq 5000$. Shown are the standard QE (blue), QE with a high-ℓ cut at 2000 on the gradient leg [12] (green, HDV QE), and the maximum a posteriori (MAP) lensing reconstruction of this work (red, without any cuts), and the input truncated to the same L range. The bias in the MAP reconstruction is much reduced compared to the QE but still visible at this cluster mass. In polarization reconstruction no such bias is visible. The deflection profile's oscillatory features results from the fact that the lensing reconstruction is performed in harmonic space and truncated to $L_{\max} = 5000$. *Lower panel:* The same profiles in harmonic space, weighted at each multipole by their contribution to the cluster mass estimate (see Eq. (7.11)). An estimate of the map-level reconstruction noise was subtracted in each realization, in order to accelerate convergence, so that the scatter is not representative of an actual data analysis. Analytic predictions are given for the QE and HDV QE cases as the dotted and dashed black lines. The MAP case is slightly tilted in this configuration compared to the input profile (solid black).

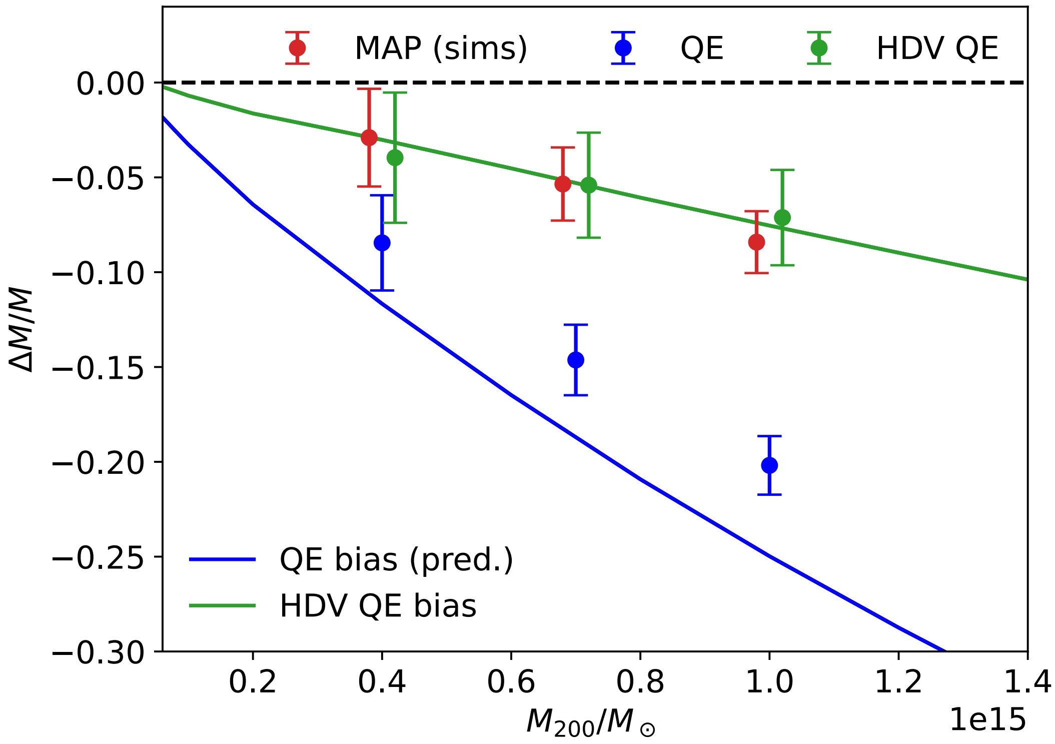

Figure 8.2: Analytical predictions for the QE-inferred mass bias as a function of halo mass for temperature-only QE lensing mass map reconstruction, with (green, ‘HDV QE’) and without (blue) cut on the gradient leg [12], including CMB multipoles $100 \leq \ell \leq 5000$ and lensing multipoles $100 \leq L \leq 5000$ (here all clusters are set at $z = 0.7$). The points show the corresponding results for our simulated reconstructions with $M_{200} = 4, 7$ and $10 \times 10^{14} M_{\odot}$, together with the result of our MAP method (red). The error bar is our empirical estimate for a sample of a thousand cluster. The bias is a strong function of halo mass and can be very significant for massive haloes.

clusters are circularly symmetric. Hence we only stacked the radial component of α. The somewhat oscillatory nature of this deflection profile is due to the truncation in harmonic space: only Fourier modes below $L_{\max} = 5000$ are reconstructed. The lower panel of Figure 8.1 shows the following quantity,

$$\frac{2L+1}{4\pi}\frac{\hat{\kappa}(L)\kappa_t(L)}{N(L)}, \tag{8.1}$$

which is the unnormalized contribution of each and every multipole to the mass estimate in Eq. 7.11 (empirically, errors are independent to a good approximation). As expected the QE is biased low for such massive clusters, whereas the HDV QE [12] does almost unbiased reconstruction of the cluster signal on all scales, at the cost of throwing away some information on small angular scale. Our iterative estimator in other hand, does get

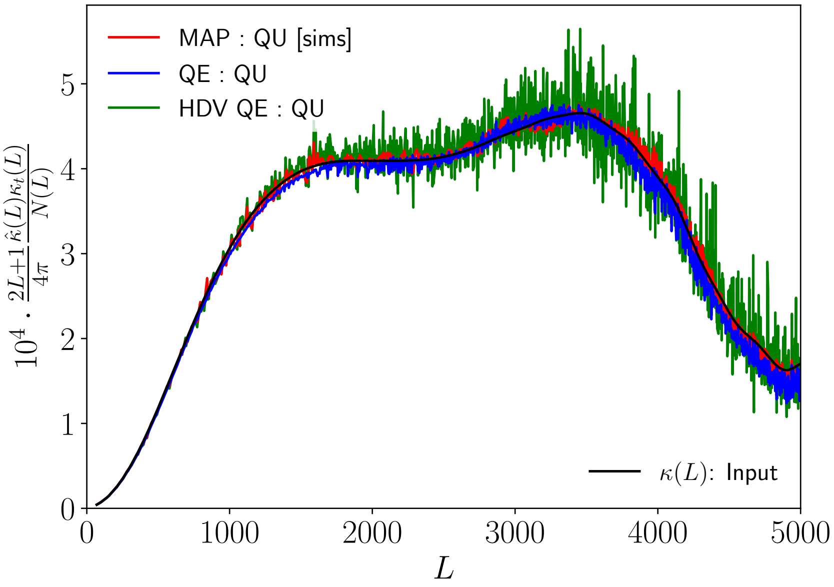

Figure 8.3: Same as the lower panel of Fig. 8.1, for the polarization-only (QU) quadratic and MAP estimators. The QU channel does not suffer from the bias due to strong to moderate lensing close to the cluster center.

rid of most of the bias, without sacrificing any information. For this high cluster mass, our recovered profile still shows some deviation from the input, with recovered signal lower than expected on large lensing scales and higher on smaller scales. In the lower panel of Figure 8.1, we also plot as the dotted and dashed analytic prediction for the QE and HDV QE reconstruction of the cluster signal in L space. We do this essentially by brute-force calculation of the QE and HDV QE expectation values, varying CMB and LSS lensing fluctuations, while keeping the cluster lensing deflection fixed, as described in more detail in Appendix A. The predictions match well, but not exactly, with the empirical findings. We are unable to identify the origin of the (small) discrepancies and defer this investigation to future work. One possible cause for the difference is that the analytical predictions are calculated using curved-sky geometry, while the simulations use small boxes in the flat-sky approximation. Fig. 8.2 shows the prediction with this tool for the halo mass bias as a function of halo mass, together with our findings on this simulation set. We see that the predicted mass bias for the HDV QE is quite accurate compared to the simulations, while there seems to be a small offset for the QE. It is interesting to note that the MAP bias is very close to the HDV QE bias, while having lower variance.

For comparison, we show the same quantity in Eq. 8.1 for the polarization only (QU) estimators in Fig. 8.3. We note that the bias in the QE, due to the magnification of the background gradient, is almost negligible, in contrast to the significant bias for the temperature estimator. We argue that this might come from the fact that the polarization QE is dominated by the EB combination, which is mostly sensitive to the shear and not the magnification. In practice, we also test QE sourced by EE pair alone and find that the bias is smaller than for the TT estimator.

We now discuss how the iterative estimator also suppresses the noise of the mass estimation compared to QE and HDV QE.

8.3 Cluster mass constraints

We now consider 1000 simulations with a cluster mass of $M_{200} = 2 \times 10^{14} M_{\odot}$ and $z = 0.7$, chosen to be close to the expected mean values of the CMB-S4 clusters. We reconstruct the lensing signal with scales between $\ell_{\text{min}}^{\text{CMB}} = 100$ and $\ell_{\text{max}}^{\text{CMB}} = 4000$, for both polarization and temperature maps. We reconstruct the lensing convergence fields with the three estimators: QE, HDV QE and MAP, and with the temperature only (T), polarization only (QU) and minimum variance (TQU) estimators. We then run a matched filter on these reconstructed lensing map to estimate the convergence amplitude $\hat{\kappa}_0$, assuming a template κ_t with the characteristic angular size θ_s corresponding to the input mass and redshift of the cluster profiles. We use the lensing multipoles between $L_{\text{min}} = 100$ and $L_{\text{max}} = 6000$ to obtain $\hat{\kappa}_0$ from Eq. 7.11. We use the empirical noise, obtained from 1000 simulations, as the variance $N(L)$ of $\hat{\kappa}_L$ in that equation.

We compute the variance of $\hat{\kappa}_0$ from our set of 1000 simulations, and compare to the theoretical expectations of the variance from Eq. 7.12. Table 8.1 summarizes our results from 1000 stacked clusters with input $\kappa_0 = 0.1285$, corresponding to a cluster mass of $M_{200} = 2 \times 10^{14} M_{\odot}$ at $z = 0.7$. The mean estimated $(\hat{\kappa}_0)$ from these simulations is shown alongside the respective errors (σ_{κ_0}). The emperical errors in σ_{κ_0} have been obtained using bootstraping method on 1000 simulations. Results for T and TQU estimators are derived from HDV QE, while the QU estimator results are based on the standard QE. The MAP estimates are also provided for comparison in a separate row. Theoretical error predictions $(\sigma_{\kappa_0}^{\text{th}})$ are included, calculated using (Eq. 7.12).

In Fig. 8.4, we show the theoretical relative error on the mass measurements for a set of 1000 stacked clusters, as a function of white noise level, for our set of estimators. We

Table 8.1: Summary of results on 1000 simulations with input $\kappa_0 = 0.1285$, corresponding to a cluster mass of $M_{200} = 2 \times 10^{14} M_{\odot}$ at $z = 0.7$. The table displays the mean $\hat{\kappa}_0$ evaluated from 1000 simulations along with the corresponding errors σ_{κ_0}, obtained using from bootstrapping. For the T and TQU estimators, HDV QE results are provided, while the QE result is presented for the QU estimator. Additionally, MAP estimated values are shown in the second row. $\sigma^{\mathrm{th}}_{\kappa_0}$ depicts the theoretical error prediction given by Eq. 7.12. See also Fig. 8.4.

HDV QE : T		QE : QU		HDV QE : TQU	
$\langle\kappa_0\rangle$	0.1276	$\langle\kappa_0\rangle$	0.1397	$\langle\kappa_0\rangle$	0.1337
σ_{κ_0}	0.0099 ±0.0003	σ_{κ_0}	0.0088 ±0.0002	σ_{κ_0}	0.0068 ±0.0002
$\sigma^{\mathrm{th}}_{\kappa_0}$	0.0096	$\sigma^{\mathrm{th}}_{\kappa_0}$	0.0090	$\sigma^{\mathrm{th}}_{\kappa_0}$	0.0067
MAP : T		MAP : QU		MAP : TQU	
$\langle\kappa_0\rangle$	0.1273	$\langle\kappa_0\rangle$	0.1342	$\langle\kappa_0\rangle$	0.1331
σ_{κ_0}	0.0082 ±0.0003	σ_{κ_0}	0.0078 ±0.0002	σ_{κ_0}	0.0061 ±0.0002
$\sigma^{\mathrm{th}}_{\kappa_0}$	0.0083	$\sigma^{\mathrm{th}}_{\kappa_0}$	0.0081	$\sigma^{\mathrm{th}}_{\kappa_0}$	0.0062

also plot the standard deviation we recovered from our simulation set (points with error bars). We employ the bootstrap method, by resampling our simulation set, to estimate the error on this error. We see that at the CMB-S4 noise level, the performance of the estimators on simulations are within the expectations. Moreover, we see that the MAP estimator allows to recover the loss in constraining power from the HDV QE estimator.

It is clear that as we go to lower noise level, the polarization estimators eventually dominates the constraints. In this regime, the lensing signal unrelated to the cluster plays an increasingly important role in the error budget. Care must be taken comparing these numbers to the literature, since many works (for example MLE's [171], using Gaussian CMB's generated with lensed CMB spectra instead of a non-Gaussian CMB) do not consider this source of noise. At the CMB S4 noise level, the MAP estimator detects the cluster signal with an approximate 12%, 13% and 20% enhancement in significance compared to HDV QE with TQU, QU and T channels respectively. While our results are

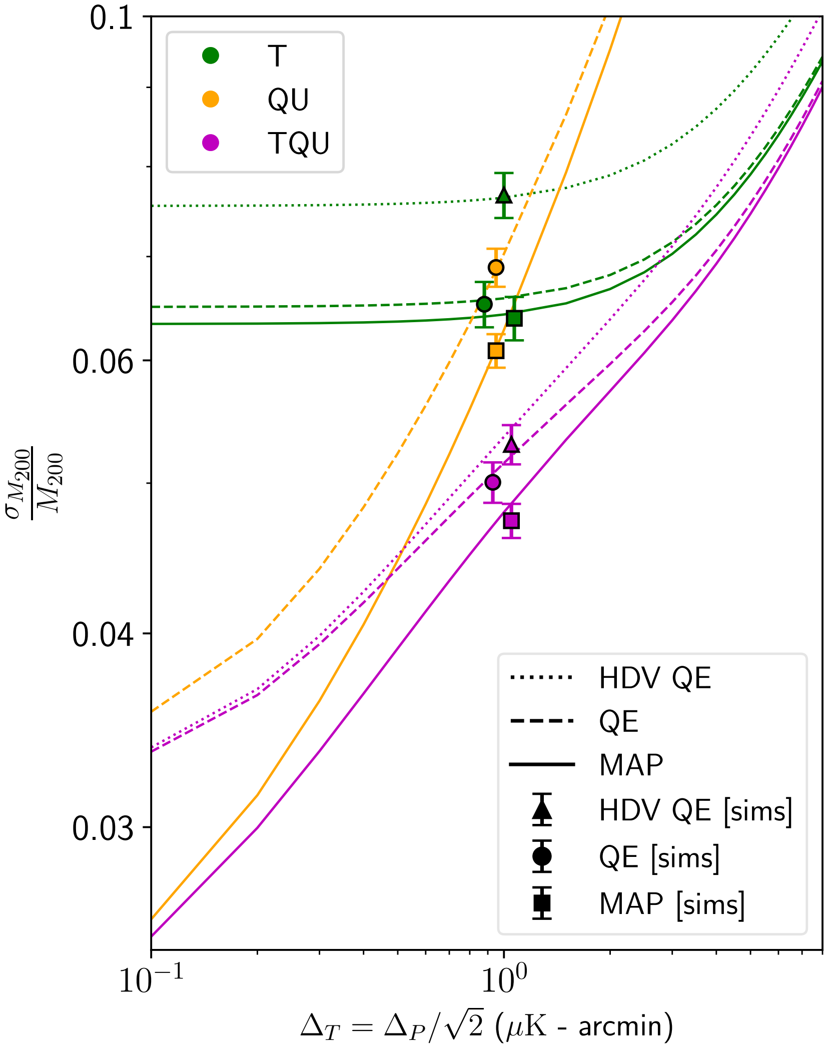

Figure 8.4: Constraints on cluster mass for a sample of 1000 identical clusters ($M_{200} = 2 \times 10^{14} M_{\odot}$, at redshift 0.7) as a function of white noise levels. The beam FWHM is 1 arcmin. It is important to note that the the relative noise quantity $\sigma_{M_{200}}/M_{200}$ corresponds the error the mass measurement for 1000 stacked clusters. Green, orange and magenta show temperature-only, polarization-only and combined reconstruction respectively. Dotted lines (HDV QE) show the QE forecast (Eq. 7.12) with a cut at 2000 in the gradient leg [12] to remove the QE bias (see Fig. 8.1), dashed lines the QE case without any cuts, and solid the maximum a posterior lensing map reconstruction method of this work (MAP). The improvement in constraining power comes from the partial removal from the CMB maps of the lensing signal not directly related to the cluster, and is more prominent in polarization, as expected. Markers with error bars are estimated from our set of simulations, with the x coordinate slightly shifted for clarity. The error bars are obtained from the bootstrapping method (for 1000 clusters), showing good consistency. In the QE case, we applied a simple multiplicative correction to remove the bias in the estimate.

presented based on 1000 simulations, they can be easily extrapolated to the projected number of clusters in CMB S4, estimated to be 10^5. By employing the MAP estimator for 10^5 clusters, the mass can be constrained, achieving an accuracy down to 0.47% for our ideal scenario where no mis-centering or foreground effects are present.

8.4 Summary

After detailing the methods for lensing reconstruction and matched filtering techniques for estimating cluster masses in the previous chapter, this chapter has presented comprehensive results of our analysis. Initially, we discussed the bias encountered in temperature-QE due to moderate to strong lensing effects at the cluster center. The lensing signature of a cluster is influenced by two primary factors: the cluster's mass and the gradient strength of the background CMB. The strong lensing near the center significantly reduces the gradient strength compared to the weak lensing regime, thereby significantly reducing the lensing signature of the cluster in the observed CMB map. Consequently, temperature QE tends to underestimate the cluster mass. Hence, temperature QE underestimates the mass of the cluster. While the HDV QE attempts to bypass this issue by implementing a scale cut in the gradient leg of the QE, this solution, unfortunately, leads to a reduced SNR due to the loss of information beyond the scale cut. On the other hand, our iterative MAP estimator eliminates this bias to a degree comparable to that of HDV QE but without sacrificing SNR. We have shown the effect of the bias in profile reconstruction in the harmonic space for all our estimators using the temperature-only channel. We have illustrated the impact of this bias on profile reconstruction in harmonic space for our estimators using only the temperature channel. We have also noted that the bias worsens for clusters of higher mass. Profile reconstruction using the polarization-only channel revealed no noticeable bias.

Subsequently, we have dedicated the next section to discussing mass constraints and comparing the performance of the estimators, QE, HDV QE, and MAP across different channel estimators. We present the theoretical predictions of the inverse SNR for 1,000 stacked clusters, showing its dependence on the noise level of the experiment. We then present the results on simulations with beam and noise levels as expected in CMB S4. These simulations incorporate two levels of lensing: firstly, a Gaussian random realization of primordial CMB is lensed by a Gaussian random realization of large-scale structure lensing potential ($\phi_{\rm LSS}$), and then this once-lensed CMB is further lensed by a circularly symmetric cluster lensing potential. Then, once lensed, CMB is lensed with circularly symmetric cluster lensing potential. The reconstructed lensing potential from such simulations includes the cluster lensing potential, $\phi_{\rm LSS}$, and the reconstruction noise. In this context, $\phi_{\rm LSS}$ acts as an additional layer of Gaussian random noise. Using the NFW template on the reconstructed lensing convergence, we obtained the mass of the clusters from the simulations. The results on simulations, as detailed in Table 8.1 align with our analytical forecasts, which is illustrated in Figure 8.4. In conclusion, this chapter demonstrates that the iterative MAP estimator successfully addresses the mass bias induced by strong lensing without compromising the SNR, and it provides more accurate mass constraints compared to both QE and HDV QE.

Chapter 9

Conclusion

Throughout this thesis, we have delved into analyzing fluctuations in the CMB on small angular scales. Our focus has been mainly on the signatures of statistical isotropy violation due to our observation frame's motion and the weak gravitational lensing of CMB photons. Employing a Bayesian framework, we have inferred parameters from these signatures, such as the velocity of our observation frame and the masses of galaxy clusters.

In the first part of this thesis, we laid the groundwork by introducing the fundamental concepts of the CMB and highlighting its significance in the realm of precision cosmology. In the second part, we delved into the analysis of the Doppler boost signal in CMB data due to our local motion. From this signal, we estimated the velocity of our observation frame. Subsequently, in the third part, we study the weak gravitational lensing of CMB photons by galaxy clusters. In this context, we show the application of the Maximum a posteriori (MAP) reconstruction method to estimate the cluster masses effectively for future CMB experiments such as CMB S4. This chapter concludes our findings and outlines future research directions.

9.1 Doppler Boost of CMB

In our work, we study the violation of statistical isotropy of the CMB sky due to the Doppler boost of CMB photons in our observation frame. We have assumed the statistical isotropy of CMB fluctuations in the cosmological rest-frame. In this joint inference, we explore the parameter space of the whole CMB covariance matrix under the Doppler boost model in a Bayesian framework. This approach is necessary because the anisotropic off-diagonal part is influenced by the isotropic diagonal part. The inference of the off-diagonal elements leads to the estimation of β_{1N} parameters (the amplitude and direction of the local motion) as in Eq. 2.19. We jointly infer our model parameters, i.e. the spherical harmonic coefficients a_{lm}'s, the power spectra C_l's and the Doppler boost signal β_{10}, β_{11}^r & β_{11}^i. This is achieved by sampling the posterior distribution Eq. 3.7 for *Planck*-2018 `SMICA` temperature anisotropy map. Inference of the high-dimensional parameter space is facilitated by the use of the HMC sampling method. The frequency dependence of the modulation effect in the `SMICA` temperature map is captured using a `SMICA` boost factor $b^{\texttt{SMICA}}(l)$, which is a weighted sum of the frequency dependence with the SMICA weights. The expression of $b^{\texttt{SMICA}}(l)$ is given in Eq. 2.17 and plotted in Figure 2.3 for different choices of mask. This recipe can also be used for any CMB map estimate obtained using the internal linear combination based method and can be used in relevant future work.

We have performed our analysis on three different sky fractions ($f_{\rm sky} = 40.1\%, 59.1\%$ and 72.2%) using multipoles from $l_{\rm min} = 800$ up to $l_{\rm max} = 1950$. With these setups, we have detected the non-zero value of the Doppler boost signal which is consistent with the fiducial values from the known CMB dipole [16,39–42], with a significance of 4.54σ, 4.97σ and 5.23σ, respectively, as expected from a previous forecast [44]. With our primary setup of $f_{\rm sky} = 40.1\%$ and $l_{\rm max} = 1950$, we conclude that our analysis finds value of the peculiar velocity of our observation frame with respect to the CMB to be $v = (298.5 \pm 65.6)$ km/s. The direction of this velocity has been found in galactic coordinates $(\ell, b) = (268.5^\circ \pm 49.8^\circ,\ 61.8^\circ \pm 12.3^\circ)$. We have computed the Bayes factor in favour of the canonical values from the known CMB dipole, to be 7.43. This value indicates a definite evidence of the canonical values in CMB data. The Bayes factor in favour of the dipole value inferred from the quasar distribution [49] is $\sim 1.24 \times 10^{-11}$, indicating strong disagreement according to the Jeffreys' scale [105]. Similar analysis has also been carried out using `NILC` and `SEVEM`, with reasonable approximations for the effective boost factor. The values of inferred velocity and direction[16] have been found to be consistent with the ones from `SMICA`. The consistency of the Doppler boost signal presented in this work method from the small angular scale temperature data with the measured CMB dipole suggests evidence for the absence of other dipole modulation signal with amplitude higher than $\sim 10^{-3}$ at those angular scales. This is consistent with the power-law decay of the cosmic hemispherical asymmetry signal in l obtained previously [11]; and with the non-detection of directional anomalies in cosmological parameter estimates from the small scale anisotropies [190, 191].

---

[16] However, we don't put the detailed results for `NILC` and `SEVEM` due to the unavailability of their respective weights and the corresponding propagation codes in Planck Legacy Archive and IRSA websites. These are required to calculate the effective boost factor, which is essential to estimate the Doppler boost signal.

In our analysis, we have used a diagonal noise covariance matrix, computed from 200 FFP10 noise simulations. However a further improvement can be made by also including the off-diagonal terms of the covariance matrix. This will be explored in a future work using a fast covariance matrix calculation technique [98]. This Bayesian formalism can also be applied to the *Planck* polarization map to extract the Doppler boost signal [44] using the `SMICA` boost factor introduced in this analysis. The method will also be useful for the future ground-based and space-based high resolution CMB experiments such as Advanced ACTPol [192], SPT-3G [193], Simons Observatory [194], CMB-S4 [195], CMB-HD [196], CMB-Bhārat[17], and PICO [197] to infer the value of local motion [31,44,58] and also the imprints of cosmic hemispherical asymmetry [198–200] from CMB temperature and polarization anisotropy.

9.2 Clusters: Small-Scale CMB Lenses

In our work, we demonstrated the use of the maximum a posteriori CMB lensing mass map estimator to reconstruct the mass profile of galaxy clusters. We showed that the constraints on the cluster masses reach the forecasted ones on simple simulations. The MAP estimator improves the constraints on the cluster mass by 12% compared to the HDV QE [12] with joint temperature and polarization reconstruction, and by 20% from polarization only. This is due to the absence of scale cuts in temperature, and iterative reduction of the CMB fluctuations sourced by cluster and LSS lensing (in polarization predominantly).

In temperature, the MAP estimator suffers from a much smaller bias than the well-known QE bias, that arises from the misestimate of the background gradient CMB modes. This may be interpreted by the fact that the MAP iteratively estimates the delensed CMB modes, using higher order correlation functions of the CMB maps, to get more accurately the unlensed gradient. This permits usage of all CMB scales in the reconstruction, without the necessity of scale cuts as in [12] (provided, of course, that foregrounds or other contaminating signals are under control on the relevant scales).

---

[17] http://cmb-bharat.in

The MAP reconstruction used here is the exact same that is being developed for generic CMB lensing reconstruction, on wide areas of the sky. It makes no assumption on what sources the deflections, and a reconstruction on some area of the sky will reconstruct at once all cluster signals in the area in a 'optimal', statistically speaking, manner. On the practical side, the curved sky MAP implementation received recently considerable increase in speed and accuracy [184], making full-sky analyses perfectly doable in very reasonable time, and converging just as well on realistic, N-body simulations inputs. Results will be presented elsewhere.

In this first work, we used for simplicity flat-sky simulations, each time with one cluster in a small patch. Our simulations went a step further than some other analyses [171] by including the lensing from the background large scale structures together with the cluster. This increases the variance of the QE, and somewhat less for the MAP. We assumed there the background LSS lensing independent from the cluster. In reality, clusters are located at the nodes of the cosmic web, and are highly correlated with overdensity regions. More sophisticated and realistic simulations such as Websky [201] or DEMNUni [202] can be used to quantify this. We also neglected many practical issues, such as the impact of miscentering, which can degrade the constraints on the mass by about $\sim 10\%$ [135, 149]. To this and other issues independent from the mass reconstruction process such as masking, and anisotropic noise, the same techniques developed for the QEs, can be applied here as well. We also plan to test the robustness of our analysis against the choice of assumed profile in our future work.

The normalization of the MAP lensing mass map (which is analogous to a Wiener-filter) requires careful handling. Indeed, at the present time it cannot be obtained accurately analytically and we relied on a set of (cluster-free, with Gaussian input lensing fields) fiducial simulations to obtain it. We showed in [181] that this normalization is independent of the true cosmology, input lensing and data noise statistics of the CMB, hence we expect this procedure to be sufficiently robust in practice.

Much work remains to be done. We did not consider contamination from foregrounds signal, such as the SZ effect, radio point sources or the Cosmic Infrared Background. The thermal SZ (tSZ) effect has a frequency dependence which allows to remove its contribution from the observed CMB maps, at the expense of increased variance. It is possible to reduce the loss of signal in the lensing reconstruction by tSZ cleaning only the gradient leg of the QE [145–147]. The kinematic SZ (kSZ) however cannot be distinguished from the lensing signal. Efforts have been undertaken to enhance the robustness of cluster-lensing estimators against kSZ contamination [166, 203]. The rotational kSZ effect [204] is also another possible source of contamination, which will be addressed within the scope of foreground studies in our future work. However, it is expected that the polarization foregrounds are small on the relevant scales, so our MAP estimator forecast in polarization should in principle be robust.

Appendices

Appendix A

Appendix for Chapter 8

A.1 Exact QE bias calculation

In this appendix we sketch how we obtain the exact expectation value of a quadratic estimator (QE) in the presence of a fixed deflection field. This allows us to predict the mass profiles and mass bias obtained by QE mass estimates. We used a curved-sky implementation, which could certainly made much faster in a satisfactory manner using the flat-sky approximation, but we found it fit enough for purpose.

We consider a generic separable temperature QE, described by two isotropic functions F_l and G_l. Following *Planck*-lensing style notation, it may be written in configuration space,

$$\begin{aligned} {}_1\hat{g}(\hat{n}) = &\left(\sum_{l_1 m_1} F_{l_1} T_{l_1 m_1}\, {}_sY_{l_1 m_1}(\hat{n})\right) \\ &\times \left(\sum_{l_2 m_2} G_{l_1} T_{l_2 m_2}\, {}_tY_{l_2 m_2}(\hat{n})\right). \end{aligned} \tag{A.1}$$

In the case of interest, lensing from temperature-only, we have $s = 0, t = 1$, and

$$F_l = \frac{1}{C_l + N_l}, \quad G_l = -\sqrt{l(l+1)}\frac{C_l}{C_l + N_l}, \tag{A.2}$$

Here, ${}_1\hat{g}(\hat{n})$ is the unnormalized deflection vector (spin-1) field estimate. We want to evaluate this quantity

$$\langle\, {}_1\hat{g}(\hat{n})\rangle_{\text{fixed } \phi}\,, \tag{A.3}$$

which may be used to predict the result of stacking QEs from CMB maps on identical clusters.

Let $\hat{n}'$ be the undeflected position that corresponds to the observed location $\hat{n}$. Working at fixed $\hat{n}$, by Fourier transforming the T-maps, we may write this as a cross-spectrum,

$$\langle\, {}_1\hat{g}(\hat{n})\rangle_{\text{fixed }\phi} = \sum_{lm} C_l F^*_{lm}(\hat{n}) G_{lm}(\hat{n}), \tag{A.4}$$

with

$$\begin{aligned} G_{lm} &= \int d^2n_2 G(\hat{n},\hat{n}_2) Y^*_{lm}(\hat{n}'_2) \\ F_{lm} &= \int d^2n_1 F(\hat{n},\hat{n}_1) Y^*_{lm}(\hat{n}'_1). \end{aligned} \tag{A.5}$$

Here F and G have structure similar to that of a spin-weighted correlation function

$$\begin{aligned} F(\hat{n},\hat{n}_1) &= \sum_{l_1 m_1} F_{l_1}\, {}_sY_{l_1 m_1}(\hat{n})\, {}_0Y^*_{l_1 m_1}(\hat{n}_1), \\ G(\hat{n},\hat{n}_2) &= \sum_{l_2 m_2} G_{l_2}\, {}_tY_{l_2 m_2}(\hat{n})\, {}_0Y^*_{l_2 m_2}(\hat{n}_2). \end{aligned} \tag{A.6}$$

For an arbitrary deflection field, this is a tough calculation, requiring several spherical harmonics transforms on non-regular grid per each point of interest $\hat{n}$

In the case of cluster lensing things simplify quite a bit owing to

- spherical symmetry, $\langle g(\hat{n})\rangle_{\text{fixed deflection}}$ will depend on the co-latitude θ only, and the deflection field does not change the longitude coordinates,
- and the fact that clusters are small. With the coordinates such that the cluster lies at the pole, only a small number of m's will be necessary. The circle at latitude θ has length $\sin\theta$, hence there is an effective $m_{\max} \sim l_{\max}\sin\theta \sim 5$ for $\theta \sim 10'$ and an analysis with $l_{\max} = 5000$. Since it is spin-1, $\langle {}_1g(\theta)\rangle$ will be heavily dominated by the $m = 1$ component near the pole.

We use this to perform the calculation in Eq. (A.3) by brute force, using the efficient general spherical harmonic transforms of [184].

Bibliography

[1] J.C. Mather, E.S. Cheng, J. Eplee, R. E., R.B. Isaacman, S.S. Meyer, R.A. Shafer et al., *A Preliminary Measurement of the Cosmic Microwave Background Spectrum by the Cosmic Background Explorer (COBE) Satellite*, *Astrophys. J. Lett.* **354** (1990) L37.

[2] C.L. Bennett, D. Larson, J.L. Weiland, N. Jarosik, G. Hinshaw, N. Odegard et al., *Nine-year Wilkinson Microwave Anisotropy Probe (WMAP) Observations: Final Maps and Results*, .

[3] Planck collaboration, *Planck 2018 results. I. Overview and the cosmological legacy of Planck*, *Astron. Astrophys.* **641** (2020) A1 [`1807.06205`].

[4] Planck collaboration, *Planck 2018 results. VIII. Gravitational lensing*, *Astron. Astrophys.* **641** (2020) A8 [`1807.06210`].

[5] ACT collaboration, *The Atacama Cosmology Telescope: DR6 Gravitational Lensing Map and Cosmological Parameters*, `2304.05203`.

[6] SPT collaboration, *Measurement of gravitational lensing of the cosmic microwave background using SPT-3G 2018 data*, *Phys. Rev. D* **108** (2023) 122005 [`2308.11608`].

[7] ACT collaboration, *The Atacama Cosmology Telescope: A Measurement of the DR6 CMB Lensing Power Spectrum and its Implications for Structure Growth*, `2304.05202`.

[8] J. Carron, M. Mirmelstein and A. Lewis, *CMB lensing from Planck PR4 maps*, *JCAP* **09** (2022) 039 [`2206.07773`].

[9] S. Mukherjee and T. Souradeep, *Statistically anisotropic Gaussian simulations of the CMB temperature field*, *Phys. Rev. D* **89** (2014) 063013 [`1311.5837`].

[10] Planck collaboration, *Planck 2018 results. IV. Diffuse component separation*, *Astron. Astrophys.* **641** (2020) A4 [`1807.06208`].

[11] S. Shaikh, S. Mukherjee, S. Das, B.D. Wandelt and T. Souradeep, *Joint Bayesian Analysis of Large Angular Scale CMB Temperature Anomalies*, *JCAP* **08** (2019) 007 [`1902.10155`].

[12] W. Hu, S. DeDeo and C. Vale, *Cluster Mass Estimators from CMB Temperature and Polarization Lensing*, *New J. Phys.* **9** (2007) 441 [`astro-ph/0701276`].

[13] A.A. Penzias and R.W. Wilson, *A Measurement of Excess Antenna Temperature at 4080 Mc/s.*, *Astrophys. J.* **142** (1965) 419.

[14] R.H. Dicke, P.J.E. Peebles, P.G. Roll and D.T. Wilkinson, *Cosmic Black-Body Radiation.*, *Astrophys. J.* **142** (1965) 414.

[15] N.W. Boggess, J.C. Mather, R. Weiss, C.L. Bennett, E.S. Cheng, E. Dwek et al., *The COBE Mission: Its Design and Performance Two Years after Launch*, *Astrophys. J.* **397** (1992) 420.

[16] A. Kogut, C. Lineweaver, G.F. Smoot, C.L. Bennett, A. Banday, N.W. Boggess et al., *Dipole Anisotropy in the COBE Differential Microwave Radiometers First-Year Sky Maps*, *Astrophys. J.* **419** (1993) 1 [`astro-ph/9312056`].

[17] D.J. Fixsen, *The temperature of the cosmic microwave background*, *The Astrophysical Journal* **707** (2009) 916–920.

[18] G. Smoot, C. Bennett, R. Weber, J. Maruschak, R. Ratliff, M. Janssen et al., *COBE Differential Microwave Radiometers: Instrument Design and Implementation*, *Astrophys. J.* **360** (1990) 685.

[19] A. Kogut et al., *Dipole anisotropy in the COBE DMR first year sky maps*, *Astrophys. J.* **419** (1993) 1 [`astro-ph/9312056`].

[20] M. Zaldarriaga and U. Seljak, *An all sky analysis of polarization in the microwave background*, *Phys. Rev. D* **55** (1997) 1830 [`astro-ph/9609170`].

[21] M. Kamionkowski, A. Kosowsky and A. Stebbins, *Statistics of cosmic microwave background polarization*, *Phys. Rev. D* **55** (1997) 7368 [`astro-ph/9611125`].

[22] J.M. Fowler et al., *Optical Design of the Atacama Cosmology Telescope and the Millimeter Bolometric Array Camera*, *Appl. Opt.* **46** (2007) 3444 [`astro-ph/0701020`].

[23] J.E. Carlstrom, P.A.R. Ade, K.A. Aird, B.A. Benson, L.E. Bleem, S. Busetti et al., *The 10 Meter South Pole Telescope*, *Publications of the Astronomical Society of the Pacific* **123** (2011) 568 [`0907.4445`].

[24] BICEP collaboration, *BICEP: a cosmic microwave background polarization telescope at the South Pole*, *Highlights Astron.* **15** (2010) 618.

[25] POLARBEAR collaboration, *Measurement of the Cosmic Microwave Background Polarization Lensing Power Spectrum with the POLARBEAR experiment*, *Phys. Rev. Lett.* **113** (2014) 021301 [`1312.6646`].

[26] SIMONS OBSERVATORY collaboration, *The Simons Observatory: Science goals and forecasts*, *JCAP* **02** (2019) 056 [`1808.07445`].

[27] S. Ghosh et al., *Performance forecasts for the primordial gravitational wave detection pipelines for AliCPT-1*, *JCAP* **10** (2022) 063 [`2205.14804`].

[28] CMB-S4 collaboration, *CMB-S4 Science Book, First Edition*, 10, 2016 [`1610.02743`].

[29] LiteBIRD collaboration, *Probing Cosmic Inflation with the LiteBIRD Cosmic Microwave Background Polarization Survey*, *PTEP* **2023** (2023) 042F01 [2202.02773].

[30] A. Lewis and A. Challinor, *Weak gravitational lensing of the CMB*, *Phys. Rept.* **429** (2006) 1 [astro-ph/0601594].

[31] A. Challinor and F. van Leeuwen, *Peculiar velocity effects in high resolution microwave background experiments*, *Phys. Rev. D* **65** (2002) 103001 [astro-ph/0112457].

[32] H.K. Eriksen, F.K. Hansen, A.J. Banday, K.M. Gorski and P.B. Lilje, *Asymmetries in the Cosmic Microwave Background anisotropy field*, *Astrophys. J.* **605** (2004) 14 [astro-ph/0307507].

[33] A. Hajian and T. Souradeep, *The Cosmic microwave background bipolar power spectrum: Basic formalism and applications*, astro-ph/0501001.

[34] S. Mitra, A.S. Sengupta, S. Ray, R. Saha and T. Souradeep, *CMB power spectrum estimation with non-circular beam and incomplete sky coverage*, *Mon. Not. Roy. Astron. Soc.* **394** (2009) 1419 [astro-ph/0702100].

[35] D.A. Varshalovich, A.N. Moskalev and V.K. Khersonskii, *Quantum theory of angular momentum*, .

[36] W. Hu and T. Okamoto, *Mass reconstruction with cmb polarization*, *Astrophys. J.* **574** (2002) 566 [astro-ph/0111606].

[37] T. Okamoto and W. Hu, *CMB lensing reconstruction on the full sky*, *Phys. Rev. D* **67** (2003) 083002 [astro-ph/0301031].

[38] J. Carron and A. Lewis, *Maximum a posteriori CMB lensing reconstruction*, *Phys. Rev. D* **96** (2017) 063510 [1704.08230].

[39] D.J. Fixsen, E.S. Cheng, D.A. Cottingham, J. Eplee, R. E., R.B. Isaacman, J.C. Mather et al., *Cosmic Microwave Background Dipole Spectrum Measured by the COBE FIRAS Instrument*, *Astrophys. J.* **420** (1994) 445.

[40] C.H. Lineweaver, L. Tenorio, G.F. Smoot, P. Keegstra, A.J. Banday and P. Lubin, *The dipole observed in the COBE DMR four-year data*, *Astrophys. J.* **470** (1996) 38 [astro-ph/9601151].

[41] D.J. Fixsen, E.S. Cheng, J.M. Gales, J.C. Mather, R.A. Shafer and E.L. Wright, *The Cosmic Microwave Background Spectrum from the Full COBE FIRAS Data Set*, *Astrophys. J.* **473** (1996) 576 [astro-ph/9605054].

[42] G. Hinshaw, J.L. Weiland, R.S. Hill, N. Odegard, D. Larson, C.L. Bennett et al., *Five-year wilkinson microwave anisotropy probe observations: Data processing, sky maps, and basic results*, *The Astrophysical Journal Supplement Series* **180** (2009) 225–245.

[43] M. Kamionkowski and L. Knox, *Aspects of the cosmic microwave background dipole*, *Phys. Rev. D* **67** (2003) 063001 [astro-ph/0210165].

[44] S. Mukherjee, A. De and T. Souradeep, *Statistical isotropy violation of CMB Polarization sky due to Lorentz boost*, *Phys. Rev. D* **89** (2014) 083005 [`1309.3800`].

[45] A. Hajian and T. Souradeep, *Measuring the statistical isotropy of the cosmic microwave background anisotropy*, *The Astrophysical Journal* **597** (2003) L5–L8.

[46] T. Souradeep, A. Hajian and S. Basak, *Measuring statistical isotropy of cmb anisotropy*, *New Astronomy Reviews* **50** (2006) 889–895.

[47] C. Blake and J. Wall, *Detection of the velocity dipole in the radio galaxies of the nrao vla sky survey*, *Nature* **416** (2002) 150 [`astro-ph/0203385`].

[48] M. Rubart and D.J. Schwarz, *Cosmic radio dipole from NVSS and WENSS*, *Astron. Astrophys.* **555** (2013) A117 [`1301.5559`].

[49] N.J. Secrest, S. von Hausegger, M. Rameez, R. Mohayaee, S. Sarkar and J. Colin, *A Test of the Cosmological Principle with Quasars*, *Astrophys. J. Lett.* **908** (2021) L51 [`2009.14826`].

[50] F. Crawford, *Detecting the Cosmic Dipole Anisotropy in Large-Scale Radio Surveys*, *Astrophys. J.* **692** (2009) 887 [`0810.4520`].

[51] N. Pant, A. Rotti, C.A.P. Bengaly and R. Maartens, *Measuring our velocity from fluctuations in number counts*, *JCAP* **03** (2019) 023 [`1808.09743`].

[52] C.A.P. Bengaly, T.M. Siewert, D.J. Schwarz and R. Maartens, *Testing the standard model of cosmology with the SKA: the cosmic radio dipole*, *Mon. Not. Roy. Astron. Soc.* **486** (2019) 1350 [`1810.04960`].

[53] T. Nadolny, R. Durrer, M. Kunz and H. Padmanabhan, *A new test of the Cosmological Principle: measuring our peculiar velocity and the large scale anisotropy independently*, `2106.05284`.

[54] R.A. Sunyaev and Y.B. Zeldovich, *The interaction of matter and radiation in the hot model of the Universe, II*, *Astrophys Space Sci* **07** (1970) 20.

[55] J. Chluba, G. Hutsi and R.A. Sunyaev, *Clusters of galaxies in the microwave band: Influence of the motion of the solar system*, *Astron. Astrophys.* **434** (2005) 811 [`astro-ph/0409058`].

[56] Planck collaboration, *Planck intermediate results. LVI. Detection of the CMB dipole through modulation of the thermal Sunyaev-Zeldovich effect: Eppur si muove II*, *Astron. Astrophys.* **644** (2020) A100 [`2003.12646`].

[57] A. Kosowsky and T. Kahniashvili, *Signature of local motion in the microwave sky*, *Phys. Rev. Lett.* **106** (2011) 191301.

[58] L. Amendola, R. Catena, I. Masina, A. Notari, M. Quartin and C. Quercellini, *Measuring our peculiar velocity on the CMB with high-multipole off-diagonal correlations*, *JCAP* **07** (2011) 027 [`1008.1183`].

[59] Planck collaboration, *Planck 2013 results. XXVII. Doppler boosting of the CMB: Eppur si muove*, *Astron. Astrophys.* **571** (2014) A27 [`1303.5087`].

[60] D. Hanson and A. Lewis, *Estimators for CMB statistical anisotropy*, *Phys. Rev. D* **80** (2009) 063004 [0908.0963].

[61] S. Adhikari, *Local variance asymmetries in Planck temperature anisotropy maps*, *Mon. Not. Roy. Astron. Soc.* **446** (2015) 4232 [1408.5396].

[62] P.K. Aluri, N. Pant, A. Rotti and T. Souradeep, *Novel approach to reconstructing signals of isotropy violation from a masked CMB sky*, *Phys. Rev. D* **92** (2015) 083015 [1506.00550].

[63] R. Catena and A. Notari, *Cosmological parameter estimation: impact of CMB aberration*, *JCAP* **04** (2013) 028 [1210.2731].

[64] D. Jeong, J. Chluba, L. Dai, M. Kamionkowski and X. Wang, *Effect of aberration on partial-sky measurements of the cosmic microwave background temperature power spectrum*, *Physical Review D* **89** (2014) .

[65] S. Yasini and E. Pierpaoli, *Footprints of Doppler and aberration effects in cosmic microwave background experiments: statistical and cosmological implications*, *Mon. Not. Roy. Astron. Soc.* **493** (2020) 1708 [1910.04315].

[66] O. Roldan, A. Notari and M. Quartin, *Interpreting the CMB aberration and Doppler measurements: boost or intrinsic dipole?*, *JCAP* **06** (2016) 026 [1603.02664].

[67] P.D. Meerburg, J. Meyers and A. van Engelen, *Reconstructing the Primary CMB Dipole*, *Phys. Rev. D* **96** (2017) 083519 [1704.00718].

[68] P.d.S. Ferreira and M. Quartin, *First constraints on the intrinsic CMB dipole and our velocity with Doppler and aberration*, 2011.08385.

[69] P. Naselsky, W. Zhao, J. Kim and S. Chen, *Is the CMB asymmetry due to the kinematic dipole?*, *Astrophys. J.* **749** (2012) 31 [1108.4376].

[70] W. Zhao, *Directional dependence of CMB parity asymmetry*, *Phys. Rev. D* **89** (2014) 023010 [1306.0955].

[71] J. Delabrouille, J.F. Cardoso and G. Patanchon, *Multi-detector multi-component spectral matching and applications for CMB data analysis*, *Mon. Not. Roy. Astron. Soc.* **346** (2003) 1089 [astro-ph/0211504].

[72] J.-F. Cardoso, M. Le Jeune, J. Delabrouille, M. Betoule and G. Patanchon, *Component separation with flexible models—application to multichannel astrophysical observations*, *IEEE Journal of Selected Topics in Signal Processing* **2** (2008) 735.

[73] Planck collaboration, *Planck 2018 results. IV. Diffuse component separation*, *Astron. Astrophys.* **641** (2020) A4 [1807.06208].

[74] J. Chluba, *Fast and accurate computation of the aberration kernel for the cosmic microwave background sky*, *Mon. Not. Roy. Astron. Soc.* **415** (2011) 3227 [1102.3415].

[75] A. Yoho, C.J. Copi, G.D. Starkman and T.S. Pereira, *Real-space approach to cosmic microwave background deboosting*, *Mon. Not. Roy. Astron. Soc.* **432** (2013) 2208 [`1211.6756`].

[76] Planck collaboration, *Planck 2015 results. XII. Full Focal Plane simulations*, *Astron. Astrophys.* **594** (2016) A12 [`1509.06348`].

[77] Planck collaboration, *Planck 2018 results. I. Overview and the cosmological legacy of Planck*, *Astron. Astrophys.* **641** (2020) A1 [`1807.06205`].

[78] D.A. Varshalovich, A.N. Moskalev and V.K. Khersonskii, *Quantum Theory of Angular Momentum*, World Scientific, Singapore (1988).

[79] Planck collaboration, *Planck 2013 results. XXVII. Doppler boosting of the CMB: Eppur si muove*, *Astron. Astrophys.* **571** (2014) A27 [`1303.5087`].

[80] S. Duane, A.D. Kennedy, B.J. Pendleton and D. Roweth, *Hybrid Monte Carlo*, *Phys. Lett.* **B195** (1987) 216.

[81] S. Das, B.D. Wandelt and T. Souradeep, *Bayesian inference on the sphere beyond statistical isotropy*, *JCAP* **1510** (2015) 050 [`1509.07137`].

[82] Planck collaboration, *Planck 2018 results. III. High Frequency Instrument data processing and frequency maps*, *Astron. Astrophys.* **641** (2020) A3 [`1807.06207`].

[83] Planck collaboration, *Planck 2013 results. XXIII. Isotropy and statistics of the CMB*, *Astron. Astrophys.* **571** (2014) A23 [`1303.5083`].

[84] Planck collaboration, *Planck 2015 results. XVI. Isotropy and statistics of the CMB*, *Astron. Astrophys.* **594** (2016) A16 [`1506.07135`].

[85] Planck collaboration, *Planck 2018 results. VII. Isotropy and Statistics of the CMB*, *Astron. Astrophys.* **641** (2020) A7 [`1906.02552`].

[86] Planck collaboration, *Planck 2018 results. IX. Constraints on primordial non-Gaussianity*, *Astron. Astrophys.* **641** (2020) A9 [`1905.05697`].

[87] R. Trotta, *Bayes in the sky: Bayesian inference and model selection in cosmology*, *Contemp. Phys.* **49** (2008) 71 [`0803.4089`].

[88] R. Neal, *MCMC Using Hamiltonian Dynamics*, in *Handbook of Markov Chain Monte Carlo*, pp. 113–162 (2011), DOI.

[89] J. Hoftuft, H.K. Eriksen, A.J. Banday, K.M. Górski, F.K. Hansen and P.B. Lilje, *Increasing evidence for hemispherical power asymmetry in the five-yearwmapdata*, *The Astrophysical Journal* **699** (2009) 985–989.

[90] A. Hajian, *Efficient Cosmological Parameter Estimation with Hamiltonian Monte Carlo*, *Phys. Rev.* **D75** (2007) 083525 [`astro-ph/0608679`].

[91] J.F. Taylor, M.A.J. Ashdown and M.P. Hobson, *Fast optimal CMB power spectrum estimation with Hamiltonian sampling*, *Mon. Not. Roy. Astron. Soc.* **389** (2008) 1284 [`0708.2989`].

[92] J. Jasche and F.S. Kitaura, *Fast hamiltonian sampling for large-scale structure inference*, *Monthly Notices of the Royal Astronomical Society* **407** (2010) 29–42.

[93] J. Jasche and B.D. Wandelt, *Bayesian physical reconstruction of initial conditions from large-scale structure surveys*, *Monthly Notices of the Royal Astronomical Society* **432** (2013) 894–913.

[94] J. Jasche and B.D. Wandelt, *Methods for Bayesian power spectrum inference with galaxy surveys*, *Astrophys. J.* **779** (2013) 15 [`1306.1821`].

[95] E. Anderes, B. Wandelt and G. Lavaux, *Bayesian inference of CMB gravitational lensing*, *Astrophys. J.* **808** (2015) 152 [`1412.4079`].

[96] M. Millea, E. Anderes and B.D. Wandelt, *Bayesian delensing delight: sampling-based inference of the primordial CMB and gravitational lensing*, *Phys. Rev. D* **102** (2020) 123542 [`2002.00965`].

[97] K.M. Gorski, E. Hivon, A.J. Banday, B.D. Wandelt, F.K. Hansen, M. Reinecke et al., *HEALPix - A Framework for high resolution discretization, and fast analysis of data distributed on the sphere*, *Astrophys. J.* **622** (2005) 759 [`astro-ph/0409513`].

[98] D.K. Ramanah, G. Lavaux and B.D. Wandelt, *Wiener filtering and pure $\mathcal{E}/\mathcal{B}$ decomposition of CMB maps with anisotropic correlated noise*, *Mon. Not. Roy. Astron. Soc.* **490** (2019) 947 [`1906.10704`].

[99] Planck collaboration, *Planck 2018 results. V. CMB power spectra and likelihoods*, *Astron. Astrophys.* **641** (2020) A5 [`1907.12875`].

[100] B.D. Wandelt, D.L. Larson and A. Lakshminarayanan, *Global, exact cosmic microwave background data analysis using Gibbs sampling*, *Phys. Rev. D* **70** (2004) 083511 [`astro-ph/0310080`].

[101] D.L. Larson, H.K. Eriksen, B.D. Wandelt, K.M. Gorski, G. Huey, J.B. Jewell et al., *Estimation of Polarized Power Spectra by Gibbs sampling*, *Astrophys. J.* **656** (2007) 653 [`astro-ph/0608007`].

[102] P. Virtanen, R. Gommers, T.E. Oliphant, M. Haberland, T. Reddy, D. Cournapeau et al., *SciPy 1.0: Fundamental Algorithms for Scientific Computing in Python*, *Nature Methods* **17** (2020) 261.

[103] Planck collaboration, *Planck 2013 results. XV. CMB power spectra and likelihood*, *Astron. Astrophys.* **571** (2014) A15 [`1303.5075`].

[104] Planck collaboration, *Planck 2015 results. XI. CMB power spectra, likelihoods, and robustness of parameters*, *Astron. Astrophys.* **594** (2016) A11 [`1507.02704`].

[105] H. Jeffreys, *The Theory of Probability* (1939).

[106] R.E. Kass and A.E. Raftery, *Bayes Factors*, *J. Am. Statist. Assoc.* **90** (1995) 773.

[107] R.D. Morey, J.-W. Romeijn and J.N. Rouder, *The philosophy of bayes factors and the quantification of statistical evidence*, *Journal of Mathematical Psychology* **72** (2016) 6.

[108] J.M. Dickey, *The Weighted Likelihood Ratio, Linear Hypotheses on Normal Location Parameters*, *The Annals of Mathematical Statistics* **42** (1971) 204 .

[109] P.R.M. Eisenhardt, F. Marocco, J.W. Fowler, A.M. Meisner, J.D. Kirkpatrick, N. Garcia et al., *The catwise preliminary catalog: Motions from wise and neowise data*, *The Astrophysical Journal Supplement Series* **247** (2020) 69.

[110] E.L. Wright, P.R.M. Eisenhardt, A.K. Mainzer, M.E. Ressler, R.M. Cutri, T. Jarrett et al., *The wide-field infrared survey explorer (wise): Mission description and initial on-orbit performance*, *The Astronomical Journal* **140** (2010) 1868–1881.

[111] A.M. Meisner, D. Lang and D.J. Schlegel, *Another unWISE Update: The Deepest Ever Full-sky Maps at 3-5 μm*, *Research Notes of the American Astronomical Society* **2** (2018) 1 [`1801.03566`].

[112] "Private communication with Subir Sarkar, an author of [49]."

[113] A. Vikhlinin et al., *Chandra Cluster Cosmology Project III: Cosmological Parameter Constraints*, *Astrophys. J.* **692** (2009) 1060 [`0812.2720`].

[114] N. Sehgal et al., *The Atacama Cosmology Telescope: Cosmology from Galaxy Clusters Detected via the Sunyaev-Zel'dovich Effect*, *Astrophys. J.* **732** (2011) 44 [`1010.1025`].

[115] S.W. Allen, A.E. Evrard and A.B. Mantz, *Cosmological Parameters from Observations of Galaxy Clusters*, *Ann. Rev. Astron. Astrophys.* **49** (2011) 409 [`1103.4829`].

[116] Planck collaboration, *Planck 2013 results. XX. Cosmology from Sunyaev–Zeldovich cluster counts*, *Astron. Astrophys.* **571** (2014) A20 [`1303.5080`].

[117] A.B. Mantz, S.W. Allen, R.G. Morris, D.A. Rapetti, D.E. Applegate, P.L. Kelly et al., *Cosmology and astrophysics from relaxed galaxy clusters – II. Cosmological constraints*, *Mon. Not. Roy. Astron. Soc.* **440** (2014) 2077 [`1402.6212`].

[118] A.B. Mantz et al., *Weighing the giants – IV. Cosmology and neutrino mass*, *Mon. Not. Roy. Astron. Soc.* **446** (2015) 2205 [`1407.4516`].

[119] Planck collaboration, *Planck 2015 results. XXIV. Cosmology from Sunyaev-Zeldovich cluster counts*, *Astron. Astrophys.* **594** (2016) A24 [`1502.01597`].

[120] SPT collaboration, *Cosmological Constraints from Galaxy Clusters in the 2500 square-degree SPT-SZ Survey*, *Astrophys. J.* **832** (2016) 95 [`1603.06522`].

[121] SPT collaboration, *Cluster Cosmology Constraints from the 2500 deg^2 SPT-SZ Survey: Inclusion of Weak Gravitational Lensing Data from Magellan and the Hubble Space Telescope*, *Astrophys. J.* **878** (2019) 55 [`1812.01679`].

[122] SPT collaboration, *Improving Cosmological Constraints from Galaxy Cluster Number Counts with CMB-cluster-lensing Data: Results from the SPT-SZ Survey and Forecasts for the Future*, Astrophys. J. **931** (2022) 139 [2111.07491].

[123] S. Raghunathan, N. Whitehorn, M.A. Alvarez, H. Aung, N. Battaglia, G.P. Holder et al., *Constraining Cluster Virialization Mechanism and Cosmology Using Thermal-SZ-selected Clusters from Future CMB Surveys*, Astrophys. J. **926** (2022) 172 [2107.10250].

[124] B.P. Koester, T.A. McKay, J. Annis, R.H. Wechsler, A.E. Evrard, E. Rozo et al., *MaxBCG: A Red Sequence Galaxy Cluster Finder*, Astrophys. J. **660** (2007) 221 [astro-ph/0701268].

[125] DES collaboration, *Constraints on the richness–mass relation and the optical-SZE positional offset distribution for SZE-selected clusters*, Mon. Not. Roy. Astron. Soc. **454** (2015) 2305 [1506.07814].

[126] S. Andreon, *Richness-based masses of rich and famous galaxy clusters*, Astron. Astrophys. **587** (2016) A158 [1601.06912].

[127] A. Farahi, A.E. Evrard, E. Rozo, E.S. Rykoff and R.H. Wechsler, *Galaxy Cluster Mass Estimation from Stacked Spectroscopic Analysis*, Mon. Not. Roy. Astron. Soc. **460** (2016) 3900 [1601.05773].

[128] M. Simet, T. McClintock, R. Mandelbaum, E. Rozo, E. Rykoff, E. Sheldon et al., *Weak lensing measurement of the mass–richness relation of SDSS redMaPPer clusters*, Mon. Not. Roy. Astron. Soc. **466** (2017) 3103 [1603.06953].

[129] M. Arnaud, E. Pointecouteau and G.W. Pratt, *The Structural and scaling properties of nearby galaxy clusters. 2. The M-T relation*, Astron. Astrophys. **441** (2005) 893 [astro-ph/0502210].

[130] M. Arnaud, E. Pointecouteau and G.W. Pratt, *Calibration of the galaxy cluster M_500-Y_X relation with XMM-Newton*, Astron. Astrophys. **474** (2007) L37 [0709.1561].

[131] K. Vanderlinde et al., *Galaxy Clusters Selected with the Sunyaev-Zel'dovich Effect from 2008 South Pole Telescope Observations*, Astrophys. J. **722** (2010) 1180 [1003.0003].

[132] G.W. Pratt, M. Arnaud, A. Biviano, D. Eckert, S. Ettori, D. Nagai et al., *The galaxy cluster mass scale and its impact on cosmological constraints from the cluster population*, Space Sci. Rev. **215** (2019) 25 [1902.10837].

[133] L. Salvati, M. Douspis and N. Aghanim, *Impact of systematics on cosmological parameters from future galaxy cluster surveys*, Astron. Astrophys. **643** (2020) A20 [2005.10204].

[134] L. Salvati et al., *Combining Planck and SPT Cluster Catalogs: Cosmological Analysis and Impact on the Planck Scaling Relation Calibration*, Astrophys. J. **934** (2022) 129 [2112.03606].

[135] M.S. Madhavacheril, N. Battaglia and H. Miyatake, *Fundamental physics from future weak-lensing calibrated Sunyaev-Zel'dovich galaxy cluster counts*, *Phys. Rev. D* **96** (2017) 103525 [`1708.07502`].

[136] A. von der Linden et al., *Robust Weak-lensing Mass Calibration of Planck Galaxy Clusters*, *Mon. Not. Roy. Astron. Soc.* **443** (2014) 1973 [`1402.2670`].

[137] H. Hoekstra, R. Herbonnet, A. Muzzin, A. Babul, A. Mahdavi, M. Viola et al., *The Canadian Cluster Comparison Project: detailed study of systematics and updated weak lensing masses*, *Mon. Not. Roy. Astron. Soc.* **449** (2015) 685 [`1502.01883`].

[138] G.P. Smith et al., *LoCuSS: Testing hydrostatic equilibrium in galaxy clusters*, *Mon. Not. Roy. Astron. Soc.* **456** (2016) L74 [`1511.01919`].

[139] M. Sereno, G. Covone, L. Izzo, S. Ettori, J. Coupon and M. Lieu, *PSZ2LenS. Weak lensing analysis of the Planck clusters in the CFHTLenS and in the RCSLenS*, *Mon. Not. Roy. Astron. Soc.* **472** (2017) 1946 [`1703.06886`].

[140] M. Penna-Lima, J.G. Bartlett, E. Rozo, J.B. Melin, J. Merten, A.E. Evrard et al., *Calibrating the Planck Cluster Mass Scale with CLASH*, *Astron. Astrophys.* **604** (2017) A89 [`1608.05356`].

[141] F. Bellagamba et al., *AMICO galaxy clusters in KiDS-DR3: weak-lensing mass calibration*, *Mon. Not. Roy. Astron. Soc.* **484** (2019) 1598 [`1810.02827`].

[142] H. Miyatake et al., *Weak-lensing Mass Calibration of ACTPol Sunyaev–Zel'dovich Clusters with the Hyper Suprime-Cam Survey*, *Astrophys. J.* **875** (2019) 63 [`1804.05873`].

[143] K. Umetsu, *Cluster–galaxy weak lensing*, *Astron. Astrophys. Rev.* **28** (2020) 7 [`2007.00506`].

[144] M.R. Becker and A.V. Kravtsov, *On the Accuracy of Weak Lensing Cluster Mass Reconstructions*, *Astrophys. J.* **740** (2011) 25 [`1011.1681`].

[145] M.S. Madhavacheril and J.C. Hill, *Mitigating Foreground Biases in CMB Lensing Reconstruction Using Cleaned Gradients*, *Phys. Rev. D* **98** (2018) 023534 [`1802.08230`].

[146] DES collaboration, *Mass Calibration of Optically Selected DES clusters using a Measurement of CMB-Cluster Lensing with SPTpol Data*, *Astrophys. J.* **872** (2019) 170 [`1810.10998`].

[147] S. Patil, S. Raghunathan and C.L. Reichardt, *Suppressing the thermal sz-induced variance in cmb-cluster lensing estimators*, *The Astrophysical Journal* **888** (2019) 9.

[148] J.F. Navarro, C.S. Frenk and S.D.M. White, *The Structure of cold dark matter halos*, *Astrophys. J.* **462** (1996) 563 [`astro-ph/9508025`].

[149] I.n. Zubeldia and A. Challinor, *Cosmological constraints from Planck galaxy clusters with CMB lensing mass bias calibration*, *Mon. Not. Roy. Astron. Soc.* **489** (2019) 401 [`1904.07887`].

[150] M. Oguri and M. Takada, *Combining cluster observables and stacked weak lensing to probe dark energy: Self-calibration of systematic uncertainties*, *Physical Review D* **83** (2011) .

[151] A.R. Duffy, J. Schaye, S.T. Kay and C. Dalla Vecchia, *Dark matter halo concentrations in the Wilkinson Microwave Anisotropy Probe year 5 cosmology*, *Mon. Not. Roy. Astron. Soc.* **390** (2008) L64 [`0804.2486`].

[152] J.E. Geach and J.A. Peacock, *Cluster richness–mass calibration with cosmic microwave background lensing*, *Nature Astron.* **1** (2017) 795 [`1707.09369`].

[153] C.O. Wright and T.G. Brainerd, *Gravitational lensing by nfw halos*, `astro-ph/9908213`.

[154] M. Takada and B. Jain, *The Three - point correlation function in cosmology*, *Mon. Not. Roy. Astron. Soc.* **340** (2003) 580 [`astro-ph/0209167`].

[155] U. Seljak and M. Zaldarriaga, *Lensing induced cluster signatures in cosmic microwave background*, *Astrophys. J.* **538** (2000) 57 [`astro-ph/9907254`].

[156] R. Scoccimarro, R.K. Sheth, L. Hui and B. Jain, *How many galaxies fit in a halo? Constraints on galaxy formation efficiency from spatial clustering*, *Astrophys. J.* **546** (2001) 20 [`astro-ph/0006319`].

[157] M. Oguri and M. Takada, *Combining cluster observables and stacked weak lensing to probe dark energy: Self-calibration of systematic uncertainties*, *Phys. Rev. D* **83** (2011) 023008 [`1010.0744`].

[158] W. Hu, *Mapping the dark matter through the cmb damping tail*, *Astrophys. J. Lett.* **557** (2001) L79 [`astro-ph/0105424`].

[159] M. Maturi, M. Bartelmann, M. Meneghetti and L. Moscardini, *Gravitational lensing of the CMB by galaxy clusters*, *Astron. Astrophys.* **436** (2005) 37 [`astro-ph/0408064`].

[160] DES, SPT collaboration, *A measurement of CMB cluster lensing with SPT and DES year 1 data*, *Mon. Not. Roy. Astron. Soc.* **476** (2018) 2674 [`1708.01360`].

[161] ACT collaboration, *The Atacama Cosmology Telescope: Weighing Distant Clusters with the Most Ancient Light*, *Astrophys. J. Lett.* **903** (2020) L13 [`2009.07772`].

[162] J.-B. Melin and J.G. Bartlett, *Measuring cluster masses with CMB lensing: a statistical approach*, *Astron. Astrophys.* **578** (2015) A21 [`1408.5633`].

[163] T. Louis and D. Alonso, *Calibrating Cluster Number Counts with CMB lensing*, *Phys. Rev. D* **95** (2017) 043517 [`1609.03997`].

[164] I.n. Zubeldia and A. Challinor, *Quantifying the statistics of CMB-lensing-derived galaxy cluster mass measurements with simulations*, *Mon. Not. Roy. Astron. Soc.* **497** (2020) 5326 [2005.14607].

[165] SPT, DES collaboration, *Detection of CMB-Cluster Lensing using Polarization Data from SPTpol*, *Phys. Rev. Lett.* **123** (2019) 181301 [1907.08605].

[166] K. Levy, S. Raghunathan and K. Basu, *A Foreground-Immune CMB-Cluster Lensing Estimator*, 5, 2023 [2305.06326].

[167] B. Horowitz, S. Ferraro and B.D. Sherwin, *Reconstructing Small Scale Lenses from the Cosmic Microwave Background Temperature Fluctuations*, *Mon. Not. Roy. Astron. Soc.* **485** (2019) 3919 [1710.10236].

[168] B. Hadzhiyska, B.D. Sherwin, M. Madhavacheril and S. Ferraro, *Improving Small-Scale CMB Lensing Reconstruction*, *Phys. Rev. D* **100** (2019) 023547 [1905.04217].

[169] A. Lewis and L. King, *Cluster masses from cmb and galaxy weak lensing*, *Phys. Rev. D* **73** (2006) 063006 [astro-ph/0512104].

[170] E.J. Baxter et al., *A Measurement of Gravitational Lensing of the Cosmic Microwave Background by Galaxy Clusters Using Data from the South Pole Telescope*, *Astrophys. J.* **806** (2015) 247 [1412.7521].

[171] S. Raghunathan, S. Patil, E.J. Baxter, F. Bianchini, L.E. Bleem, T.M. Crawford et al., *Measuring galaxy cluster masses with CMB lensing using a Maximum Likelihood estimator: Statistical and systematic error budgets for future experiments*, *JCAP* **08** (2017) 030 [1705.00411].

[172] J.a. Caldeira, W.L.K. Wu, B. Nord, C. Avestruz, S. Trivedi and K.T. Story, *DeepCMB: Lensing Reconstruction of the Cosmic Microwave Background with Deep Neural Networks*, *Astron. Comput.* **28** (2019) 100307 [1810.01483].

[173] N. Gupta and C.L. Reichardt, *Mass Estimation of Galaxy Clusters with Deep Learning II. Cosmic Microwave Background Cluster Lensing*, *Astrophys. J.* **923** (2021) 96 [2005.13985].

[174] L. Parker, D. Han, P.L. Portela and S. Ho, *Recovering Galaxy Cluster Convergence from Lensed CMB with Generative Adversarial Networks*, 11, 2022 [2211.08990].

[175] C.M. Hirata and U. Seljak, *Analyzing weak lensing of the cosmic microwave background using the likelihood function*, *Phys. Rev. D* **67** (2003) 043001 [astro-ph/0209489].

[176] C.M. Hirata and U. Seljak, *Reconstruction of lensing from the cosmic microwave background polarization*, *Phys. Rev. D* **68** (2003) 083002 [astro-ph/0306354].

[177] J. Yoo and M. Zaldarriaga, *Improved estimation of cluster mass profiles from the cosmic microwave background*, *Phys. Rev. D* **78** (2008) 083002 [0805.2155].

[178] J. Yoo, M. Zaldarriaga and L. Hernquist, *Lensing reconstruction of cluster-mass cross-correlation with cosmic microwave background polarization*, *Phys. Rev. D* **81** (2010) 123006 [1005.0847].

[179] M. Millea, E. Anderes and B.D. Wandelt, *Bayesian delensing of CMB temperature and polarization*, *Phys. Rev. D* **100** (2019) 023509.

[180] M. Millea and U. Seljak, *Marginal unbiased score expansion and application to CMB lensing*, *Phys. Rev. D* **105** (2022) 103531.

[181] L. Legrand and J. Carron, *Lensing power spectrum of the cosmic microwave background with deep polarization experiments*, *Phys. Rev. D* **105** (2022) 123519.

[182] R. Aurlien et al., *Foreground separation and constraints on primordial gravitational waves with the PICO space mission*, *JCAP* **06** (2023) 034 [2211.14342].

[183] L. Legrand and J. Carron, *Robust and efficient CMB lensing power spectrum from polarization surveys*, 4, 2023 [2304.02584].

[184] M. Reinecke, S. Belkner and J. Carron, *Improved CMB (de-)lensing using general spherical harmonic transforms*, 4, 2023 [2304.10431].

[185] CMB-S4 collaboration, *CMB-S4: Iterative internal delensing and r constraints*, 2310.06729.

[186] A.H. Barnett, J. Magland and L. af Klinteberg, *A Parallel Nonuniform Fast Fourier Transform Library Based on an "Exponential of Semicircle" Kernel*, *SIAM Journal on Scientific Computing* **41** (2019) C479 [1808.06736].

[187] A.H. Barnett, *Aliasing error of the* $\exp(\beta\sqrt{1-z^2})$ *kernel in the nonuniform fast Fourier transform*, *arXiv e-prints* (2020) arXiv:2001.09405 [2001.09405].

[188] A.S. Maniyar, Y. Ali-Haïmoud, J. Carron, A. Lewis and M.S. Madhavacheril, *Quadratic estimators for CMB weak lensing*, *Phys. Rev. D* **103** (2021) 083524 [2101.12193].

[189] M.H. Kesden, A. Cooray and M. Kamionkowski, *Lensing reconstruction with CMB temperature and polarization*, *Phys. Rev. D* **67** (2003) 123507 [astro-ph/0302536].

[190] S. Mukherjee, P.K. Aluri, S. Das, S. Shaikh and T. Souradeep, *Direction dependence of cosmological parameters due to cosmic hemispherical asymmetry*, *JCAP* **06** (2016) 042 [1510.00154].

[191] S. Mukherjee and B.D. Wandelt, *Making maps of cosmological parameters*, *JCAP* **01** (2018) 042 [1712.01986].

[192] S.W. Henderson et al., *Advanced ACTPol Cryogenic Detector Arrays and Readout*, *J. Low Temp. Phys.* **184** (2016) 772 [1510.02809].

[193] SPT-3G collaboration, *SPT-3G: A Next-Generation Cosmic Microwave Background Polarization Experiment on the South Pole Telescope*, *Proc. SPIE Int. Soc. Opt. Eng.* **9153** (2014) 91531P [1407.2973].

[194] Simons Observatory collaboration, *The Simons Observatory: Science goals and forecasts*, *JCAP* **02** (2019) 056 [1808.07445].

[195] K. Abazajian et al., *CMB-S4 Science Case, Reference Design, and Project Plan*, 1907.04473.

[196] N. Sehgal et al., *CMB-HD: Astro2020 RFI Response*, 2002.12714.

[197] NASA PICO collaboration, *PICO: Probe of Inflation and Cosmic Origins*, 1902.10541.

[198] S. Mukherjee, *Hemispherical asymmetry from an isotropy violating stochastic gravitational wave background*, *Phys. Rev. D* **91** (2015) 062002 [1412.2491].

[199] S. Mukherjee and T. Souradeep, *Litmus Test for Cosmic Hemispherical Asymmetry in the Cosmic Microwave Background B-mode polarization*, *Phys. Rev. Lett.* **116** (2016) 221301 [1509.06736].

[200] J.I. Cayuso and M.C. Johnson, *Towards testing CMB anomalies using the kinetic and polarized Sunyaev-Zel'dovich effects*, *Phys. Rev. D* **101** (2020) 123508 [1904.10981].

[201] G. Stein, M.A. Alvarez, J.R. Bond, A. van Engelen and N. Battaglia, *The Websky Extragalactic CMB Simulations*, *JCAP* **10** (2020) 012 [2001.08787].

[202] C. Carbone, M. Petkova and K. Dolag, *DEMNUni: ISW, Rees-Sciama, and weak-lensing in the presence of massive neutrinos*, *JCAP* **07** (2016) 034 [1605.02024].

[203] S. Raghunathan, G.P. Holder, J.G. Bartlett, S. Patil, C.L. Reichardt and N. Whitehorn, *An Inpainting Approach to Tackle the Kinematic and Thermal SZ Induced Biases in CMB-Cluster Lensing Estimators*, *JCAP* **11** (2019) 037 [1904.13392].

[204] E.J. Baxter, B.D. Sherwin and S. Raghunathan, *Constraining the Rotational Kinematic Sunyaev-Zel'dovich Effect in Massive Galaxy Clusters*, *JCAP* **06** (2019) 001 [1904.04199].